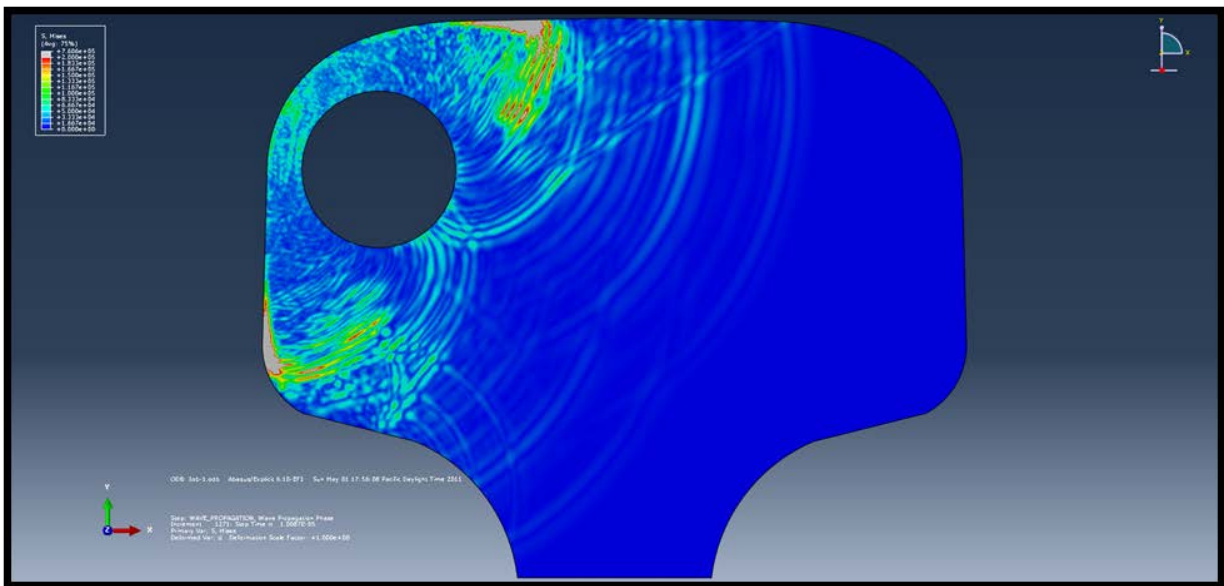U.S. Department of
Transportation

**Federal Railroad
Administration**

Research and Development of Ultrasonic Tomography Technology for Three-Dimensional Imaging of Internal Rail Flaws: Modeling and Simulation

Office of Research
and Development
Washington, DC 20590

REPORT DOCUMENTATION PAGE

1. AGENCY USE ONLY (Leave blank)	2. REPORT DATE April 2013	3. REPORT TYPE AND DATES COVERED Final Report (Performance Period: 04/04/2011–03/31/2012)

4. TITLE AND SUBTITLE Research and Development to Demonstrate Ultrasonic Tomography Technology for Three-Dimensional Imaging of Internal Rail Flaws: Modeling and Simulation	5. FUNDING NUMBERS DTFR53-11-C-00010

6. AUTHOR(S) and FRA COTR

Francesco Lanza di Scalea, Faye M. Reynolds, Piervincenzo Rizzo, Salvatore Salamone, and Ivan Bartoli

FRA COTR: Leith Al-Nazer, FRA Office of Research and Development

7. PERFORMING ORGANIZATION NAME(S) AND ADDRESS(ES) Avanti Tech, LLC 5155 Seachase Street San Diego, CA 92130	8. PERFORMING ORGANIZATION REPORT NUMBER 0009

9. SPONSORING/MONITORING AGENCY NAME(S) AND ADDRESS(ES) U.S. Department of Transportation Federal Railroad Administration Office of Research and Development Washington, DC 20590	10. SPONSORING/MONITORING AGENCY REPORT NUMBER DOT/FRA/ORD-13/20

11. SUPPLEMENTARY NOTES
COTR: Leith Al-Nazer, FRA Office of Research and Development

12a. DISTRIBUTION/AVAILABILITY STATEMENT This document is kept temporarily confidential to the Government.	12b. DISTRIBUTION CODE

13. ABSTRACT (Maximum 200 words)

This report covers the work performed under the FRA High-Speed BAA 2010–2011 program to demonstrate the technology of ultrasonic tomography for 3-D imaging of internal rail flaws. There is a need to develop new technologies that are able to quantify characteristics of the internal rail flaws so as to ensure increased safety of rail transportation and reduced rail maintenance costs. In this work, ultrasonic tomography has been applied to the detection of a 5 percent rail head area (RHA) transverse defect in the railhead. This project has built finite element models of ultrasonic tomographic arrays on a flawed rail and identified an algorithm designed to perform the tomographic imaging of the internal rail flaw in 3-D and automatically. The results show excellent 3-D imaging performance with the proposed approach. The work therefore confirms the potential of the ultrasonic tomography technique for quantitative verification of internal rail flaws.

14. SUBJECT TERMS High-speed rail, rail flaws, tomographic imaging, ultrasonic testing, Finite Element Analysis, digital signal processing	15. NUMBER OF PAGES 120
	16. PRICE CODE

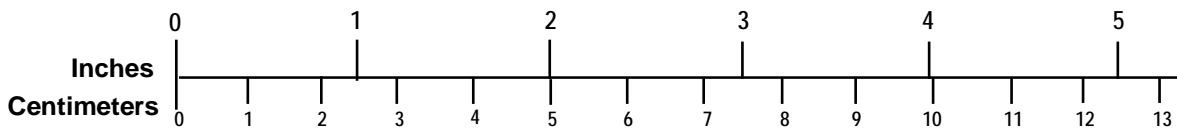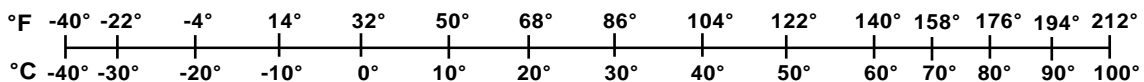| 17. SECURITY CLASSIFICATION OF REPORT Unclassified	18. SECURITY CLASSIFICATION OF THIS PAGE Unclassified	19. SECURITY CLASSIFICATION OF ABSTRACT Unclassified	20. LIMITATION OF ABSTRACT

METRIC/ENGLISH CONVERSION FACTORS

ENGLISH TO METRIC

LENGTH (APPROXIMATE)

1 inch (in)	=	2.5 centimeters (cm)
1 foot (ft)	=	30 centimeters (cm)
1 yard (yd)	=	0.9 meter (m)
1 mile (mi)	=	1.6 kilometers (km)

AREA (APPROXIMATE)

1 square inch (sq in, in^2)	=	6.5 square centimeters (cm^2)
1 square foot (sq ft, ft^2)	=	0.09 square meter (m^2)
1 square yard (sq yd, yd^2)	=	0.8 square meter (m^2)
1 square mile (sq mi, mi^2)	=	2.6 square kilometers (km^2)
1 acre = 0.4 hectare (he)	=	4,000 square meters (m^2)

MASS - WEIGHT (APPROXIMATE)

1 ounce (oz)	=	28 grams (gm)
1 pound (lb)	=	0.45 kilogram (kg)
1 short ton = 2,000 pounds (lb)	=	0.9 tonne (t)

VOLUME (APPROXIMATE)

1 teaspoon (tsp)	=	5 milliliters (ml)
1 tablespoon (tbsp)	=	15 milliliters (ml)
1 fluid ounce (fl oz)	=	30 milliliters (ml)
1 cup (c)	=	0.24 liter (l)
1 pint (pt)	=	0.47 liter (l)
1 quart (qt)	=	0.96 liter (l)
1 gallon (gal)	=	3.8 liters (l)
1 cubic foot (cu ft, ft^3)	=	0.03 cubic meter (m^3)
1 cubic yard (cu yd, yd^3)	=	0.76 cubic meter (m^3)

TEMPERATURE (EXACT)

$[(x-32)(5/9)]$ °F = y °C

METRIC TO ENGLISH

LENGTH (APPROXIMATE)

1 millimeter (mm)	=	0.04 inch (in)
1 centimeter (cm)	=	0.4 inch (in)
1 meter (m)	=	3.3 feet (ft)
1 meter (m)	=	1.1 yards (yd)
1 kilometer (km)	=	0.6 mile (mi)

AREA (APPROXIMATE)

1 square centimeter (cm^2)	=	0.16 square inch (sq in, in^2)
1 square meter (m^2)	=	1.2 square yards (sq yd, yd^2)
1 square kilometer (km^2)	=	0.4 square mile (sq mi, mi^2)
10,000 square meters (m^2)	=	1 hectare (ha) = 2.5 acres

MASS - WEIGHT (APPROXIMATE)

1 gram (gm)	=	0.036 ounce (oz)
1 kilogram (kg)	=	2.2 pounds (lb)
1 tonne (t)	=	1,000 kilograms (kg)
	=	1.1 short tons

VOLUME (APPROXIMATE)

1 milliliter (ml)	=	0.03 fluid ounce (fl oz)
1 liter (l)	=	2.1 pints (pt)
1 liter (l)	=	1.06 quarts (qt)
1 liter (l)	=	0.26 gallon (gal)
1 cubic meter (m^3)	=	36 cubic feet (cu ft, ft^3)
1 cubic meter (m^3)	=	1.3 cubic yards (cu yd, yd^3)

TEMPERATURE (EXACT)

$[(9/5) y + 32]$ °C = x °F

QUICK INCH - CENTIMETER LENGTH CONVERSION

Inches: 0 1 2 3 4 5

Centimeters: 0 1 2 3 4 5 6 7 8 9 10 11 12 13

QUICK FAHRENHEIT - CELSIUS TEMPERATURE CONVERSION

°F	-40°	-22°	-4°	14°	32°	50°	68°	86°	104°	122°	140°	158°	176°	194°	212°
°C	-40°	-30°	-20°	-10°	0°	10°	20°	30°	40°	50°	60°	70°	80°	90°	100°

For more exact and or other conversion factors, see NIST Miscellaneous Publication 286, Units of Weights and Measures. Price $2.50 SD Catalog No. C13 10286

Contents

Illustrations

Tables

Executive Summary

This work was carried out under FRA Broad Agency Announcement (BAA-2010-1) "Research and Demonstration Projects Supporting the Development of High Speed and Intercity Passenger Rail Service." The project has provided proof-of-principle results that show the potential for ultrasonic tomography to offer accurate 3-D imaging of internal rail flaws.

In the past 6 years (2006–2011), according to Federal Railroad Administration (FRA) statistics, rail defects accounted for 1,235 derailments and $321 million in reportable damage costs. The work discussed in this report is motivated by the lack of inspection techniques currently able to provide accurate information about the shape and size of critical internal rail flaws such as transverse defects (TDs) in the railhead. The current rail flaw verification system is a manual process through which rail flaw data is collected and subjectively interpreted by an inspector. This subjectivity can lead to errors in the sizing of defects, and this is a safety concern since an inappropriate remedial action may be taken.

Tomographic techniques are at the forefront of successful imaging systems in the medical field, the sonar and radar fields, and the civil engineering field. The current project has adapted various elements of tomographic imaging from these other fields to develop an ultrasonic tomographic imager specific to internal rail flaws. The numerical results presented herein show great potential for use of the tomographic technique in accurate 3-D rail flaw imaging. The advantages of this approach include the following: (1) no manual scanning of the transducers is required, and (2) the imaging results are provided automatically with minimal operator interpretation, which eliminates the potential subjectivity inherent in the manual process.

1. Introduction

Internal rail flaws are a cause of major concern for rail transportation safety. If left undetected, flaws can grow and lead to rail failure and catastrophic derailments. With the advent of high-speed rail, and the increased tonnage and frequency of freight trains, the importance of detecting internal rail defects before they result in a complete rail break is magnified. Because high-speed operations necessitate shorter rail maintenance windows, there is greater need to detect the flaws early and accurately.

FRA safety statistics for the past 6 years (2006–2011) indicate that defects at rail, joint bars, and rail anchoring were responsible for 1,235 derailments and \$321 million in reportable damage costs in the United States. Among the rail defects, TDs in the railhead, i.e., flaws that are oriented perpendicularly to the rail running direction, are consistently the most critical, causing the highest percentage of derailments and damage cost.

Currently, rail flaw inspection in the United States is performed from a dedicated, in-motion hi-rail vehicle that is outfitted with ultrasonic transducers, and a detected flaw must then be manually verified ("stop and confirm" mode). The hand verification is typically done using ultrasonic transducers operated in a pulse-echo mode. At present, the manual verification does not allow for precise quantification of the defect size and shape. Rather, defect sizing is somewhat subjective since it depends on the inspector's judgment and level of experience. What is needed is a new inspection system for rails that is able to provide accurate and repeatable quantitative information on the shape and, more importantly, the size of an internal flaw. Hence, the need for 3-D rail flaw imaging, which the FRA BAA-2010-1 explicitly identifies as a critical research need.

1.1 Objectives

The objective of this project is to demonstrate the technique of ultrasonic tomography for 3-D imaging of internal rail flaws. The scope of the project was limited to carrying out numerical analysis and simulations of the tomographic rail imaging technique. It is expected that the successful completion of this modeling phase will lay the foundation for the subsequent development of a tomographic rail imaging system for use in verification of rail flaws. The

numerical work was carried out with the following requirements in mind for a possible future field-deployable system: (1) ability to size the flaw automatically without manual scanning of the ultrasonic transducers, (2) ability to resolve TDs as small as 5 percent railhead area (RHA), and (3) ability to generate a 3-D image of a defect in a reasonable timeframe, preferably less than 10 minutes.

1.2 Overall Approach

In the first part of the project, Finite Element Analysis (FEA) models of a 136-pound RE rail were constructed in 2-D and, subsequently, in 3-D. Through appropriate discretization of the space domain (mesh refinement to represent small wavelengths) and of the time domain (integration time refinement to represent high wave frequencies), the models were able to represent ultrasonic waves (up to 2.25 MHz) propagating in the rail and interacting with internal rail flaws. The 3-D model also featured advanced nonreflecting boundary FEA elements (to eliminate artificial wave reflections at the FEA model boundaries that would not be present in an actual rail), as well as absorbing FEA elements to simulate wave damping.

The FEA allowed for simulation of an array of ultrasonic transducers operated in a tomographic scheme. The tomographic algorithm was developed in a Matlab environment to provide 2-D and 3-D images of an internal 5-percent RHA TD flaw simulated in the railhead. The tomographic algorithm used the following four key steps to generate the images: (1) Synthetic Aperture Focus (borrowed from ultrasonic, medical and radar imaging), (2) Matched Filtering (borrowed from radar imaging), (3) Baseline Subtraction (borrowed from ultrasonic testing), and (4) Multimode Detection (borrowed from ultrasonic testing).

The ultrasonic tomographic array for the 3-D imaging consisted of up to 252 transducers arranged in a planar fashion to generate 3-D images without requiring mechanical repositioning of the transducers during the imaging process. Two configurations for the array were examined: a sparse transmitter configuration (5 transmitters) with a full receiver configuration (525 receivers), and a sparse transmitter configuration (5 transmitters) with a reduced receiver configuration (140 receivers). In addition, different wave mode combinations were examined. It was found that reducing the receiver array did not have a substantial impact on the performance

of the 3-D imaging in a new rail profile. The tomographic algorithm produced good results; the estimated size of the imaged flaw was close to the 5 percent RHA actual size.

A worn rail, modeled after a tangent track profile received from Burlington Northern Santa Fe (BNSF) Railroad, was also examined in the final phase. It was concluded that profile wear does not have any effect on tomographic imaging performance when the full receiver array is used. For the reduced receiver array, by contrast, some degradation was seen in the worn rail case.

1.3 Organization of the Report

Section 1 of this report introduces the project and describes the overall technical approach. Section 2 reviews the current practice of ultrasonic testing in the railroad industry. Sections 3 and 4 review various applications of ultrasonic tomography imaging in the civil engineering and medical field. Section 5 presents the 2-D FEA of ultrasonic waves propagating in the 136-pound RE rail. Section 6 extends the previous analysis to the 3-D case. Section 7 summarizes the steps of the tomographic imaging algorithm developed for 2-D and 3-D imaging of the rail flaws. Section 8 presents the results of 2-D tomographic imaging of a 5-percent RHA TD in the 136-pound RE rail, along with a noise sensitivity analysis. Section 9 presents the results of 3-D tomographic imaging of the 5-percent RHA TD in the 136-pound RE rail. Section 10 extends the 3-D imaging results to the case of a worn rail. Section 11 summarizes the conclusions of this work.

2. Current Practice of Ultrasonic Testing of Rails

This chapter reviews the current practice of ultrasonic testing in the railroad industry.

2.1   Bulk Wave Testing

Ultrasonic Testing (UT) has been widely used by the railroad industry for rail internal defect detection since the 1960s. Normally, the UT inspection is targeted at detecting defects in the center of the rail head and web, with only limited coverage of the rail base and rail head corners. The frequency of rail track inspection varies from country to country. In the United States, FRA mandates that inspections for track defects be made at least once every 40 million gross tons (mgt) or once a year—whichever interval is shorter—for tracks over which passenger trains operate. For tracks over which passenger trains do not operate, the inspection must be carried out every 30 mgt or once a year, whichever interval is longer.

UT of rail tracks is performed with longitudinal or transverse transducers operated in a pulse-echo mode or in a pitch-catch mode (Figure 2.1). The transducers are located in wheels which roll over the surface of the of the rail head. The wheels are typically filled with water or a water-based solution. Sleds, rather than wheels, can also be used to host several transducers in a smaller area. Specialized test cars typically perform the inspection. Details on common transducer configurations can be found in various references (Bray 1991, Anon 1990, Grewal 1996, Lanza di Scalea 2007). The most common configuration (Figure 2.1 uses transducer orientations that are able to generate ultrasonic beams propagating at 0 degrees (normal incidence) and at 70 degrees from the normal to the rail surface. The 0-degree probe targets horizontal cracks while the 70-degree probe targets the transverse cracks that tend to grow in a 20-degree direction from the transverse plane.

A 37- or 45-degree probe is also often used in addition to the previous two orientations to target other defects such as bolt-hole cracks and weld defects (Figure 2.1-left). To target vertical defects, complete search units also host "side looking" transducers generating beams in the transverse plane, typically at 45-degree orientations, rather than in the vertical plane of the track (Figure 2.1-right).

Wheels or sleds are often used in tandem to provide complete coverage. Using tandem configurations adds pitch-catch testing capability to the pulse-echo capability of a single wheel.

The standard transducer of a rail track UT unit operates at 2.25 MHz; 3 MHz transducers can also be used.
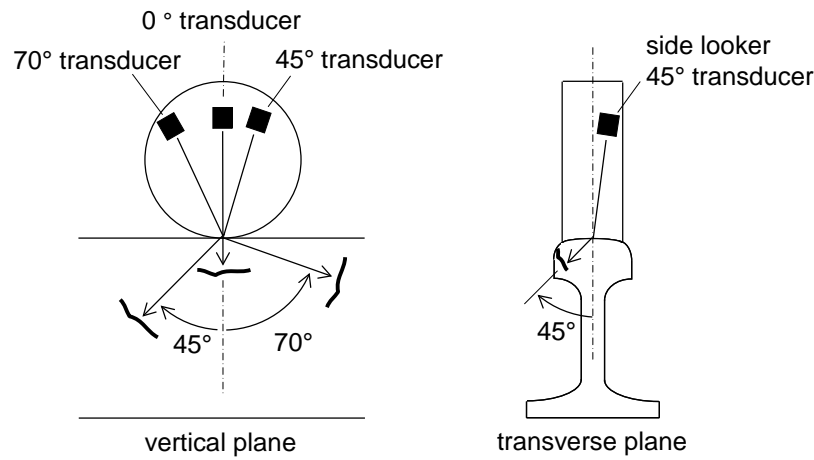
Figure 2.1. Common transducer arrangements for rail track inspections in the vertical plane (left) and in the transverse plane (right). (Lanza di Scalea 2007)

The test car inspections of rail tracks are followed by manual scanning to confirm the presence of a defect and to size it. Generally, both normal-beam transducers and angle-beam transducers (with conventional acrylic wedges) can be used in manual scanning. As mentioned above, normal-beam transducers target horizontal-type defects while angle-beam transducers target transverse-type defects. Defect sizing is done by simply scanning the normal-beam transducer for horizontal defects and using the conventional 6 decibel (dB) down technique while scanning the angle-beam transducers.   In addition to conventional normal-beam or angle-beam configurations, more complex transducer arrangements can be implemented during manual scanning. Skewed transducer orientations, for example, can be used to detect detail fractures. In skewed arrangements, the ultrasonic wave propagates along planes that are inclined with respect to both the vertical and the transverse plane so as to enhance the interaction with certain types of defects.

In the United States, manual UT is required to verify any defect indication from the test car search units ("stop and confirm" testing mode). Europe, on the other hand, operates in a nonstop testing mode, whereby defect indications are verified by manual UT only days or weeks after the test car has passed. Modern test cars can operate, theoretically, at reasonably high testing

speeds—up to at least 30 mph (45 km/h)—although much testing is conducted at speeds as low as 10 mph (15 km/h).

One serious disadvantage to current wheel or sled transducer arrangements is that in the presence of shallow horizontal cracks such as head checks and shelling, internal TDs in the rail may be missed by inspection (Figure 2.2). Another drawback is that the high probing frequency used by the transducers (2.25–3 MHz) is sometimes not effective in penetrating alumino-thermic welds, which have a coarser grain structure compared with the surrounding steel (Clark and Singh 2003, Wilcox et al. 2003). Additional challenges with conventional ultrasonic inspections of rails have to do with detecting vertical split head defects and small TDs in the gage corner of the rail head. The presence of leaves, dirt, ice, and other foreign objects can affect the ultrasonic transmission and reception through the wheel or sled.

70-deg ultrasonic transducer

rail

Horizontal shelling
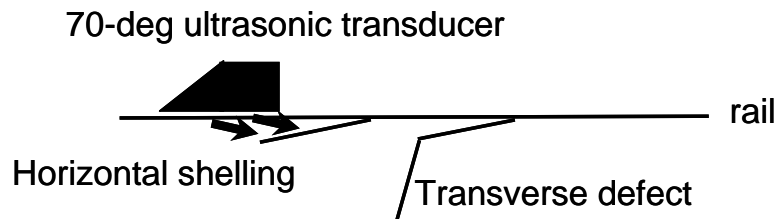
Transverse defect

Figure 2.2. Masking of internal transverse defects under shelling in conventional ultrasonic testing of rails.

2.2   Ultrasonic Phased-Arrays – Basic Principles

Ultrasonic phased arrays offer more flexibility than single-element ultrasonic transducers because they can achieve beam steering and beam focusing without physically moving the transducers.

Traditional single-element ultrasonic transducers excite a beam propagating along a fixed direction and, if necessary, focus the beam to a fixed point via acoustic lenses. However, neither beam direction nor focal point can be changed in a single transducer without moving the transducer or replacing the acoustic lens. Phased arrays are comprised of multiple transducers that are electronically delayed to build a constructive interference wavefront (Figure 2.3). By changing the time delays between the elements of the array, the resulting wavefront can be

pointed to different directions (beam steering) and also focused at different depths (dynamic focusing) without mechanical motion.
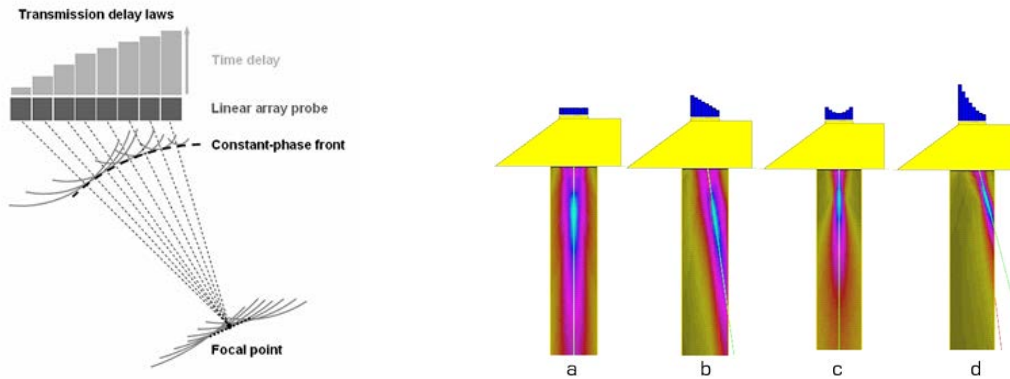
Figure 2.3. Principle of multiple transducers firing at imposed delays in phased-array ultrasonic probes (dynamic steering and dynamic focusing).

A minimum of three elements is required for steering and focusing capabilities. Increasing the number of elements increases the resolution of the beam steering and focusing. Phased arrays exist in different forms, including linear arrays, 2-D arrays, and circular arrays (Figure 2.4). Linear arrays allow steering and focusing across a plane. 2-D arrays allow complete 3-D steering and focusing.
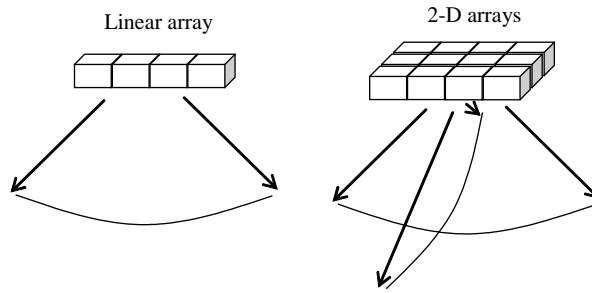
Figure 2.4. Different configurations of phased-array ultrasonic probes: linear arrays and 2-D arrays.

2.3   Applications of Ultrasonic Phased-Arrays in the Rail Industry

Phased arrays in the railroad industry have been applied primarily to the inspection of axles (Hansen and Hintze 2002). They were used in this research effort to detect the radial cracks in the press fitted areas of the axle, including wheel seats, brake disk seats (for trailing axles), and gear seats (for driving axles). Other targets were cracks in the transition regions between two diameters.

Traditional inspection systems for axles rely on either single transducers operating from the free end of the axle (Figure 2.5a), or angle-beam transducers requiring manual scanning (Figure 2.5b). Ultrasonic phased arrays eliminate the manual scanning of the angle-beam transducers (Figure 2.5c).
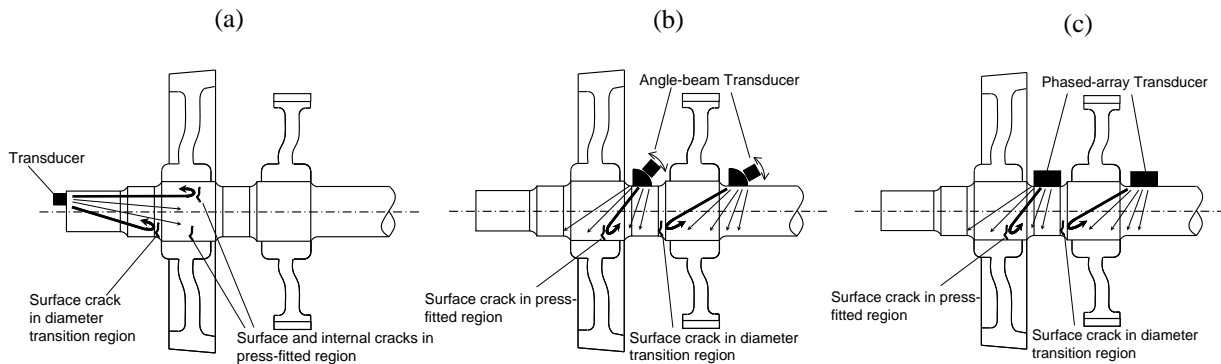
Figure 2.5. Transducer arrangements for axle inspections: (a) longitudinal transducer at axle free end; (b) angle-beam transducers; (c) phased-array transducers. (Lanza di Scalea 2007).

For rail inspections, phased-arrays are not common practice, although published research has been performed by the authors cited herein.

Utrata (2002) used a 16-element, linear phased array under dry contact to enhance the detectability of transverse head cracks and this was compared with the results of single-element inspections. Starting with the typical 70-degree angle, this phased array was used to steer the beam across the rail section ("lateral steering") for a +/-20-degree angle relative to the centerline of the head. The lateral steering demonstrated that most transverse cracks are best detected off angle, specifically at a 10-degree angle from the centerline of the rail.

Wooh and Wang (2002) proposed the use of a "hybrid array sensor" for rails consisting of a traditional phased array for electronic generation of beam steering and a static array for beam detection. Crack detection was done by elaborating the "ultrasonic shadows" detected by the static array. It was suggested that this concept would be capable of determining the location, size, and orientation of a planar transverse head defect. Although results were not shown on actual rails, the theory worked out in the model seems applicable to the rail case. However, the proposed approach assumes flat planar cracks, and therefore cannot capture the full shape of a curved defect. Moreover, the method uses generation and detection of ultrasound from the same side of the rail. This may not be the best approach, as waves must bounce from the back wall of the rail to be detected. A straight-path beam in a through-transmission configuration is probably more appropriate for capturing ultrasonic shadows.

Tscharntke et al. (2003) developed directivity patterns for dry-coupled phased array probes. Their studies were mainly theoretical and showed limited laboratory results involving actual railroad specimens.

More recently, the Transportation Technology Center, Inc. (TTCI) investigated ultrasonic phased arrays for rail web, base, and head inspection focusing on the defect sizing and characterization (Garcia and Zhang 2006). The authors used pulse-echo phased-array probes on 33.7-degree wedges at 5 MHz positioned on the sides of the rail head (Figure 2.6). They concluded that phased arrays can (a) detect TDs and discriminate them from a shell, (b) determine the location of the TD in the rail, and (c) estimate the size of the TD in the rail. In essence, TTCI researchers confirmed the ability of phased-arrays to dynamically steer the ultrasonic beam.
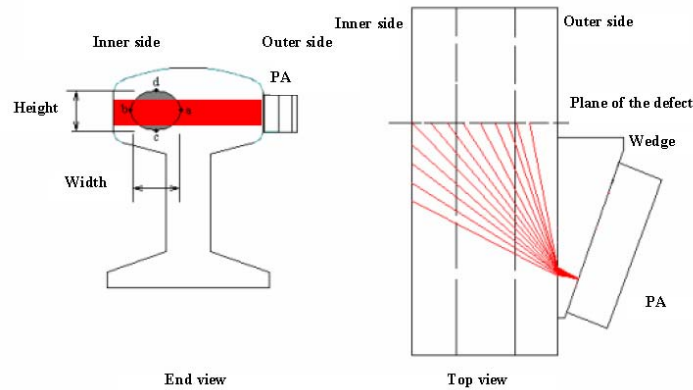
Figure 2.6. TTCI approach of ultrasonic phased arrays for rails. (Garcia and Zhang 2006).

2.4   Ultrasonic Tomography- Basic Concepts

Ultrasonic tomography is a noninvasive and safe technique for the cross-sectional imaging of an object through transmission or reflection data collected by illuminating the sample from different directions. CT scans (Computerized Tomography) are routinely performed in the medical field to image tumors, organs, and other parts of the human body. Medical CT scans primarily use X-rays or Magnetic Resonance Imaging (MRI). With solids, such as rail steel, however, ultrasonic scans are more practical, and the corresponding technique is called ultrasonic tomography. Ultrasonic tomography is being applied successfully to various civil engineering fields (as the next chapter will discuss).

Similarly to phased arrays, an ultrasonic tomography setup uses a series of transducers to excite and receive ultrasonic waves. Multiple wave paths are then recorded to cover every direction of the test volume (Figure 2.7). Algorithms based on wave propagation theory are then used to reconstruct the exact shape, position, and size of a defect from the multiple propagation paths.

Various applications of ultrasonic tomography for imaging will be discussed in this report.
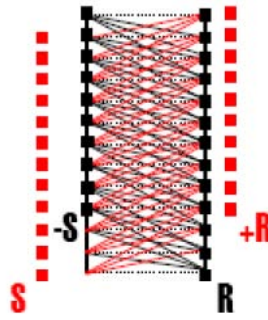
Figure 2.7. Basic concept of ultrasonic tomography for imaging defects in solids (S = ultrasonic sources, R = ultrasonic receivers). (Mekic-Stall and Grimm 2002)

2.5 Ultrasonic Tomography with Synthetic Aperture Focusing – Basic Concepts

A successful method borrowed from radar technology that also uses transducer arrays for ultrasonic tomographic imaging of structural defects is the Synthetic Aperture Focusing Technique (SAFT). It is a computer enhanced imaging technique for the detection and the characterization of discontinuities (ASNT 2007). The technique numerically superimposes multiple ultrasonic pulse-echo time signals, measured at several positions, to create a high resolution image. The signals are assembled and integrated, or focused, with respect to the time-of-flight surface in volume and time space for each voxel (volumetric picture element) of material (ASNT 2007).

SAFT locates the position of the ultrasonic reflector (flaw) based on the arrival time of pitch-catch ultrasonic signals (Figure 2.8-left). In the simplest implementation, the defect position from a transmitter-receiver pair can be calculated using the Pythagorean Theorem for known transducer positions. Referring to Figure 2.8-right, this formula is:

$$d = \sqrt{\left(v\,\Delta t / 2\right)^2 - X^2}$$

where v is the wave speed in the test object and Δt the travel time of the wave between the transmitter and the receiver.
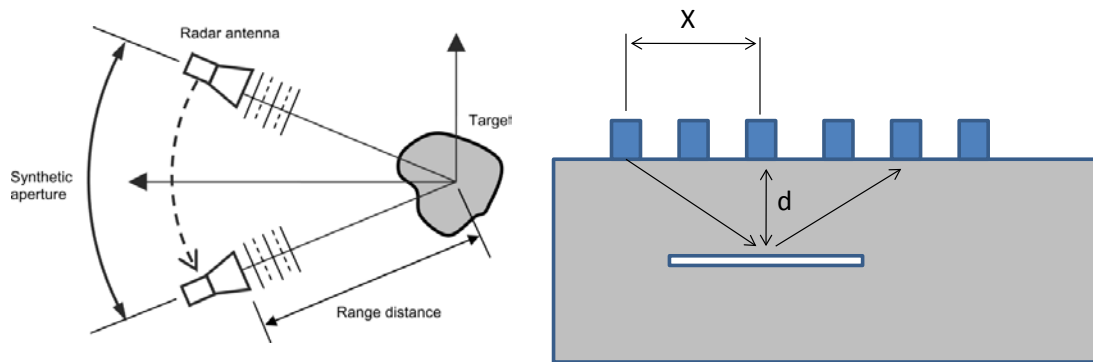
Figure 2.8. Principle of Synthetic Aperture Focusing. Left: radar. Right: ultrasonic testing.

Conventional SAFT operates sequentially in two stages. First, each transducer element emits and receives an ultrasonic signal which is digitized and stored. Then, digital signal processing is applied to generate the scanning lines, which form the UT image (Martinez et al. 1999). By using arrays of ultrasonic transmitters and receivers in conjunction with SAFT, detailed 3-D imaging of internal flaws is possible.

Since SAFT is based on the processing of stored data, multiple algorithms can be applied and new algorithms are being continually developed. The raw data are usually A-scans stored as the broadband transducer is scanned over the surface of the test object. In one implementation (ASNT 2007), a curve is made of the peak amplitudes caused by the reflection from the discontinuity for each aperture element. The size of this curve's path is determined by the width of the ultrasonic beam. The curvature and apex of the curve depend on the depth of the discontinuity, the ultrasonic velocity in the test material, and the coupling medium.

One of the most successful applications of SAFT for imaging internal defects is in the inspection of concrete slabs for civil engineering. The "MIRA Tomographer," used by various companies, including the CTL Group of Skokie, IL (CTL Group 2011) (Figure 2.9), uses pitch-catch ultrasonic tomography and SAFT to reconstruct 3-D representations of internal defects that may be present in concrete elements such as prestressed concrete slabs. The system uses low frequencies, typically 50 kHz, to penetrate the coarse concrete microstructure. A dry-coupled array of 4×10 transducers provides a total of 180 transit time measurements during each test.

13

The recordings are done sequentially, with each row of transducers acting as the transmitter and all other rows acting as receivers. The entire scan takes approximately 3 seconds for complete data acquisition. SAFT is then used to reconstruct the 3-D image of the internal flaws from the transit times of the multiple wave paths.
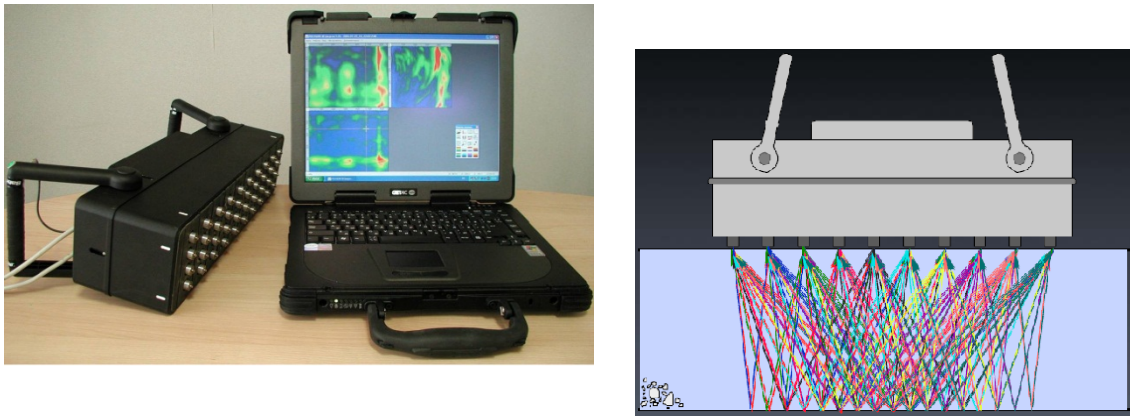
Figure 2.9. The MIRA Tomographer that uses a 4×10 transducer array in dry-coupling for concrete inspection. (Bishko et al. 2008 and CTL Group 2011)

3. Bidimensional Finite Element Analysis

This chapter discusses the 2-D FEA performed to model ultrasonic waves propagating in a flawed rail.

3.1 2-D Finite Element Model of Flawed Rail

The specific case that was modeled by these initial FEA was a 2.25 MHz ultrasonic wave propagating in a 136-pound RE rail with a TD in the gage corner extending for 5 percent of the rail RHA. The TD is one of the most common flaws found in rails.

The choice of the 2.25 MHz value reflects the most common frequency used in ultrasonic rail inspections (both with in-motion wheel transducers and hand-held transducers for verifications). Figure 3.1 shows the picture of an actual TD at the railhead gage corner taken at the Herzog, Inc. rail defect farm.

Figure 3.1. A picture of a Transverse Defect at the gage corner of the railhead.

The corresponding geometrical model for the 2-D FEA is shown in Figure 3.2. The geometrical dimensions of the model were as follows:

Entire rail section:

Area = 0.0084 m^2

Perimeter = 0.7087 m

Railhead alone:

Area = 0.0034 m^2

Perimeter = 0.2252 m

The TD was modeled as a 5 percent RHA planar flaw.
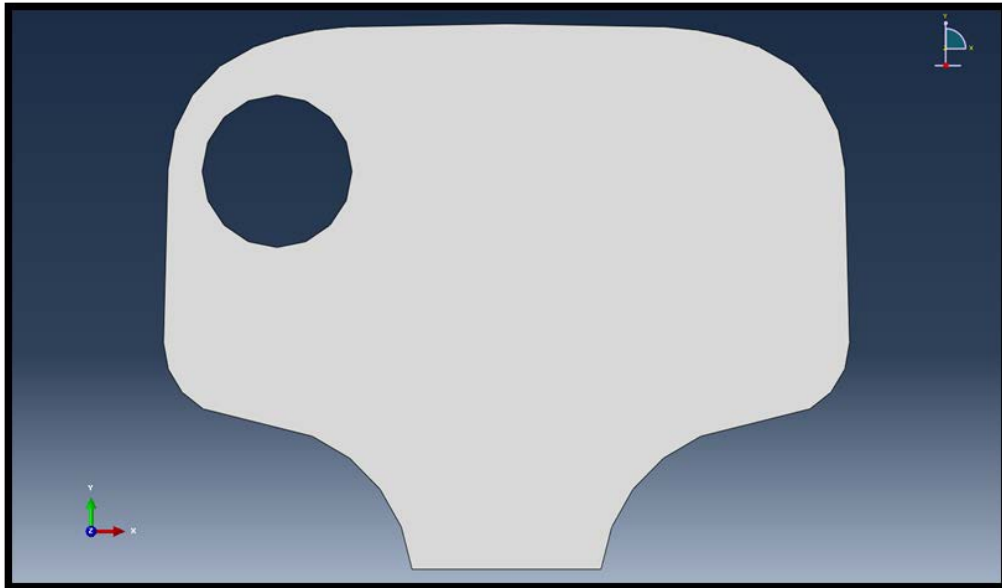
Figure 3.2. The geometrical model of the rail for the 2-D FEA with the 5% RHA Transverse Defect in the gage corner.

The material properties of the model were steel, with the following elastic constants:

Young's modulus E = 209 GPa

Poisson's ratio ν = 0.28

Mass density ρ = 7800 kg/m^3.

Assuming a maximum wave frequency f_{max} = 2.25 MHz and hence a minimum wavelength λ_{min} = c_S / f_{max} = 1.33 mm (with c_S the shear wave velocity in steel), the maximum dimensions of the finite elements were chosen as:

$d_{max} = \lambda_{min} / 10 = 0.133$ mm

This level of mesh refinement ensured proper representation of the minimum ultrasonic wavelength (or maximum frequency). To reduce the computational burden, it was decided to model only the railhead—the only portion of the rail relevant for the defect considered. The resulting finite element mesh is shown in Figure 3.3. A close-up view of the mesh in the area surrounding the defect is shown in Figure 3.4.
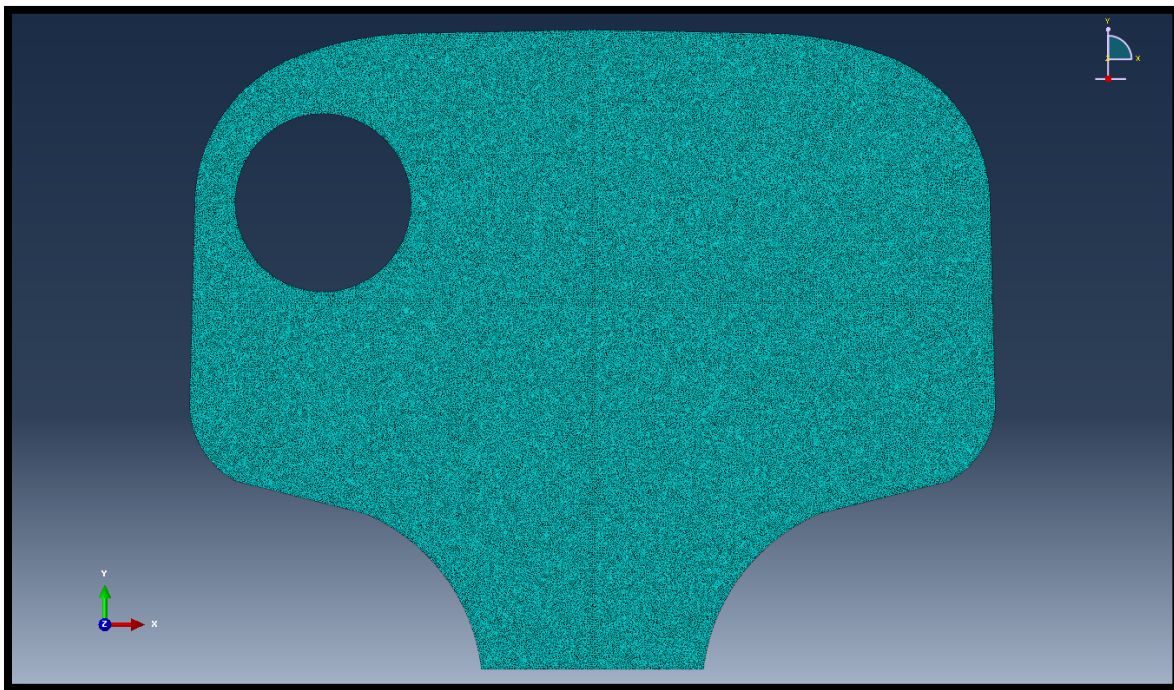
Figure 3.3. The total mesh for the 2-D FEA.
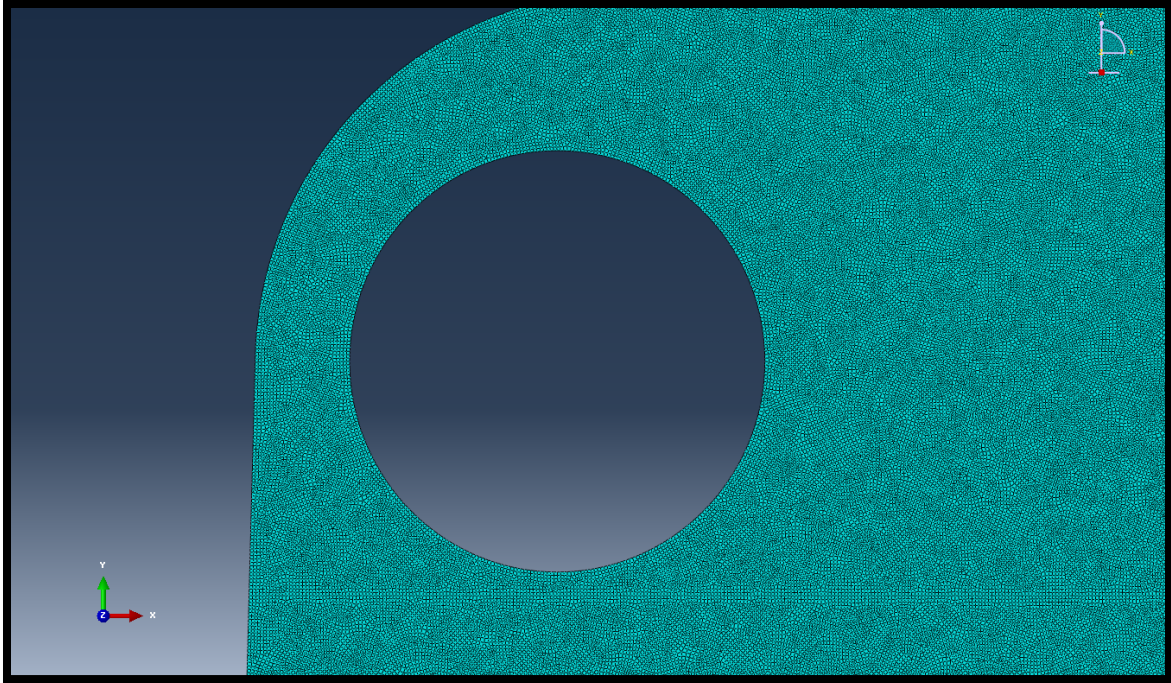
Figure 3.4. A zoom of the mesh around the defect for the 2-D FEA.

The final parameters of the mesh utilized were as follows:

```
              P R O B L E M    S I Z E


NUMBER OF ELEMENTS IS                              235682
NUMBER OF NODES IS                                 236746
NUMBER OF NODES DEFINED BY THE USER                236746
TOTAL NUMBER OF VARIABLES IN THE MODEL             473492
```

The total duration of the analysis, sufficient to capture the relevant wave diffractions from the defect, was 30 μsec. The maximum time increment was chosen according to the customary criterion of:

$\Delta t_{max} = 1 / (20{*}f_{max}) = 0.0222$ μsec

This time increment limit ensured proper representation of the highest frequency components of the waves.

In this analysis, the forcing function (simulating the ultrasonic generation) was applied to the gage corner of the railhead as one sinusoidal cycle at 2.25 MHz with a duration of 0.4 μsec and a nominal unity amplitude (Figure 3.5). The specific amplitude value of this excitation was

18

irrelevant to the analysis, as the purpose was to capture reflections and refractions of the wave from the defect.
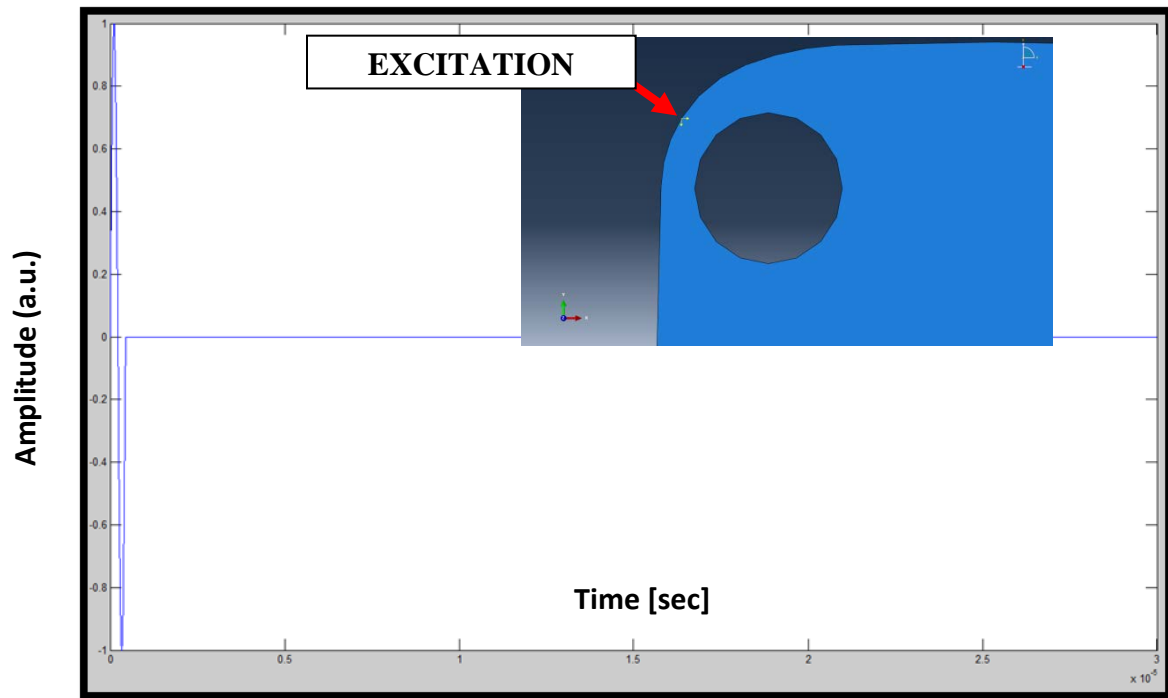
Figure 3.5. Shape and location of the excitation force for the 2-D FEA simulating 2.25 MHz ultrasonic excitation at the rail gage corner.

Five detection points were considered on the field side of the railhead, as shown in Figure 3.6 below. These points represent possible locations of the ultrasonic receivers.
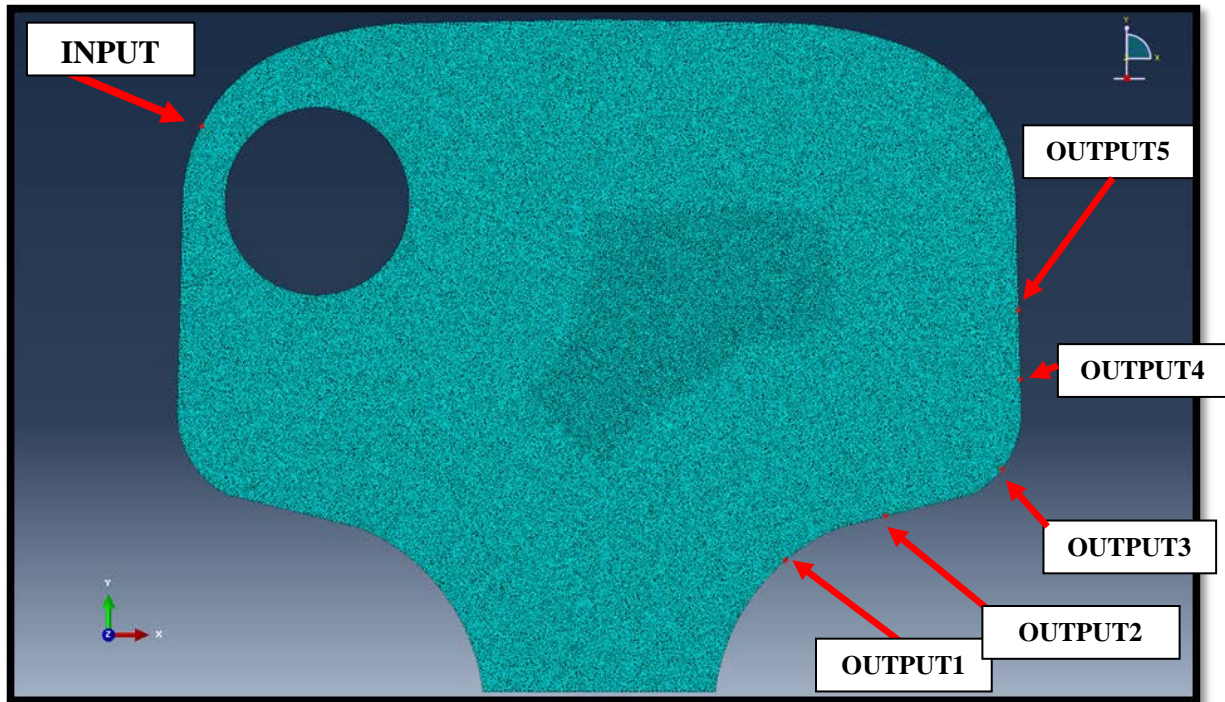
Figure 3.6. Location of the excitation point and of five detection points used to sample the ultrasonic waves interacting with the flaw in the 2-D FEA.

3.2 Results of 2-D Finite Element Model

Contour plots of the Von Mises Equivalent stress are shown in the following figures (Figures 3.7 through 3.12) at six different times during the ultrasonic wave propagation. Interesting or unusual behaviors are captured by these plots; for example, the strong surface (Rayleigh) wave travelling along the railhead top surface.

In the region internal to the railhead, the plots also show the refraction of the wave caused by the 5-percent RHA TD. Another interesting behavior is the smaller surface (Rayleigh) wave developing along the defect surface and following the defect perimeter. Strong bulk waves are also generated past the defect as the diffracting wavefronts interfere constructively past the defect. This phenomenon is analogous to the "anomalous" strong ocean waves generated at the downwind side of an island. As a result, a variety of wavefronts are received at the opposite side of the defect. These multiple wavefronts were eventually used to develop the ultrasonic tomographic system for defect imaging.
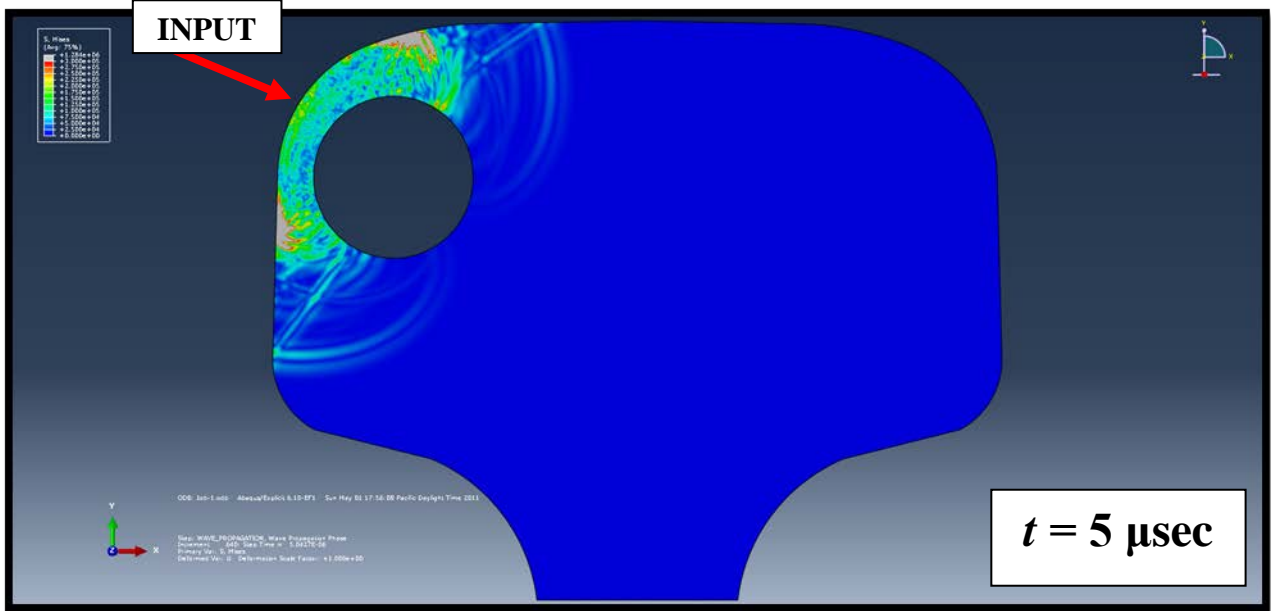
Figure 3.7. Contour plots of Von Mises Equivalent Stress at *t* = 5 μsec after excitation from the 2-D FEA.
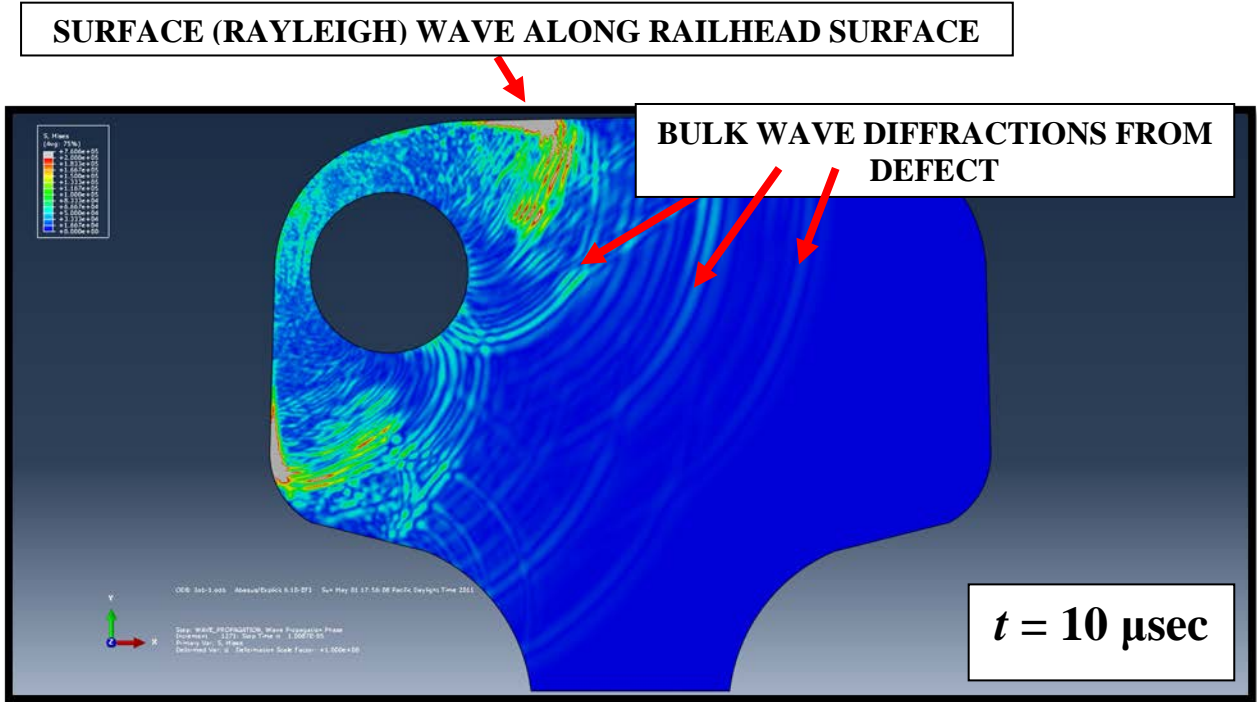
Figure 3.8. Contour plots of Von Mises Equivalent Stress at *t* = 10 μsec after excitation from the 2-D FEA.

SURFACE (RAYLEIGH) WAVE ALONG DEFECT SURFACE
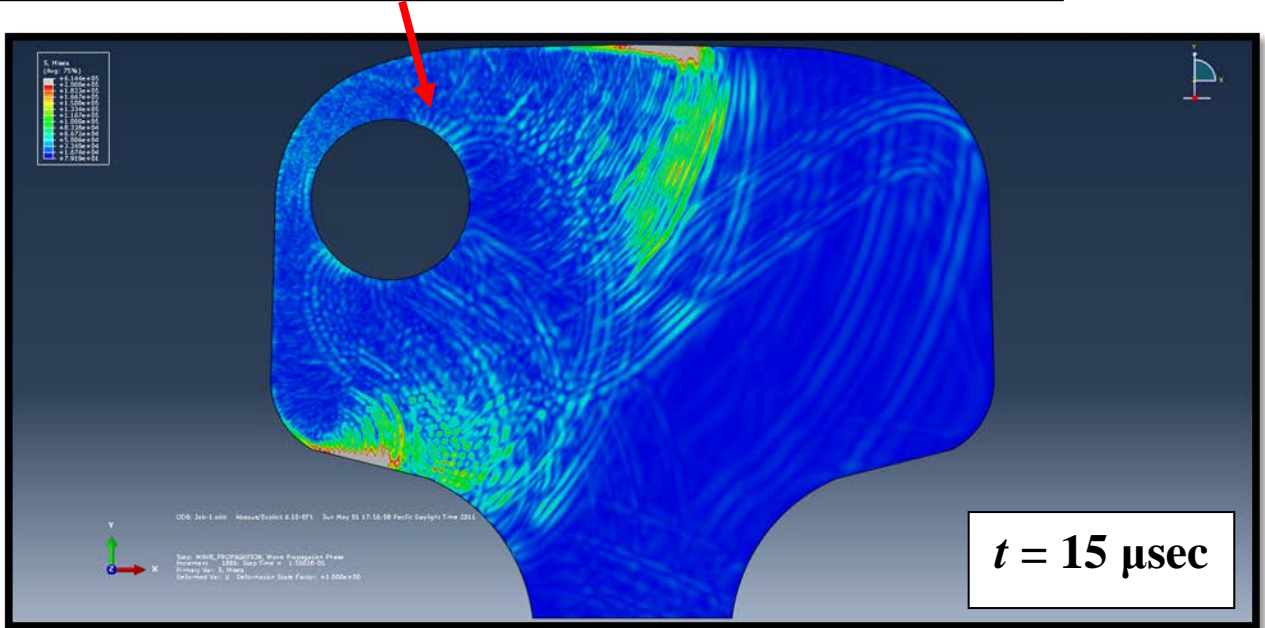
Figure 3.9. Contour plots of Von Mises Equivalent Stress at t = 15 μsec after excitation from the 2-D FEA.
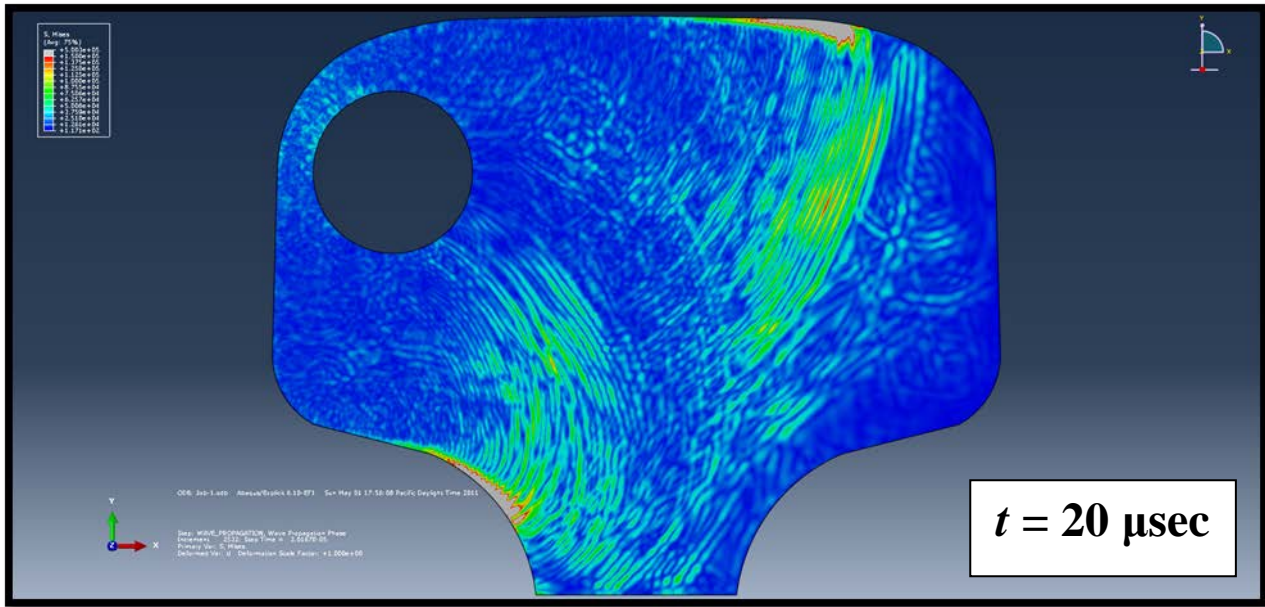
Figure 3.10. Contour plots of Von Mises Equivalent Stress at t = 20 μsec after excitation from the 2-D FEA.
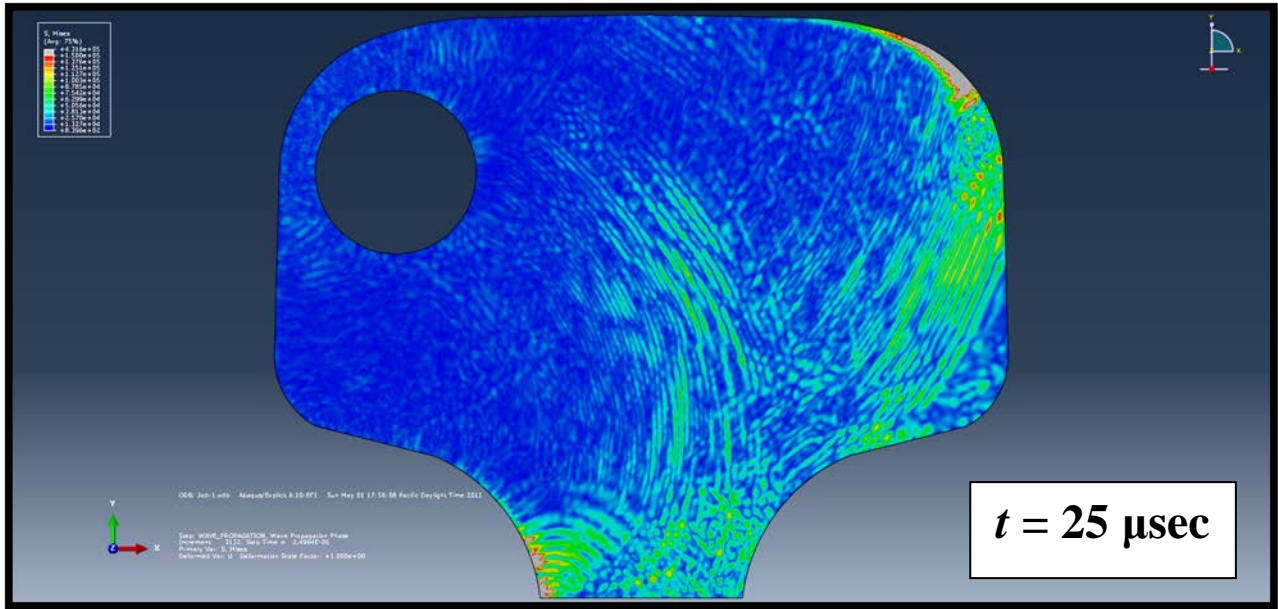
Figure 3.11. Contour plots of Von Mises Equivalent Stress at t = 25 µsec after excitation from the 2-D FEA.
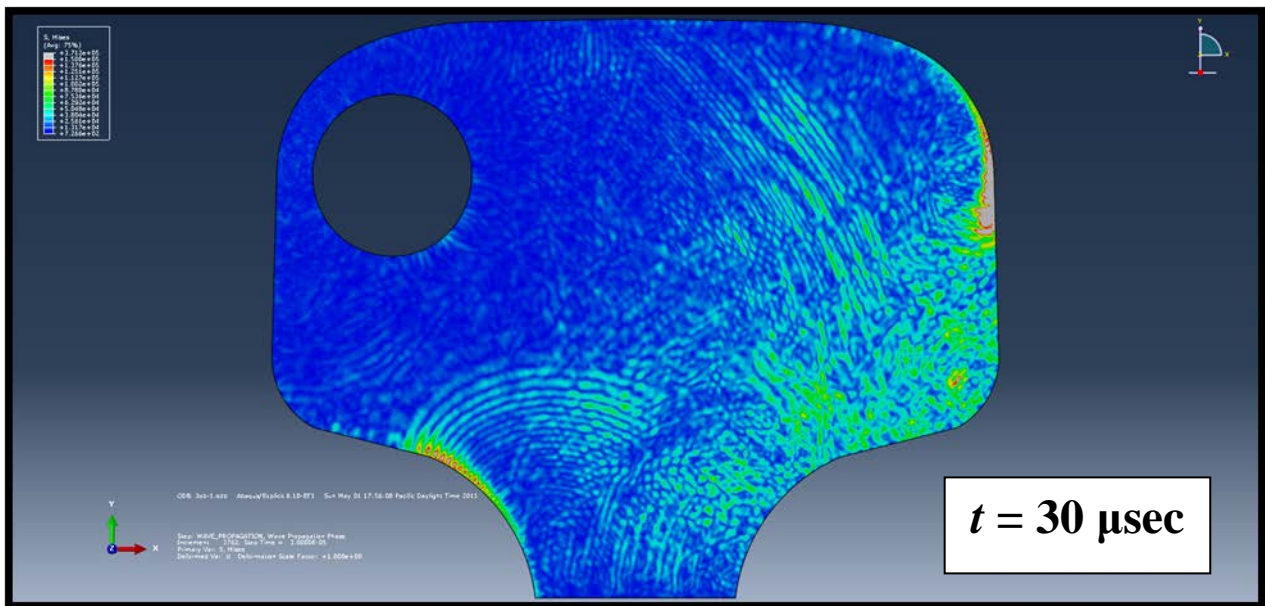
Figure 3.12. Contour plots of Von Mises Equivalent Stress at t = 30 µsec after excitation from the 2-D FEA.

Figure 3.13 shows the plots of the time histories of the transverse displacement (u_x) recorded at the five detection nodes considered. The multitude of the wave modes detected is also apparent in these time histories, with the bulk waves diffracted from the flaw arriving early and the strong Rayleigh wave running along the railhead arriving later. For the internal defect imaging, the initial portion of the time histories will be of interest, as it is the section that contains information about the wave that has interacted with the flaw.
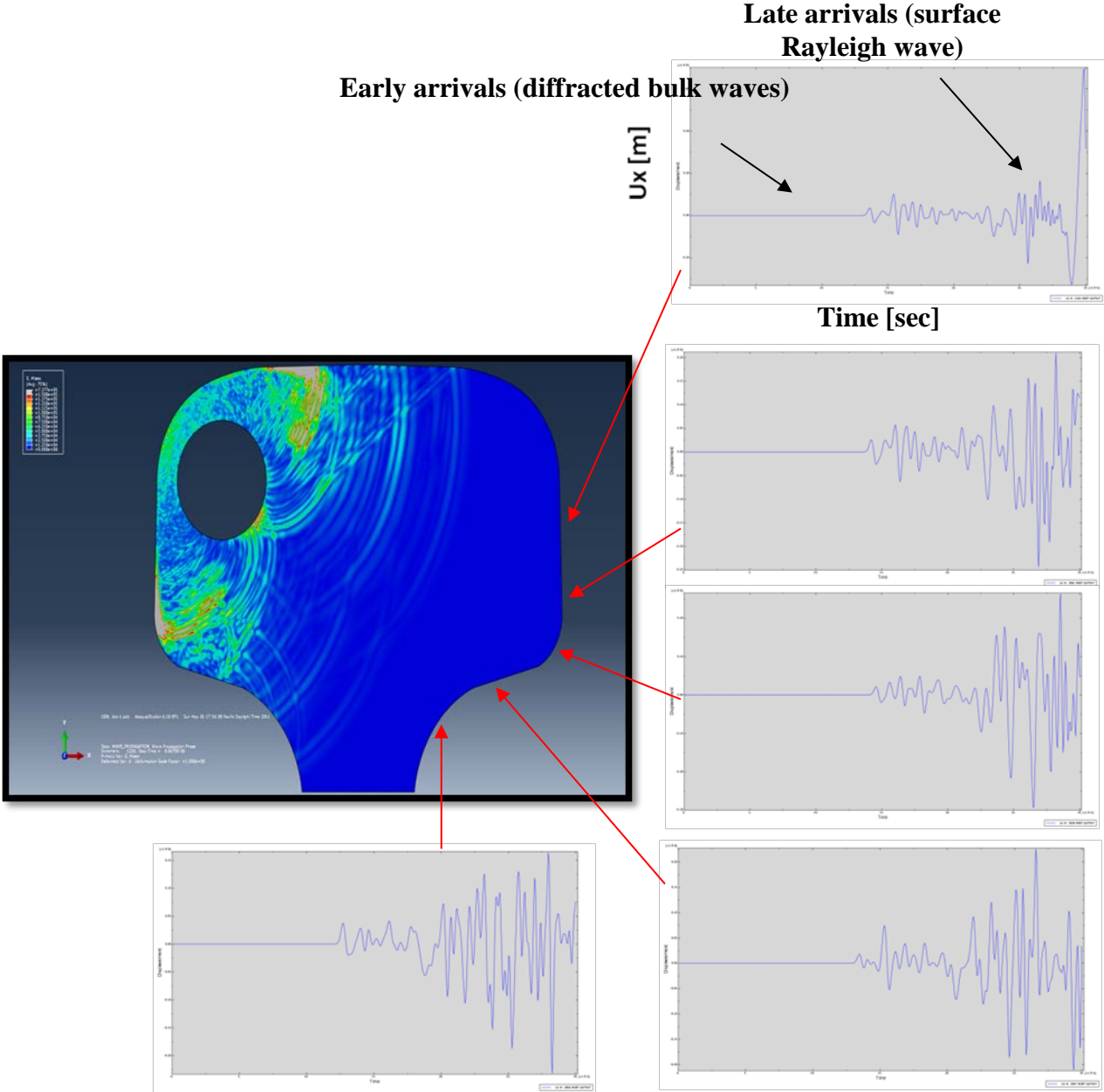
Figure 3.13. Time histories of transverse displacement u_x recorded at the five detection nodes by the 2-D FEA.

4. Three-Dimensional Finite Element Analysis

This chapter discusses the 3-D FEA performed to model ultrasonic waves propagating in a flawed rail.

4.1 3-D Finite Element Model of Flawed Rail

In order to create a more realistic model, the bidimensional analysis presented in the previous section was extended to the three-dimensional case. The 3-D case is more representative of an actual ultrasonic tomographic system as the ultrasonic transmitters and receivers will likely be positioned on different planes.

A length of 10 cm for the rail was considered for the 3-D analysis. This length was adequate to capture the wave interaction with the defect. The geometric case considered was analogous to the 2-D analysis (i.e., 136-pound rail with a 5-percent RHA TD at the gage corner).

To satisfy the mesh refinement requirements for modeling the high-frequency waves, a careful sectioning of the meshed region was applied. Three mesh zones were created. In Zone 1 (Figure 4.1), the mesh was left coarser, with a maximum element size $d = 3$ mm. The corresponding mesh of this zone is shown in Figure 4.2. In Zone 2, called "transition zone," an intermediate element size of $d = 1.5$ mm was created (Figures 4.3 and 4.4). This zone provided a smooth change from the coarser mesh, away from the flaw, to the highly refined mesh around the flaw. In Zone 3 around the flaw, a highly refined mesh with $d = 0.4$ mm was created to properly capture the complex wave diffractions at the flaw boundaries (Figure 4.5).

The final mesh for the complete model is illustrated in Figure 4.6, showing the progression from the coarser mesh away from the flaw towards the more refined mesh close to the flaw. The parameters of the final mesh were as follows:

Total number of nodes: 2133430

Total number of elements: 1570347 Quadratic Tetrahedral of type C3D10M
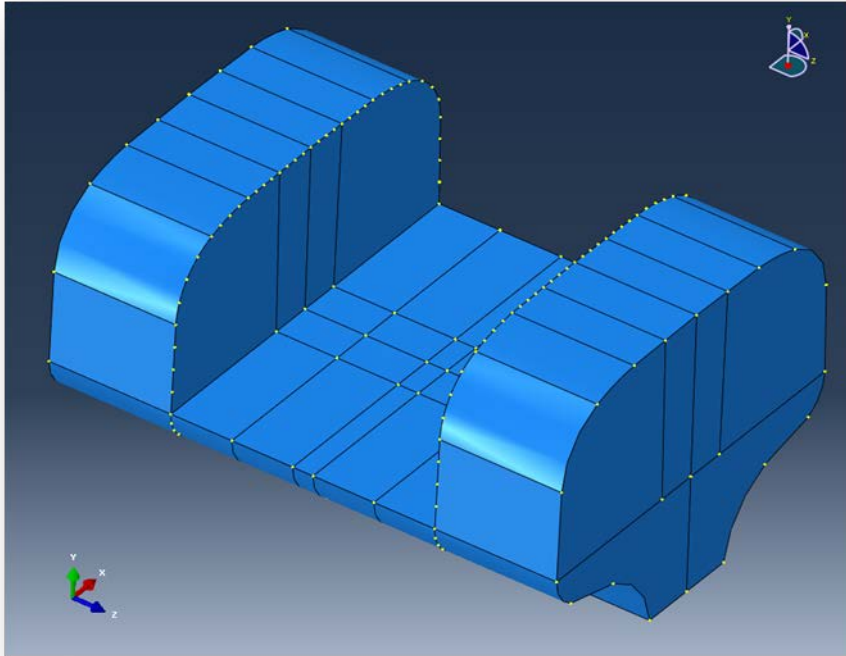
Figure 4.1. Zone 1 geometry – coarser mesh with element size *d* **= 3 mm for the 3-D FEA.**
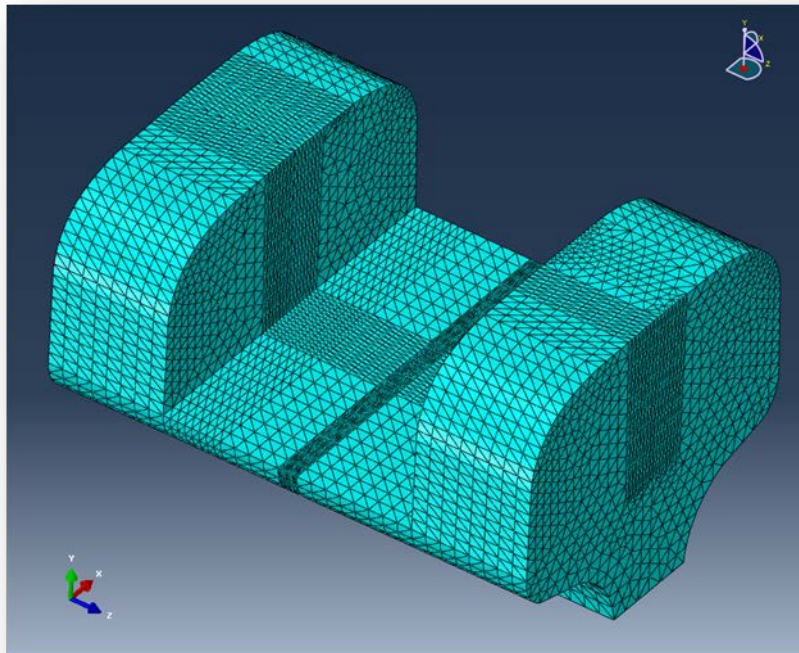
Figure 4.2. Zone 1 mesh – coarser mesh with element size *d* **= 3 mm for the 3-D FEA.**
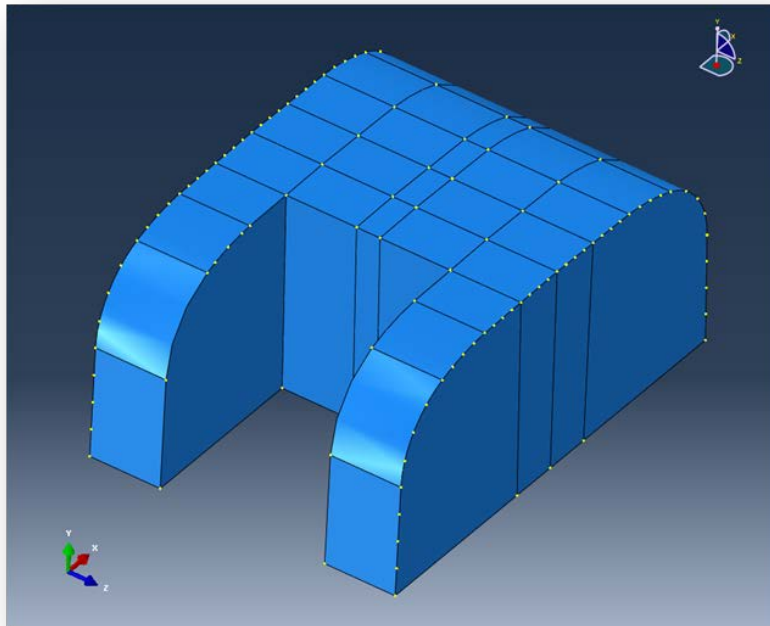
Figure 4.3. Zone 2 geometry – intermediate mesh with element size *d* = 1.5 mm for the 3-D FEA.
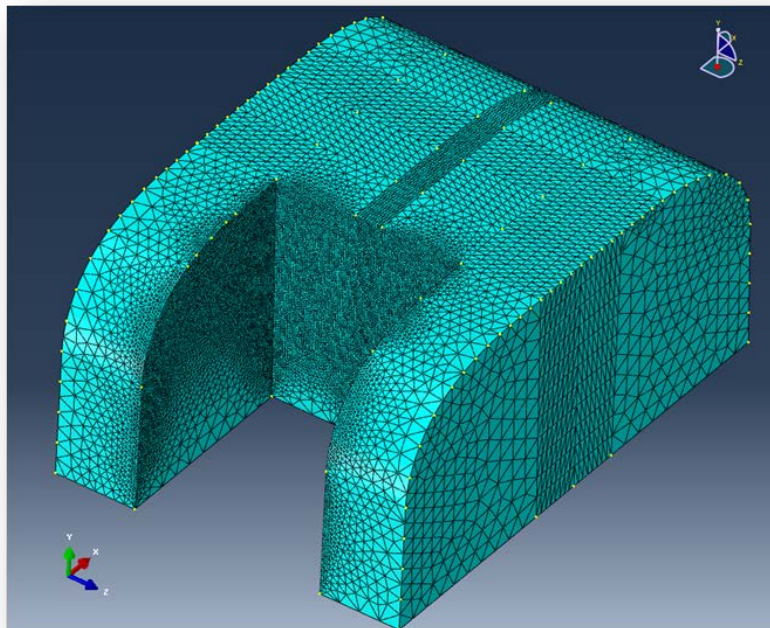
Figure 4.4. Zone 2 mesh – intermediate mesh with element size *d* = 1.5 mm for the 3-D FEA.
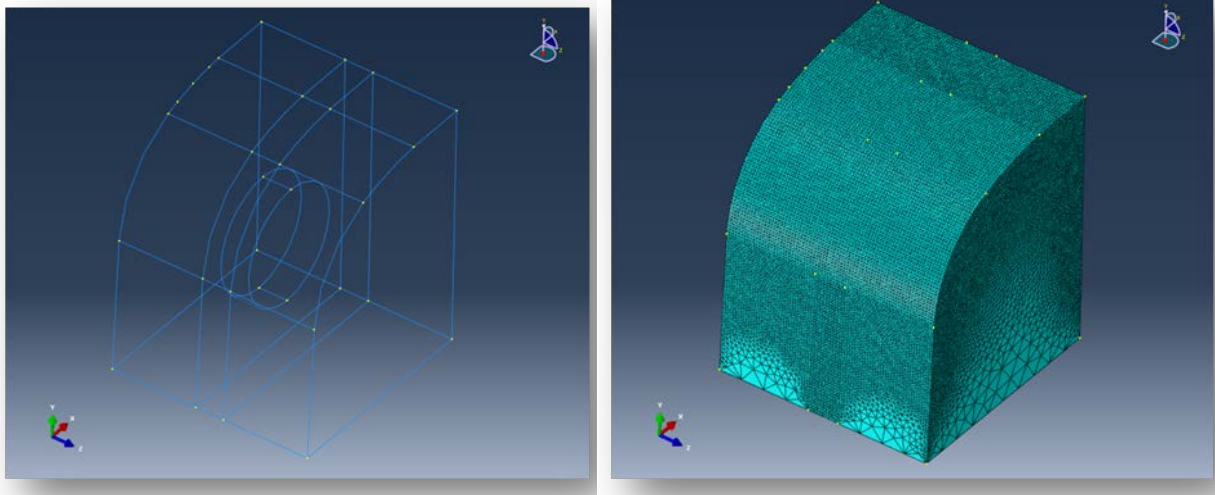
Figure 4.5. Zone 3 geometry and mesh – fine mesh with element size $d = 0.4$ mm for the 3-D FEA.
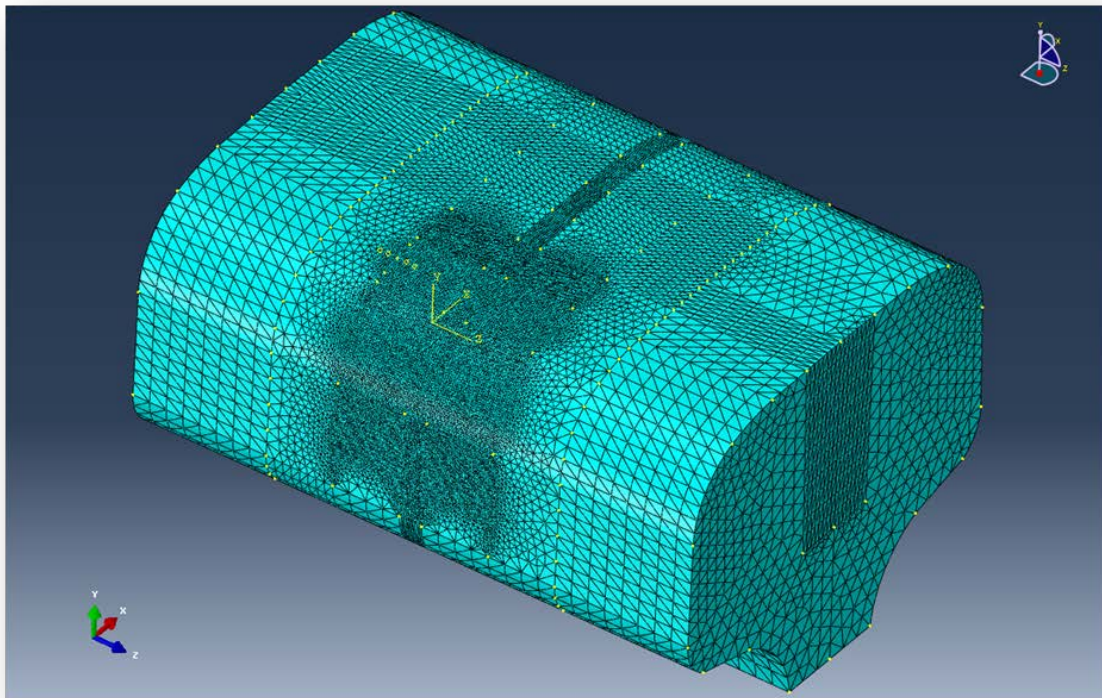
Figure 4.6. Entire mesh for the 3-D FEA. The TD is in the middle of the model in the gage corner area with the highest mesh refinement.

The base of the model was constrained with fixed boundaries (Figure 4.7).
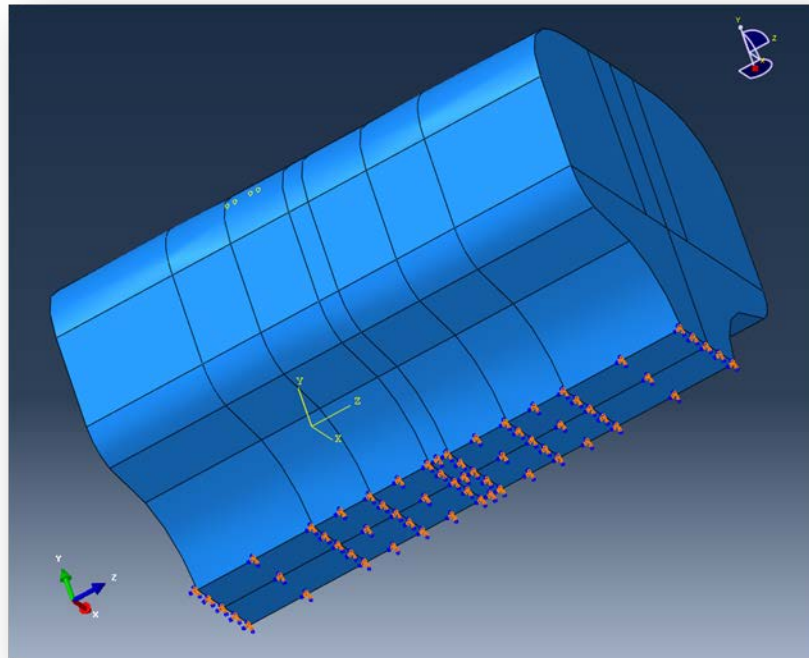
Figure 4.7. Boundary conditions for the 3-D FEA model.

The load was applied along a 0.25-inch line at the gage corner of the railhead (Figure 4.8). The load time history was one sinusoidal cycle at 2.25 MHz with nominal unity amplitude. The load vector was inclined at 70 degrees from the vertical (y-axis) direction. This inclination was given to simulate the typical 70-degree ultrasonic beam used in wheel and manual ultrasonic testing of rails for best detection of TDs.
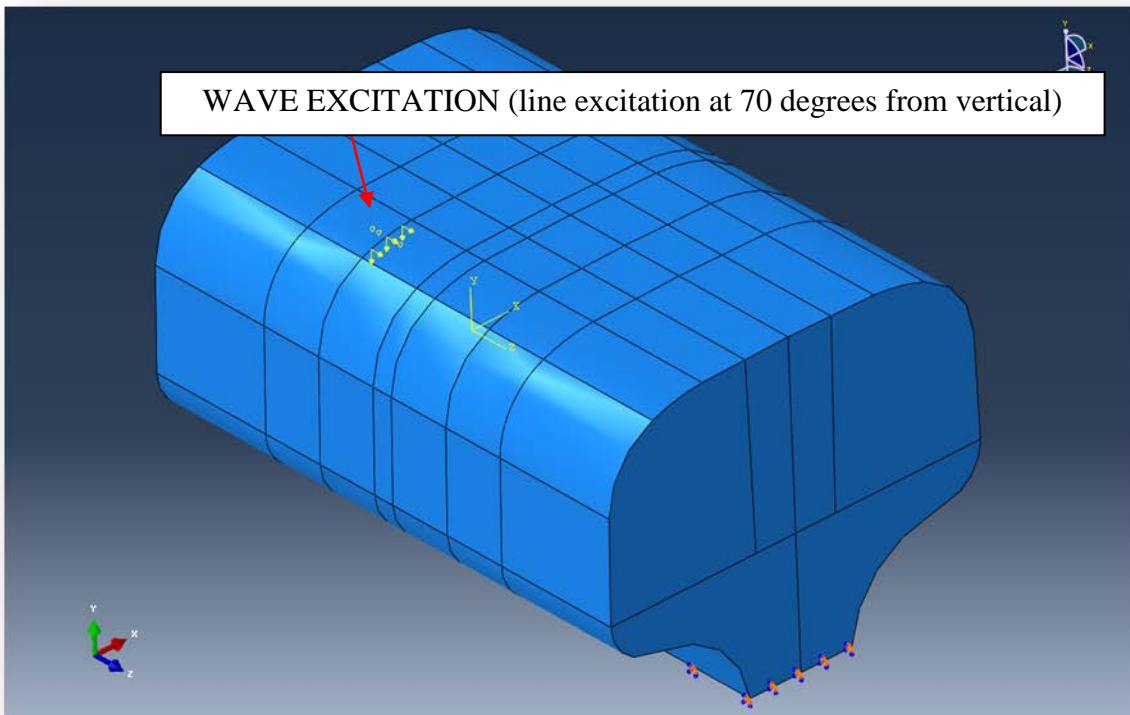
Figure 4.8. Excitation used for the 3-D FEA.

The same material properties adopted for the 2-D analysis were applied to the 3-D analysis. Hence:

Young's modulus $E = 209$ GPa

Poisson's ratio $\nu = 0.28$

Mass density $\rho = 7800$ kg/m^3

The analysis was developed in a single step using ABAQUS/Explicit code. The duration of the analysis was set to 30 μsec. The integration time required for the numerical stability of the solution was estimated based on the wave maximum frequency:

$\Delta t_{max} = 1 / (20 \ast f_{max}) = 0.0222$ μsec

4.2   Results of 3-D Finite Element Model

The following figures show the Von Mises Equivalent stress obtained at several times during the wave propagation. Figures 4.9 through 4.11 offer a global view, whereas Figures 4.12 through 4.14 show a sectional view. In these contour plots, the generation of the wave at early times can be seen clearly, along with the complex interaction of the wave with the 5-percent RHA TD at later times.
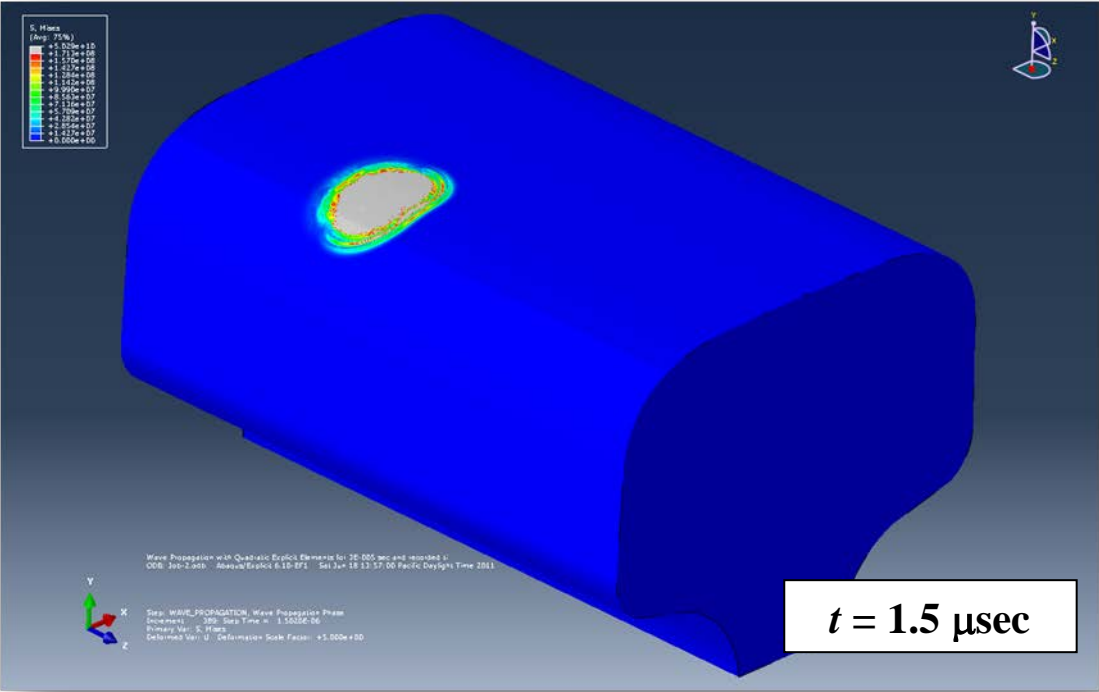
Figure 4.9.   Contour plots of Von Mises Equivalent Stress at *t* = 1.5 μsec after excitation from the 3-D FEA (global view).
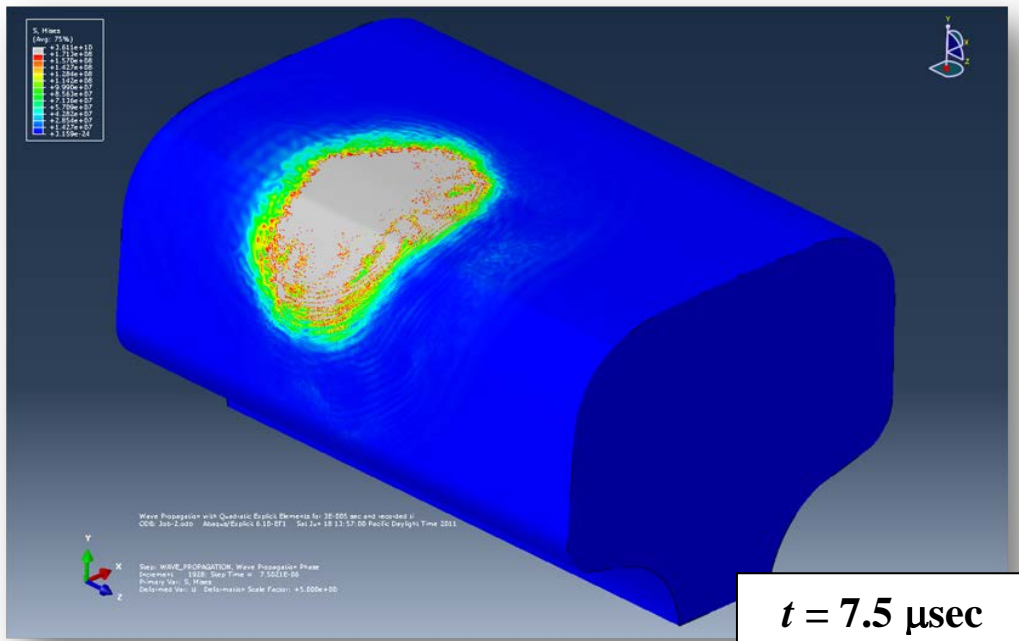
Figure 4.10. **Contour plots of Von Mises Equivalent Stress at** t = **7.5 μsec after excitation from the 3-D FEA (global view).**
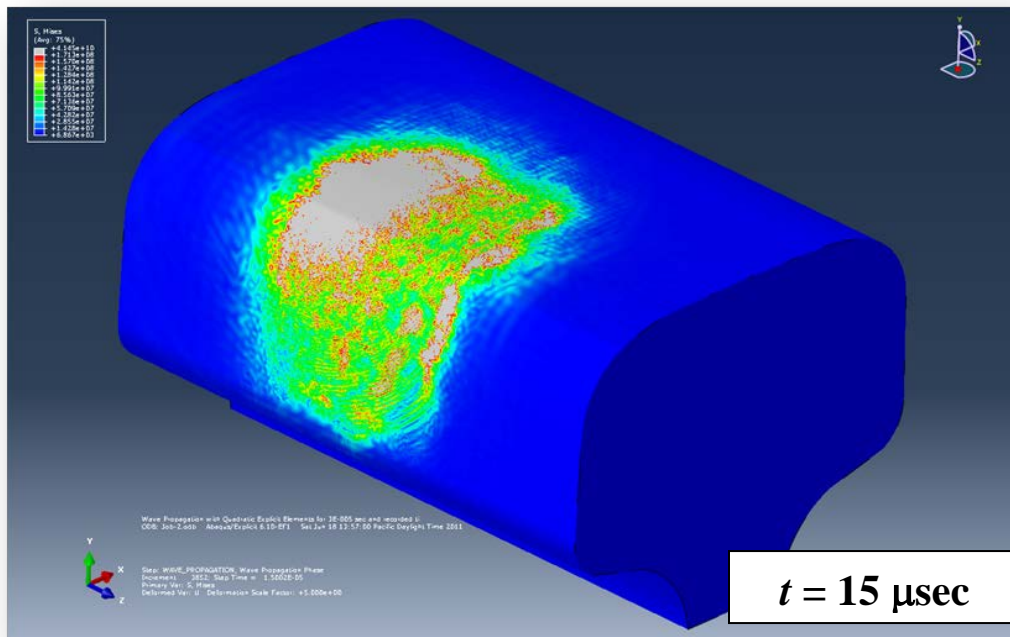
Figure 4.11. **Contour plots of Von Mises Equivalent Stress at** t = **15 μsec after excitation from the3-D FEA (global view).**
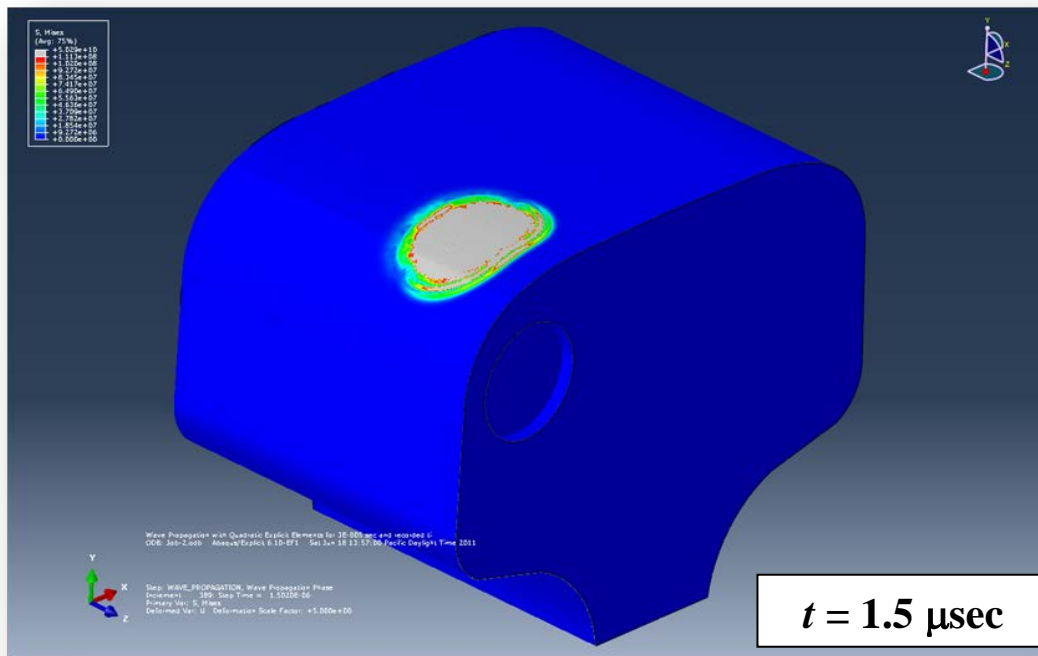
Figure 4.12. Contour plots of Von Mises Equivalent Stress at *t* = 1.5 μsec after excitation from the 3-D FEA (sectional view).
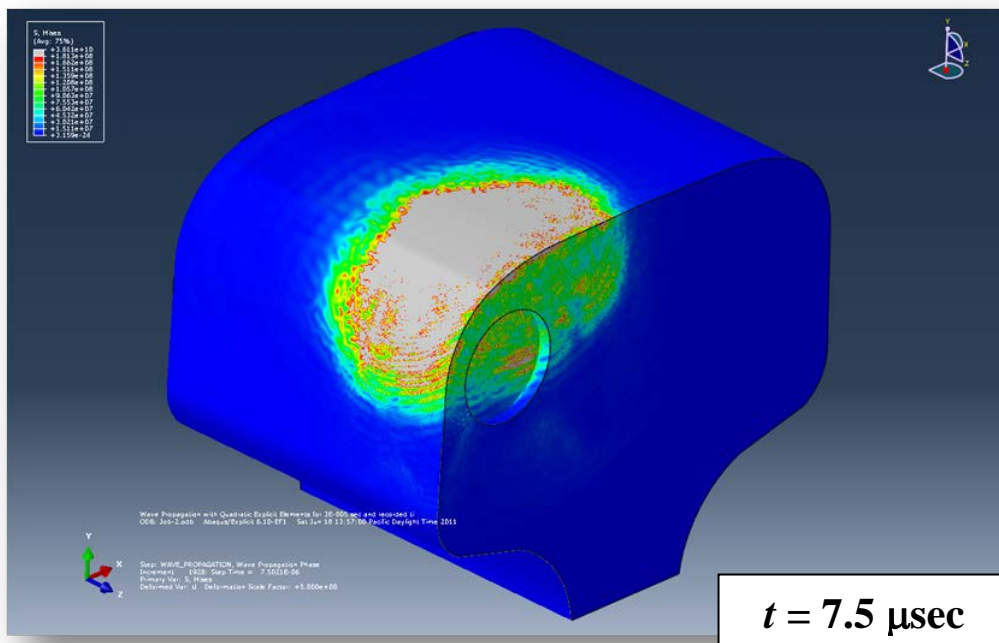
Figure 4.13. Contour plots of Von Mises Equivalent Stress at *t* = 7.5 μsec after excitation from the 3-D FEA (sectional view).

33
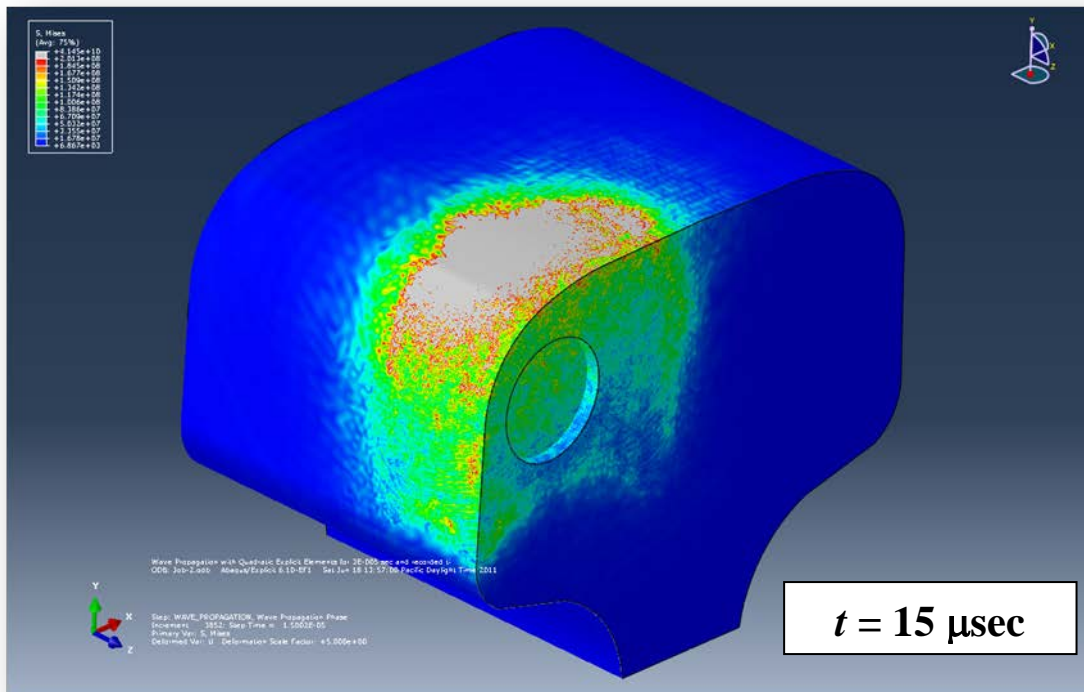
Figure 4.14. Contour plots of Von Mises Equivalent Stress at $t = 15$ μsec after excitation from the 3-D FEA (sectional view).

Two arrays of wave detection probes, wrapping around the railhead profile in the transverse direction, were chosen for this analysis. The arrays, shown in Figure 4.15, were positioned 2.6 cm away from one another on either side of the TD. These will be herein denoted as "rear" array and "front" array, respectively. Each of the arrays contained 57 nodal points where all the time histories were recorded. The choice of this particular configuration of detection points was motivated by the envisaged plan to study both reflection and transmission schemes for the ultrasonic tomographic system to be developed in subsequent phases. The numbering of the probe arrays is shown in Figures 4.16 and 4.17 for the "rear" array and the "front" array, respectively.
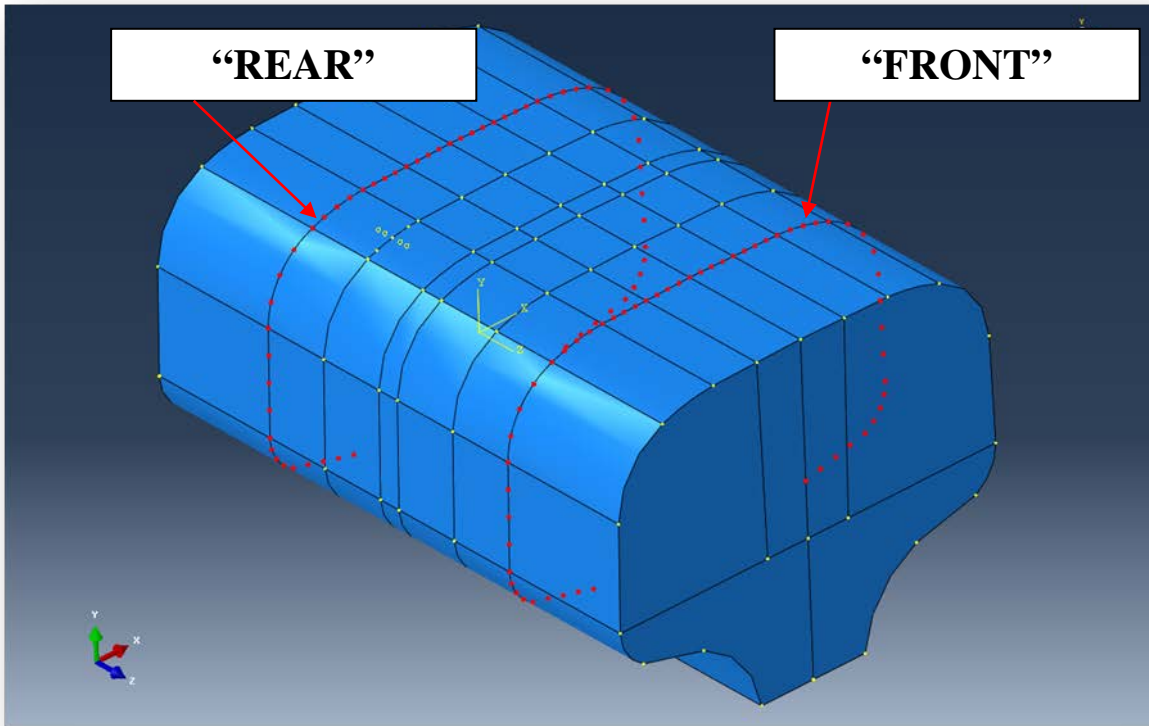
Figure 4.15. Location of the arrays of detection nodes for the wave time-history recordings. Each array contains 57 nodes.
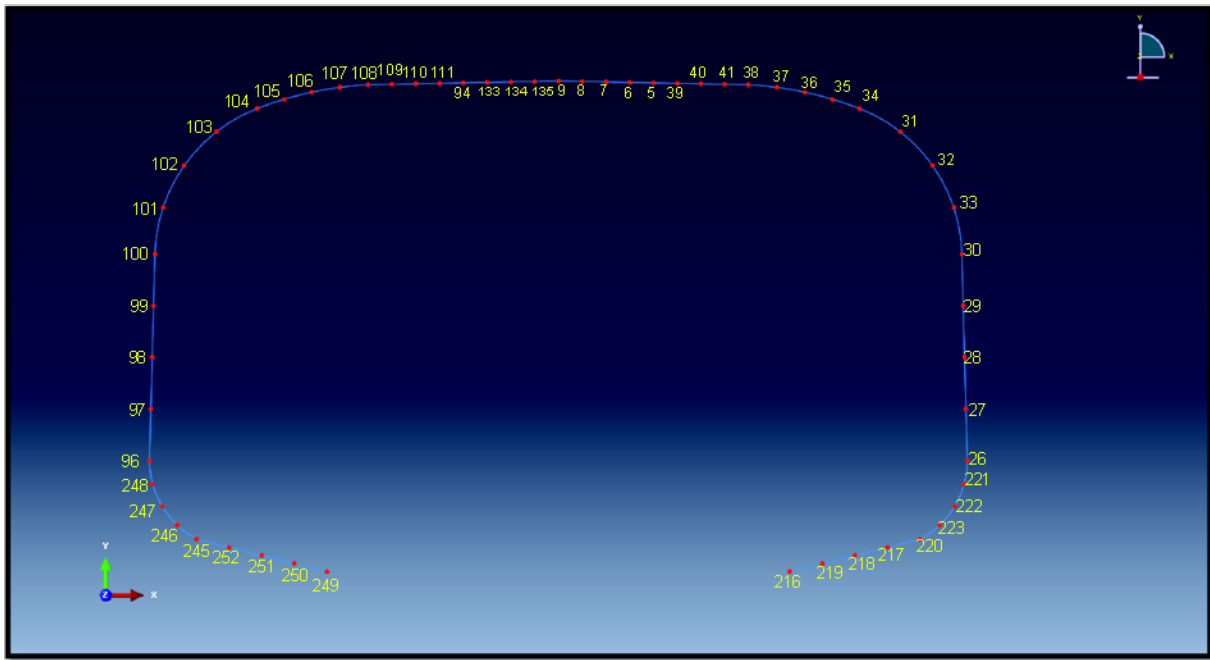
Figure 4.16. Numbering of nodes for the "rear" array.
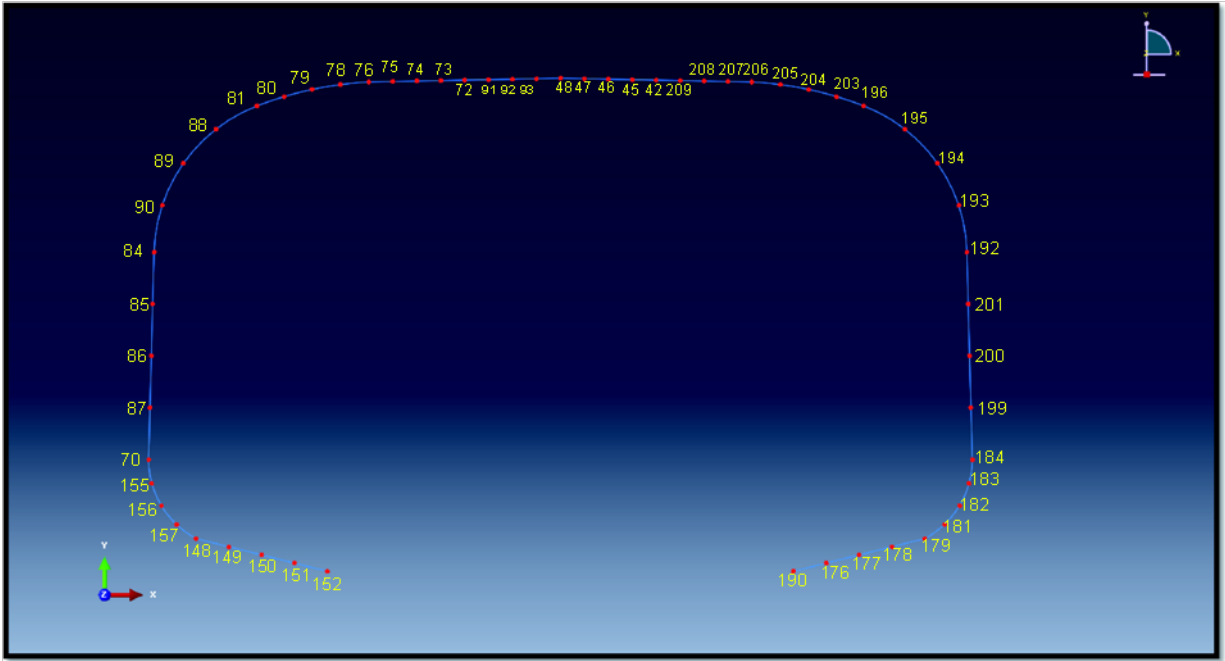
Figure 4.17. Numbering of nodes for the "front" array.

Figure 4.18 shows a sample of these results, specifically the time histories of the vertical displacement (u_y) for two nodes on the "rear" array prior to the defect (nodes 107 and 41), and two nodes on the "front" array past the defect (nodes 78 and 204). Multiple wave arrivals consisting of first arrivals plus reflections and refractions of waves from the flaw can be seen in these plots.
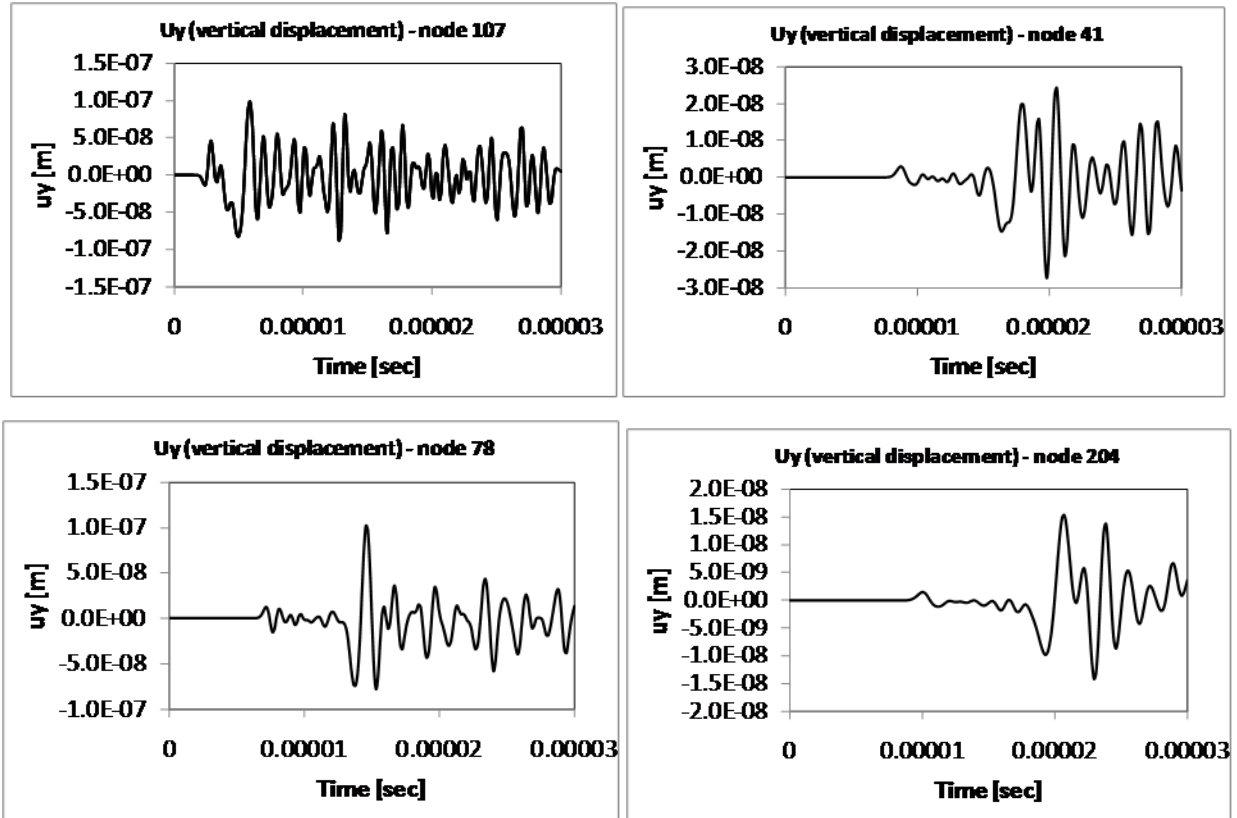
Figure 4.18. Time histories of vertical displacement recorded at sample nodes on the "rear" array (nodes 107 and 41) and at sample nodes on the "front" array (nodes 78 and 204).

4.3 FEA Convergence Study

A detailed convergence study at varying degrees of mesh refinements was also carried out to confirm the appropriateness of the chosen mesh to represent the interaction of the ultrasonic wave with the defect.

This study was carried out on the "most critical" mesh region of the 3-D model (i.e., Zone 3) or the area surrounding the defect. The discretization of the other two regions (Zone 1 – away from the defect, and Zone 2 – transition zone) were left unaltered from the 3-D model discussed in the previous section.

To check the convergence, a node close to the defect was analyzed in terms of recorded accelerations, velocities, and displacements, as discussed later in this section.

4.3.1 Meshes for Convergence Study

As discussed in the previous section, the entire 10 cm-long 3-D model of the rail was divided into three regions. The convergence study was only conducted on Zone 3 surrounding the defect because it provided the higher refinement requirements needed to properly model the wave diffraction close to the defect boundaries. Six different mesh refinements were studied in this region for convergence check.

The mesh in the unaltered Zones 1 and 2 is shown again in Figures 4.19 and 4.20, respectively, for clarity.
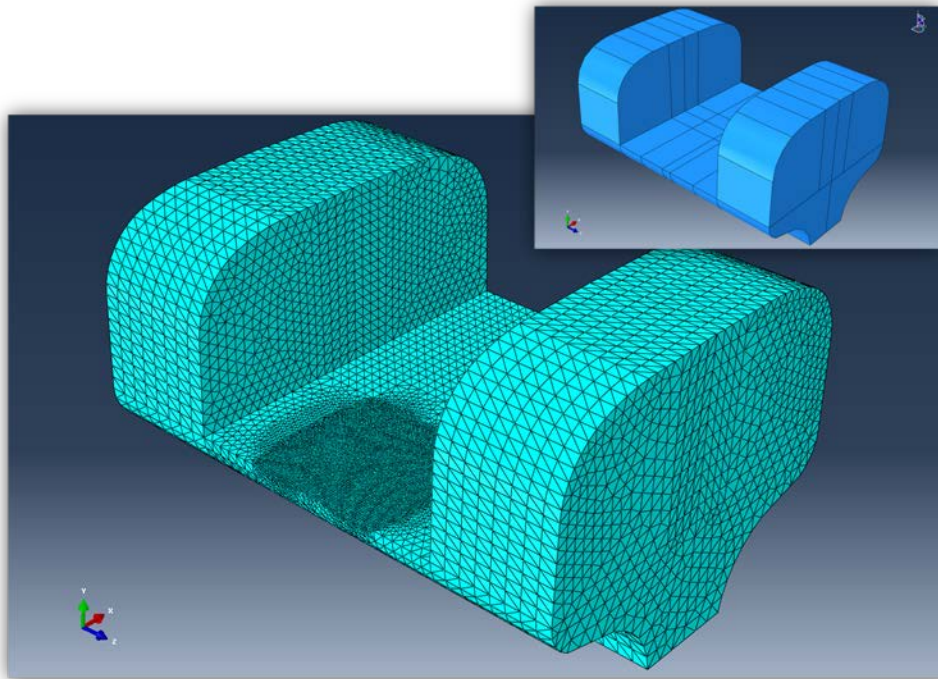
Figure 4.19. Coarse mesh in Zone 1 (maximum element size *d* = 3mm).
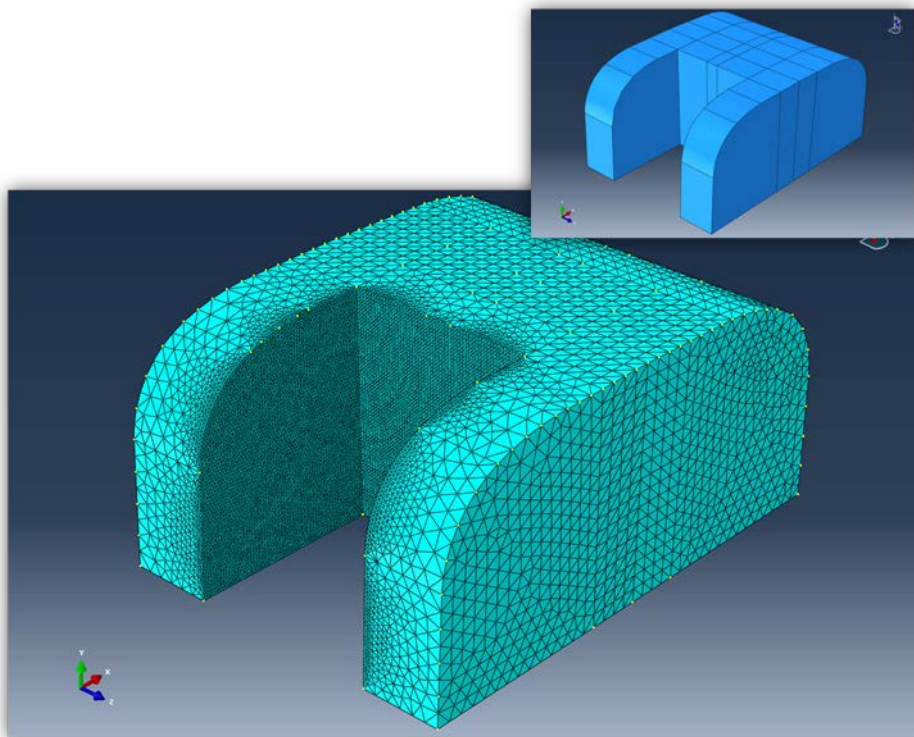
Figure 4.20. Transition mesh in Zone 2 (maximum element size *d* = 2mm).

The following figures (Figures 4.21 through 4.26) show the six levels of mesh refinements (Mesh 1 through Mesh 6) modeled for Zone 3 around the defect. The drawings are ordered from the most refined mesh (max. element size d = 0.5 mm) to the coarsest mesh (max element size d = 2.0 mm).
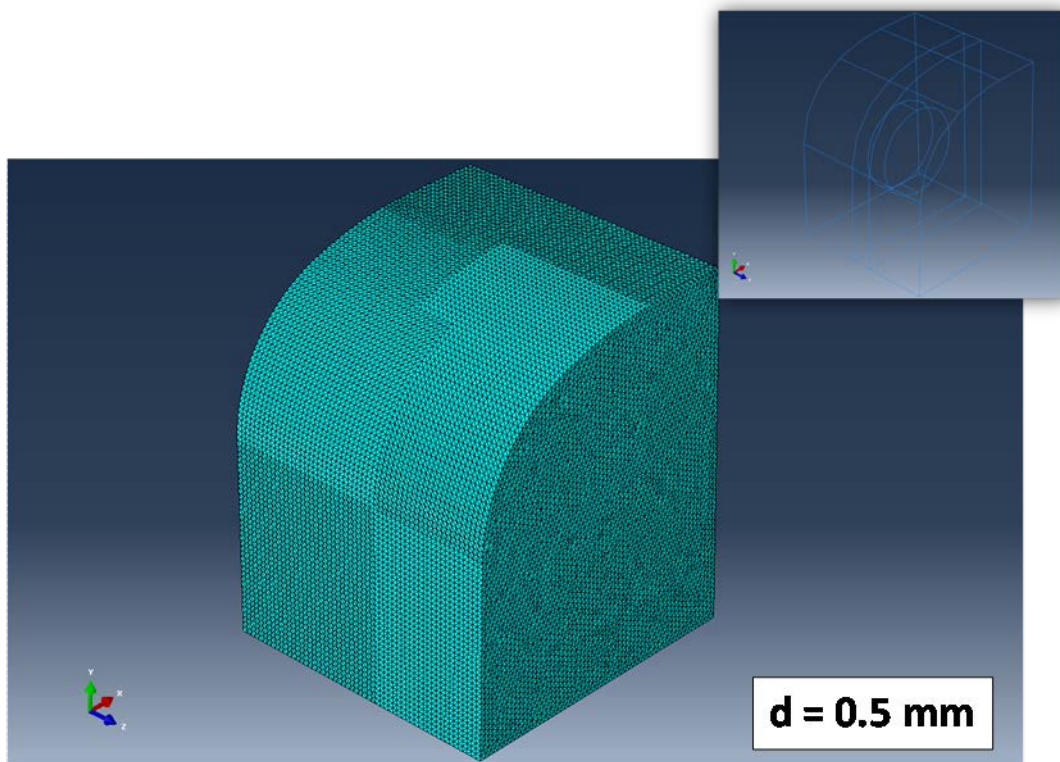
Figure 4.21. Mesh 1 in Zone 3 around the defect (maximum element size d = 0.5 mm).
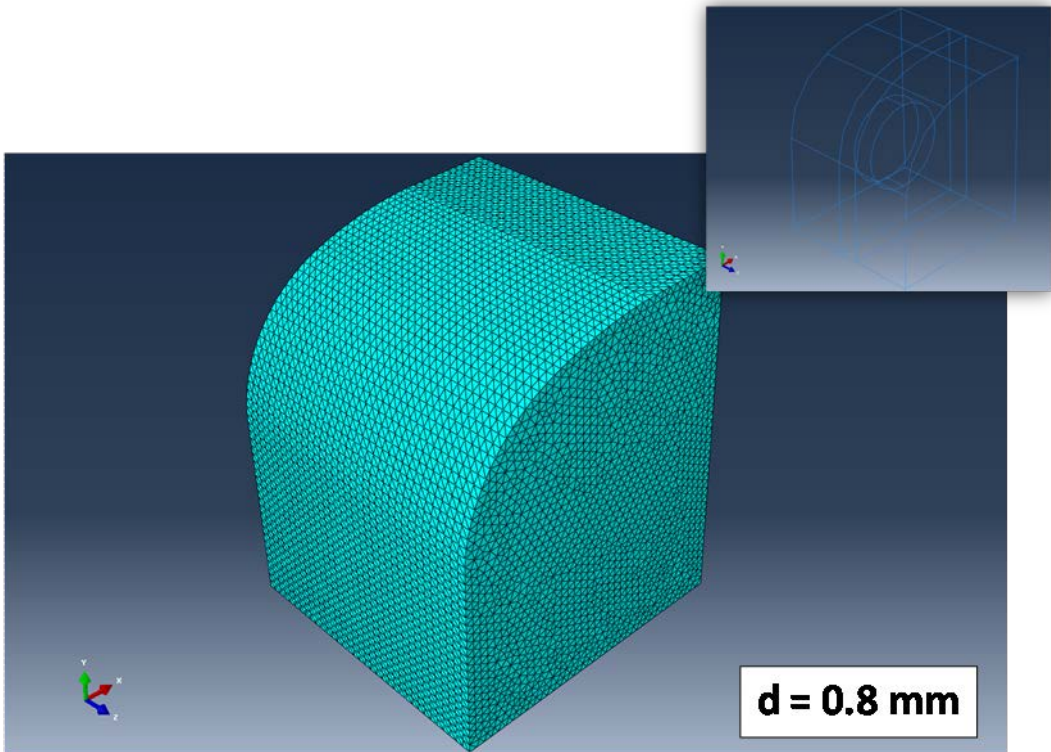
Figure 4.22. Mesh 2 in Zone 3 around the defect (maximum element size *d* = 0.8 mm).
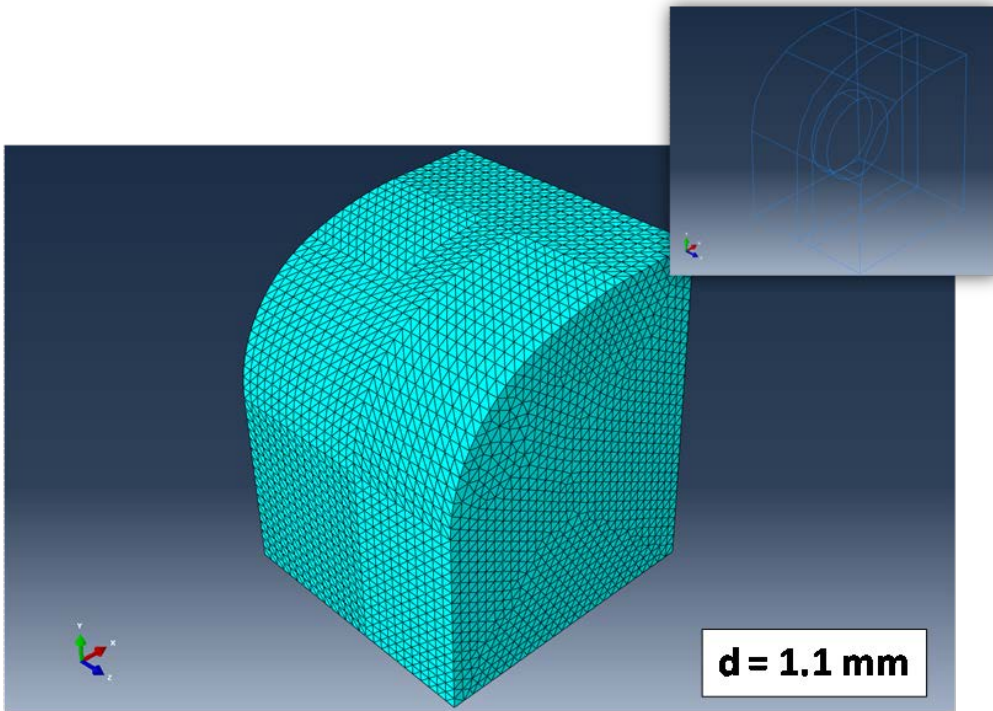
Figure 4.23. Mesh 3 in Zone 3 around the defect (maximum element size *d* = 1.1 mm).
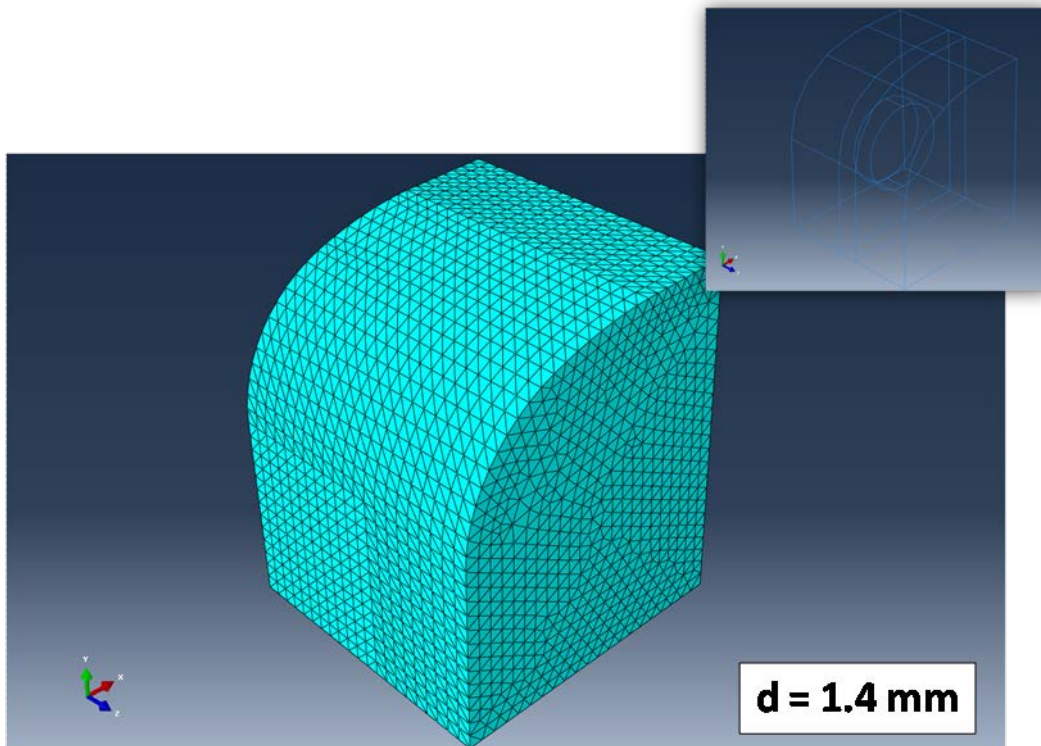
Figure 4.24. Mesh 4 in Zone 3 around the defect (maximum element size *d* = 1.4 mm).
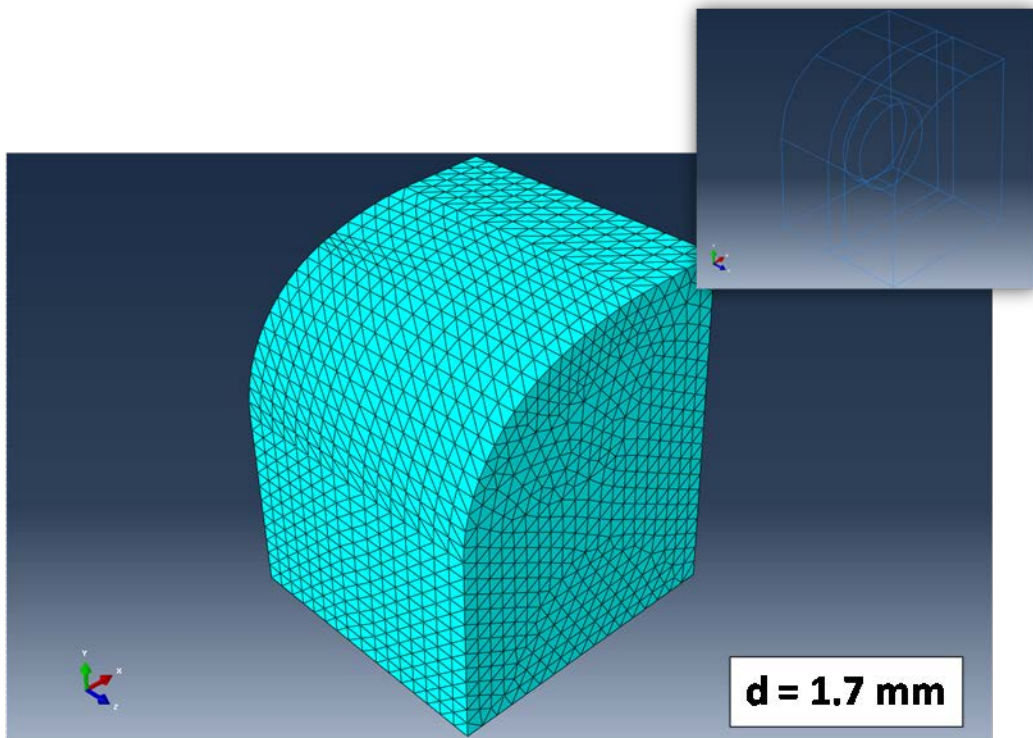
Figure 4.25. Mesh 5 in Zone 3 around the defect (maximum element size *d* = 1.7 mm).
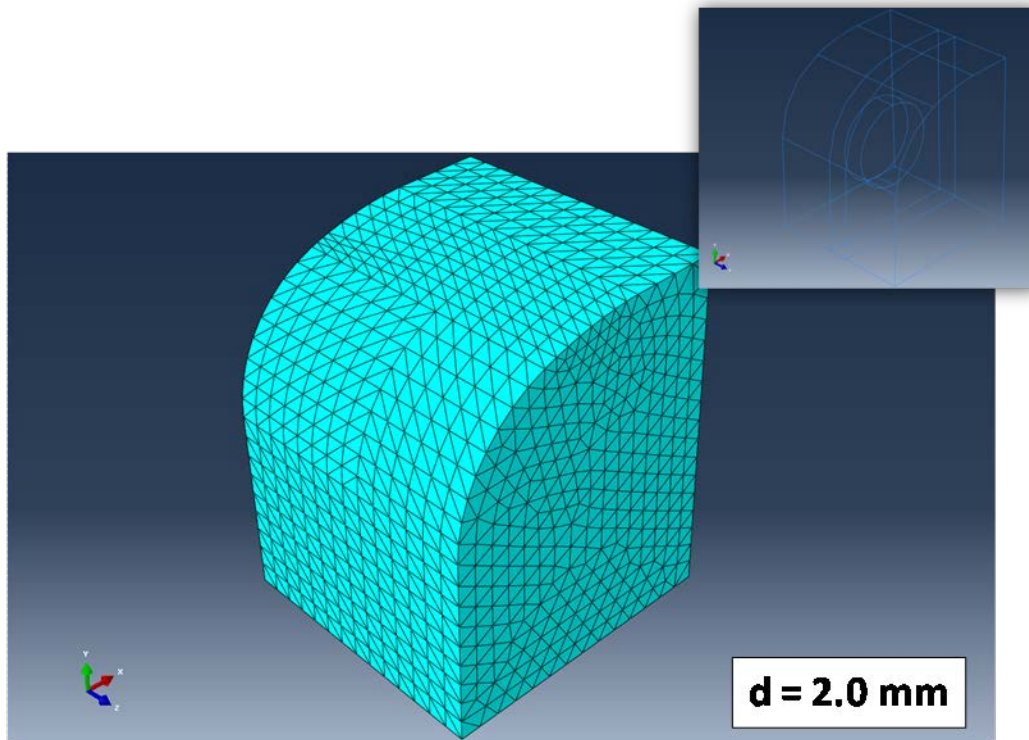
Figure 4.26. Mesh 6 in Zone 3 around the defect (maximum element size *d* = 2.0 mm).

All six cases used explicit tetrahedral elements with linear shape functions. The details of the six meshes are shown in the following:

MESH 1 – d_max around the defect = 0.5 mm

    Total number of nodes: 233,575

    Total number of elements: 1,367,021 Linear Tetrahedral of type C3D10M

MESH 2 – d_max around the defect = 0.8 mm

    Total number of nodes: 99,952

    Total number of elements: 577,885 Linear Tetrahedral of type C3D10M

MESH 3 – d_max around the defect = 1.1 mm

    Total number of nodes: 66,982

    Total number of elements: 383,988 Linear Tetrahedral of type C3D10M

MESH 4 – d_max around the defect = 1.4 mm

    Total number of nodes: 63,222

    Total number of elements: 362,540 Linear Tetrahedral of type C3D10M

MESH 5 – d_max around the defect = 1.7 mm

> *Total number of nodes: 52,347*

> *Total number of elements: 297,712 Linear Tetrahedral of type C3D10M*

MESH 6 – d_max around the defect = 2.0 mm

> *Total number of nodes: 41,548*

> *Total number of elements: 234,478 Linear Tetrahedral of type C3D10M*

Material properties (steel), boundary conditions (fixed base), and forcing function (one sinusoidal cycle at 2.25 MHz, unity amplitude, at gage corner, inclined at 70 degrees from vertical axis *y*) were unchanged from the 3-D model discussed in the previous section. Also, the same time increment requirement was used to properly represent 2.25 MHz frequencies, hence $\Delta t_{max} = 0.0222$ μsec.

4.3.2 Results of Convergence Study

A node close to the defect was chosen as a probe to analyze the behavior of the different meshes. The position of the "probe node" is shown in two different views in Figures 4.27 and 4.28.
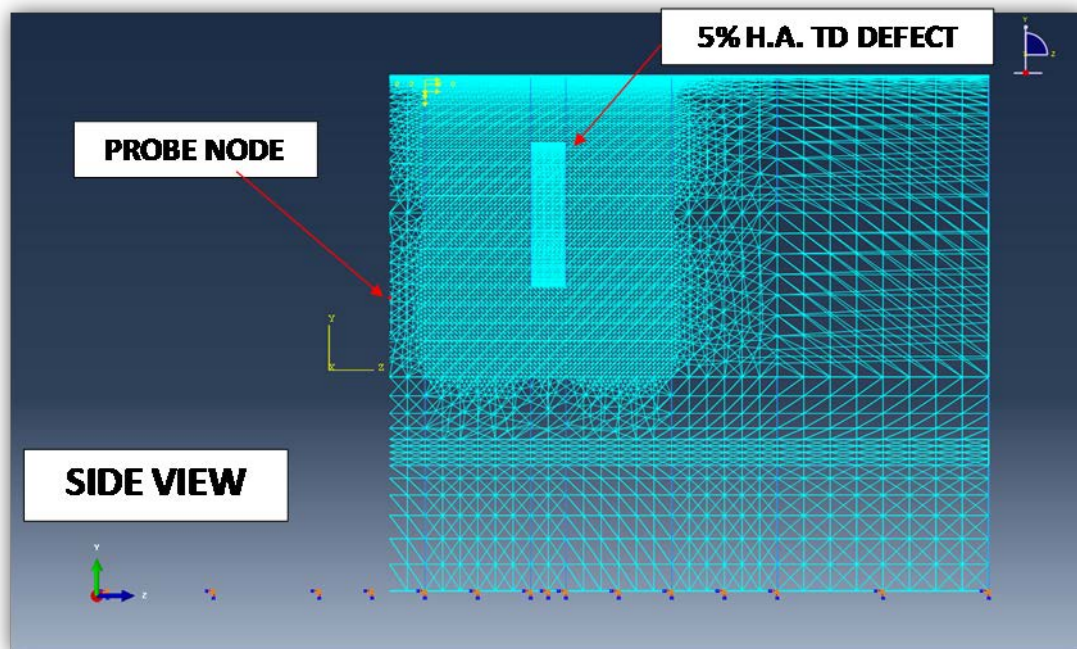
Figure 4.27. Position of the probe node for convergence study – side view.
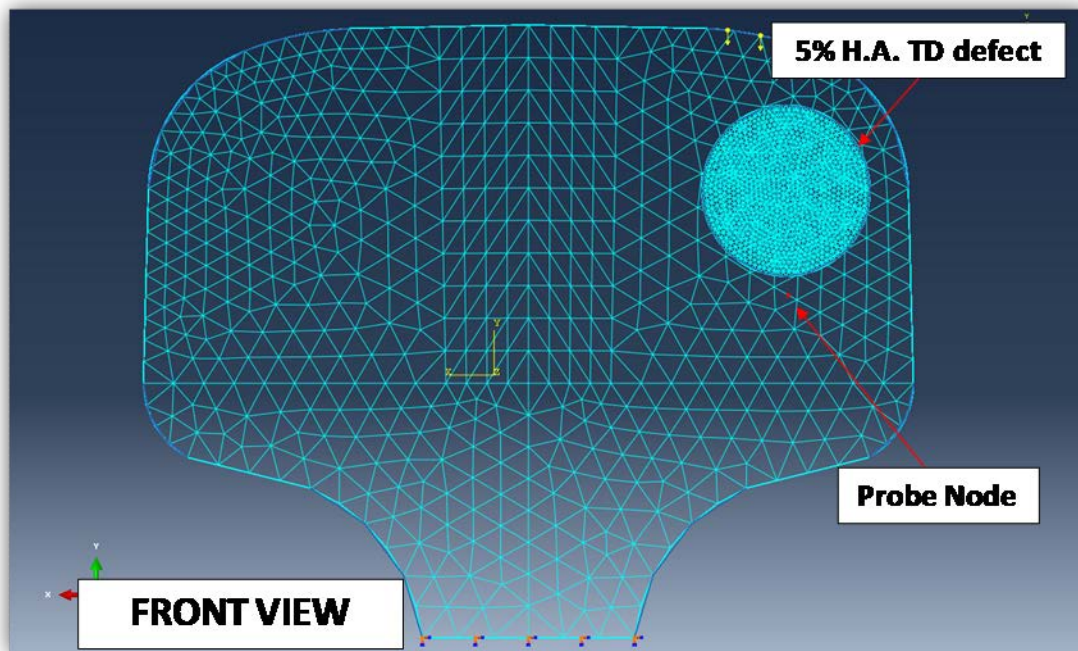
Figure 4.28. Position of the probe node for convergence study – front view.

For each of the six meshes, the following kinematic quantities were recorded at the Probe Node: accelerations (x, y and z), velocities (x, y and z), and displacements (x, y and z). The time histories of these quantities recorded with each mesh are shown in Figures 4.29 through 4.34. In these plots the first row refers to the accelerations a_x, a_y and a_z; the second row to the velocities v_x, v_y and v_z; and the third row to the displacements u_x, u_y and u_z.
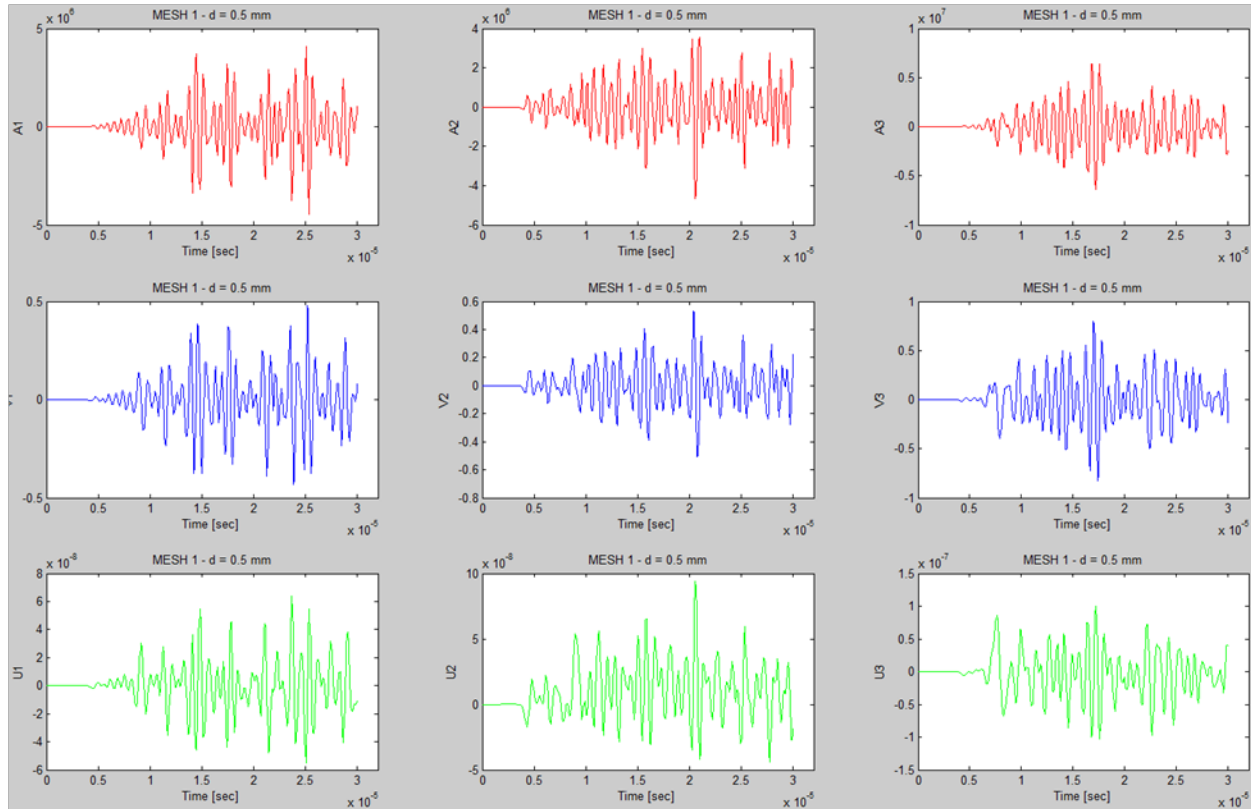
Figure 4.29. Time histories of accelerations a_x, a_y and a_z (first row), velocities v_x, v_y and v_z (second row), and displacements u_x, u_y and u_z (third row) recorded at the Probe Node for convergence study using Mesh 1 in Zone 3 around the defect (maximum element size $d = 0.5$ mm).
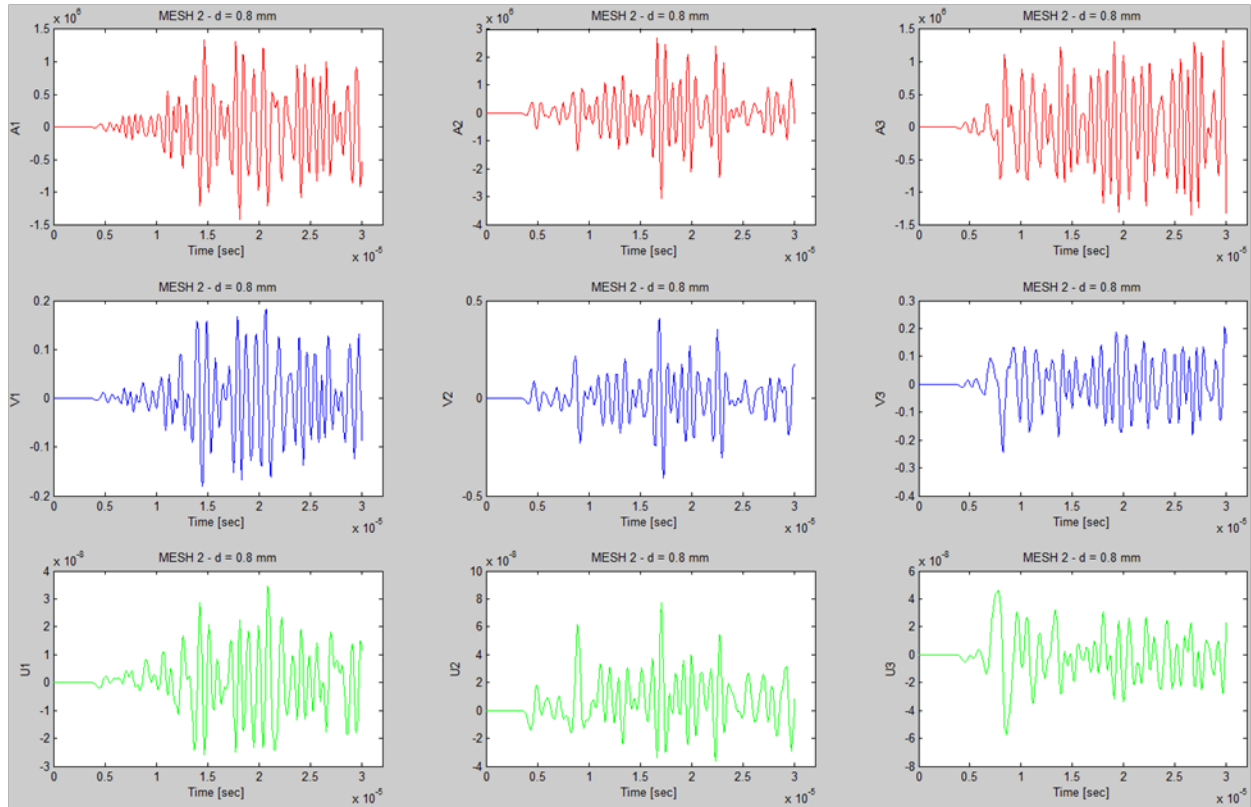
Figure 4.30. Time histories of accelerations a_x, a_y and a_z (first row), velocities v_x, v_y and v_z (second row), and displacements u_x, u_y and u_z (third row) recorded at the Probe Node for convergence study using Mesh 2 in Zone 3 around the defect (maximum element size $d = 0.8$ mm).
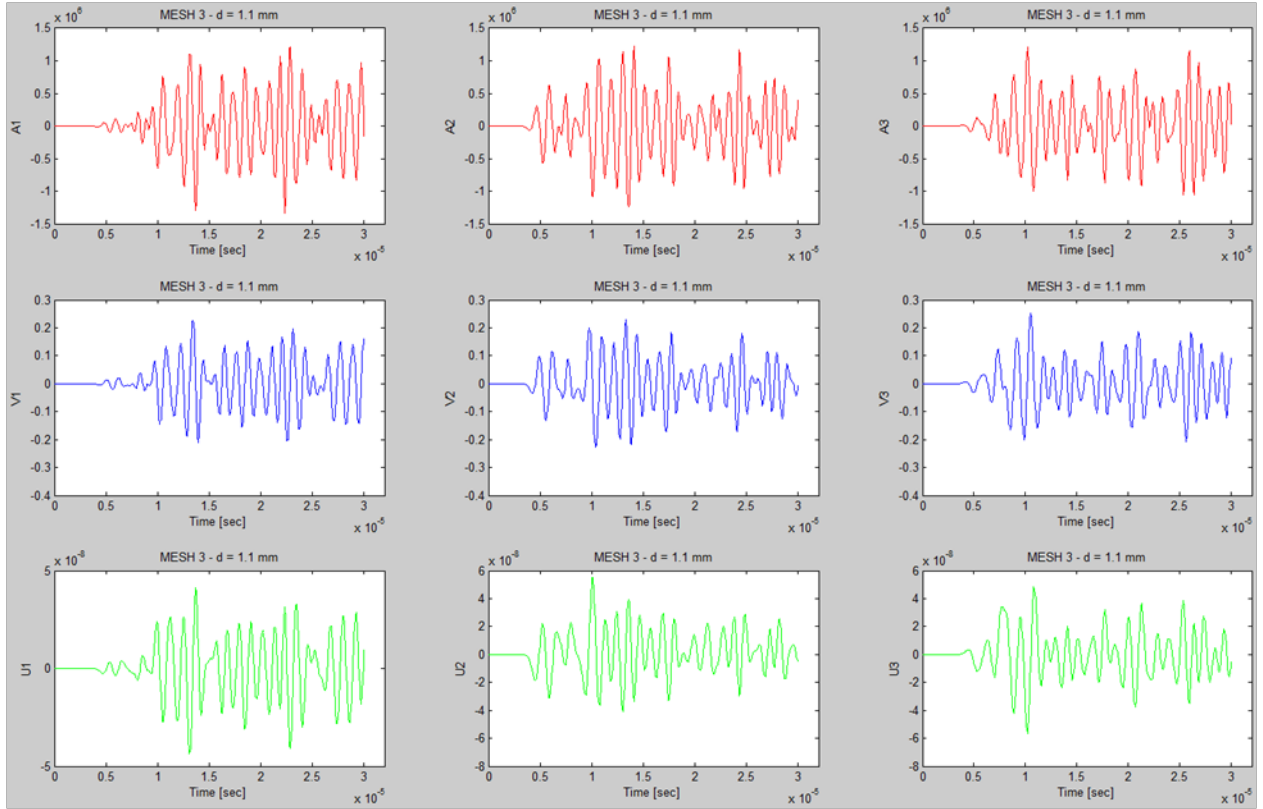
Figure 4.31. Time histories of accelerations a_x, a_y and a_z (first row), velocities v_x, v_y and v_z (second row), and displacements u_x, u_y and u_z (third row) recorded at the Probe Node for convergence study using Mesh 3 in Zone 3 around the defect (maximum element size $d = 1.1$ mm).
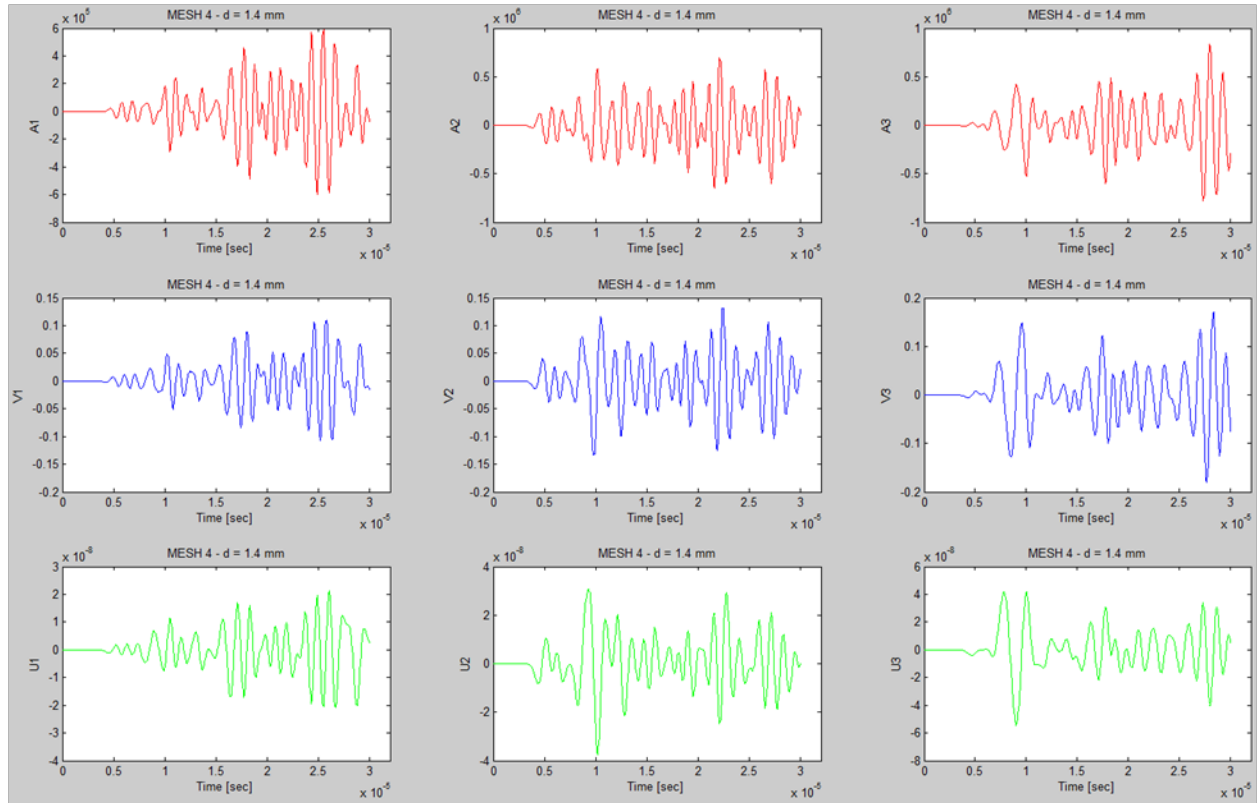
Figure 4.32. Time histories of accelerations a_x, a_y and a_z (first row), velocities v_x, v_y and v_z (second row), and displacements u_x, u_y and u_z (third row) recorded at the Probe Node for convergence study using Mesh 4 in Zone 3 around the defect (maximum element size $d = 1.4$ mm).
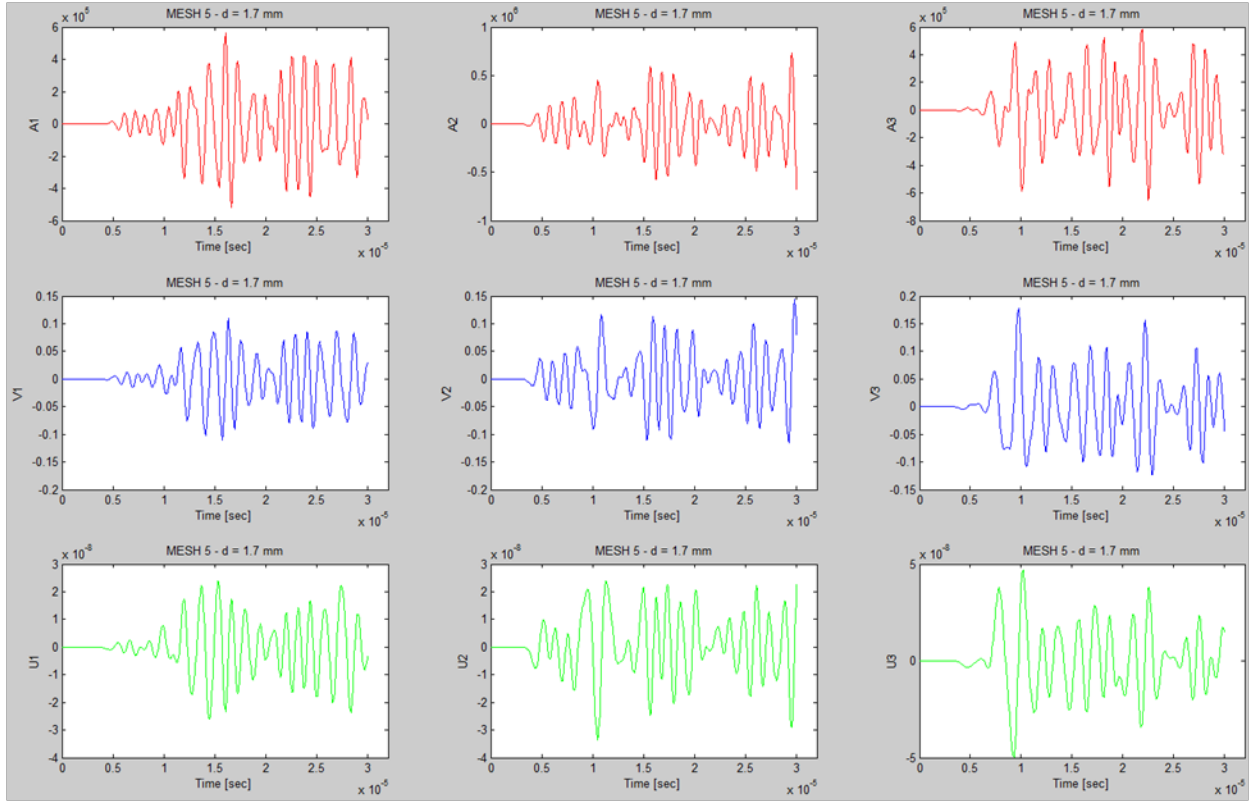
Figure 4.33. Time histories of accelerations a_x, a_y and a_z (first row), velocities v_x, v_y and v_z (second row), and displacements u_x, u_y and u_z (third row) recorded at the Probe Node for convergence study using Mesh 5 in Zone 3 around the defect (maximum element size $d = 1.7$ mm).
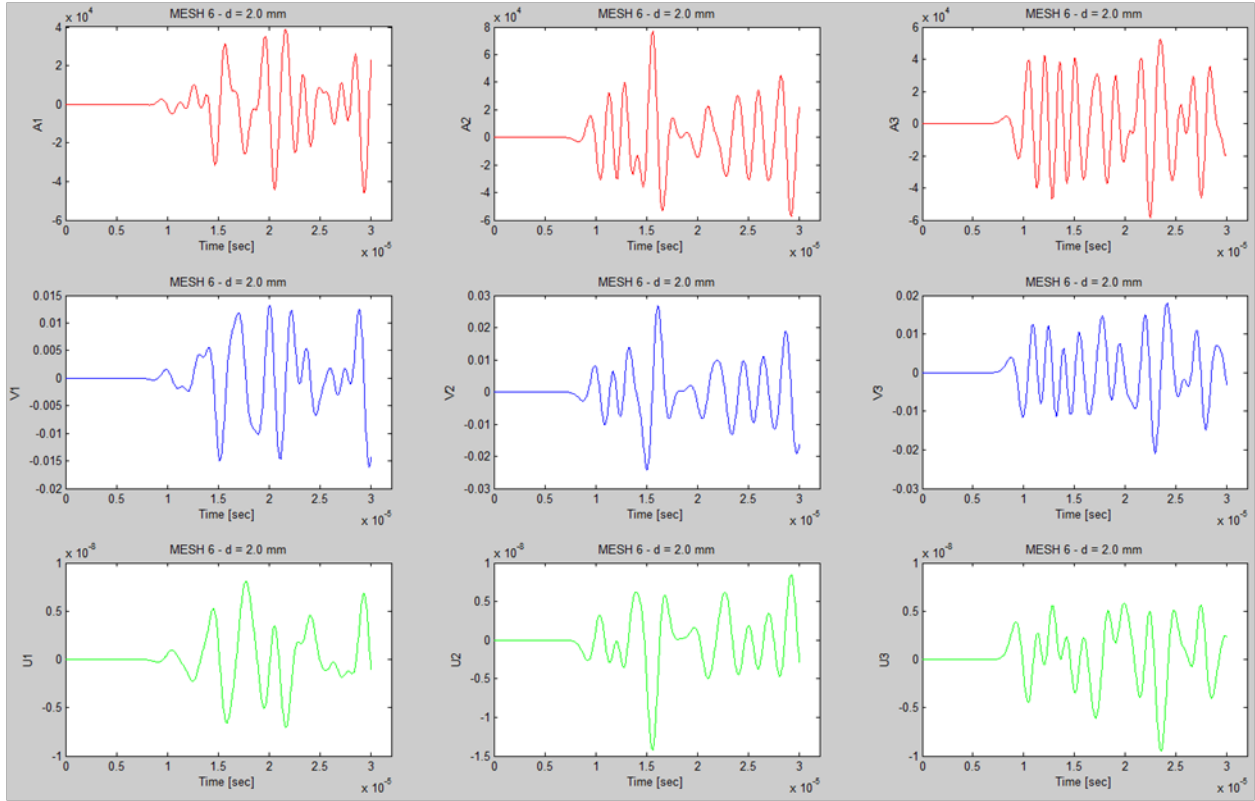
Figure 4.34. Time histories of accelerations a_x, a_y and a_z (first row), velocities v_x, v_y and v_z (second row), and displacements u_x, u_y and u_z (third row) recorded at the Probe Node for convergence study using Mesh 6 in Zone 3 around the defect (maximum element size $d = 2.0$ mm).

Following zero-padding to increase the frequency resolution, these time histories were processed through a Fast Fourier Transform (FFT) for frequency information. The following figures (Figure 4.35 through 4.43) show the FFT magnitude spectra recorded for each of the nine kinematic quantities (a_x, a_y, a_z, v_x, v_y, v_z and u_x, u_y, u_z) for the six different mesh refinements.

What is apparent in these plots, as expected, is that the finer the mesh, the better the representation of the higher frequency components. The coarsest mesh, mesh 6 of $d = 2.0$ mm, for example, only properly represents frequency components up to ~ 1 MHz. In order to properly represent the excitation frequency of 2.25 MHz, the most refined mesh, mesh 1 with $d = 0.5$ mm, is required. Use of a mesh coarser than $d = 0.5$ mm around the defect would not be adequate to represent the high frequency waves. This study therefore gives confidence in the results shown in the previous section (Section 3) obtained with the mesh of $d = 0.4$ mm in Zone 3.

51
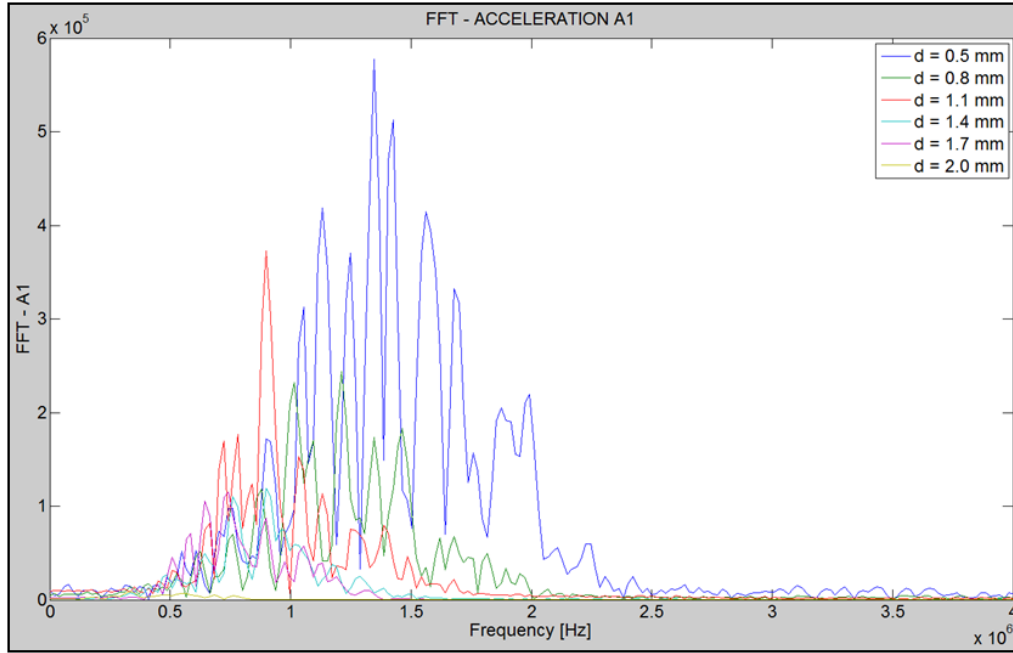
Figure 4.35. Fast Fourier Transform magnitude spectra recorded at the Probe Node for acceleration a_x for the six different meshes considered in the convergence study.
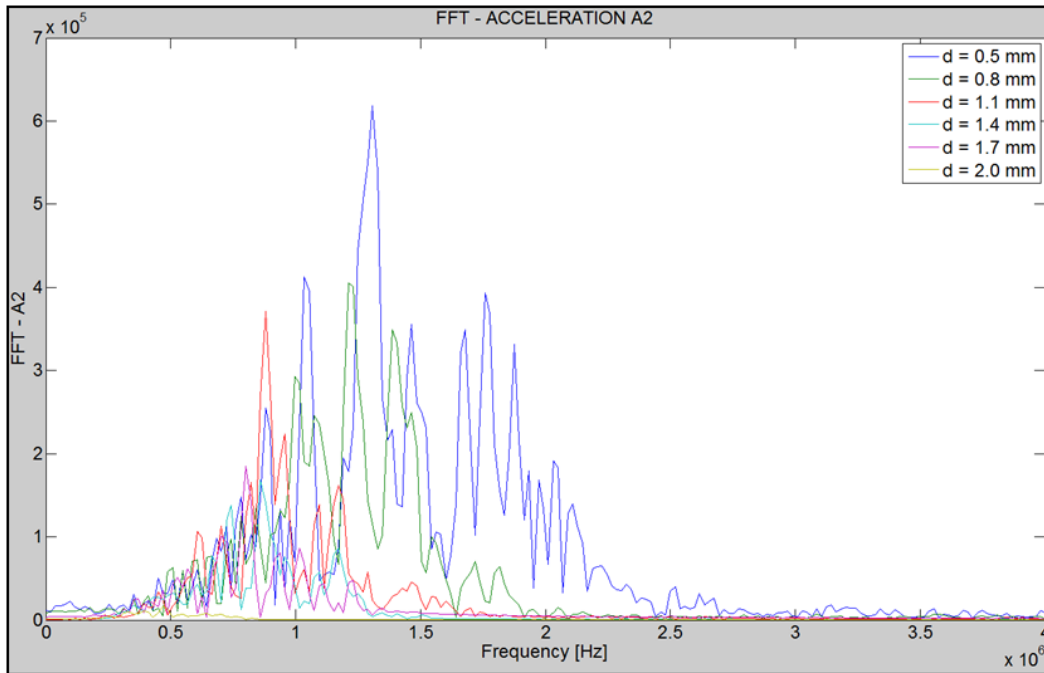
Figure 4.36. Fast Fourier Transform magnitude spectra recorded at the Probe Node for acceleration a_y for the six different meshes considered in the convergence study.
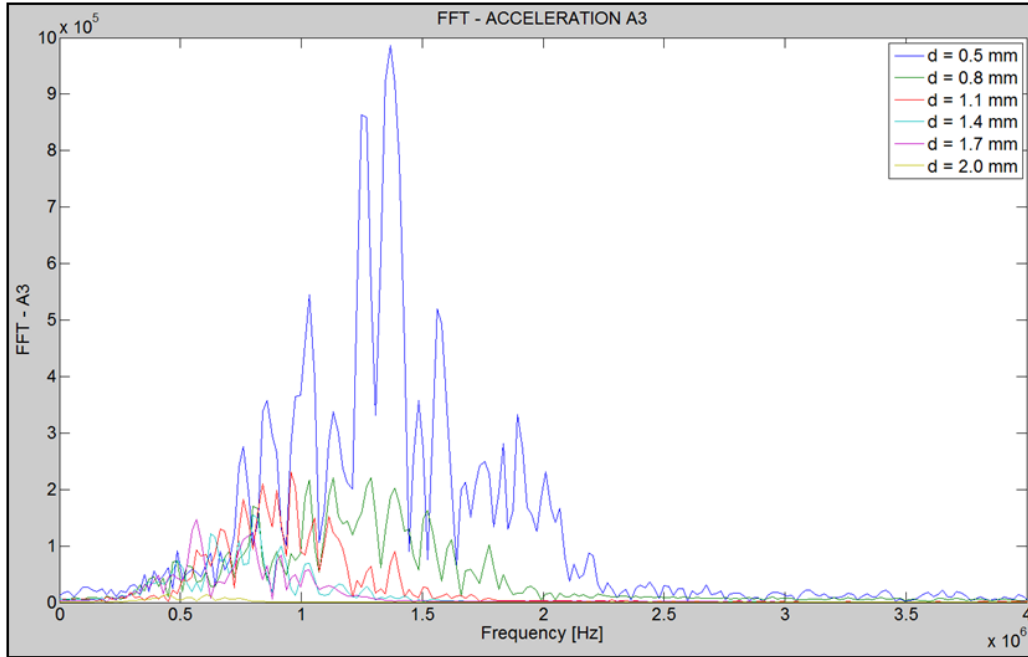
Figure 4.37. Fast Fourier Transform magnitude spectra recorded at the Probe Node for acceleration a_z for the six different meshes considered in the convergence study.
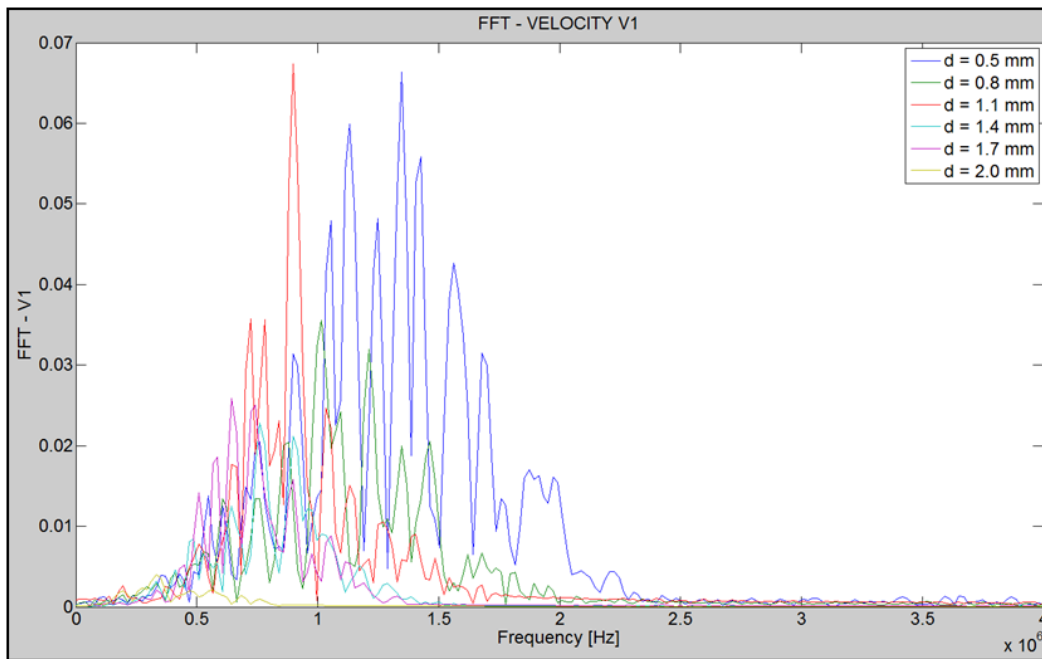
Figure 4.38. Fast Fourier Transform magnitude spectra recorded at the Probe Node for velocity v_x for the six different meshes considered in the convergence study.

53
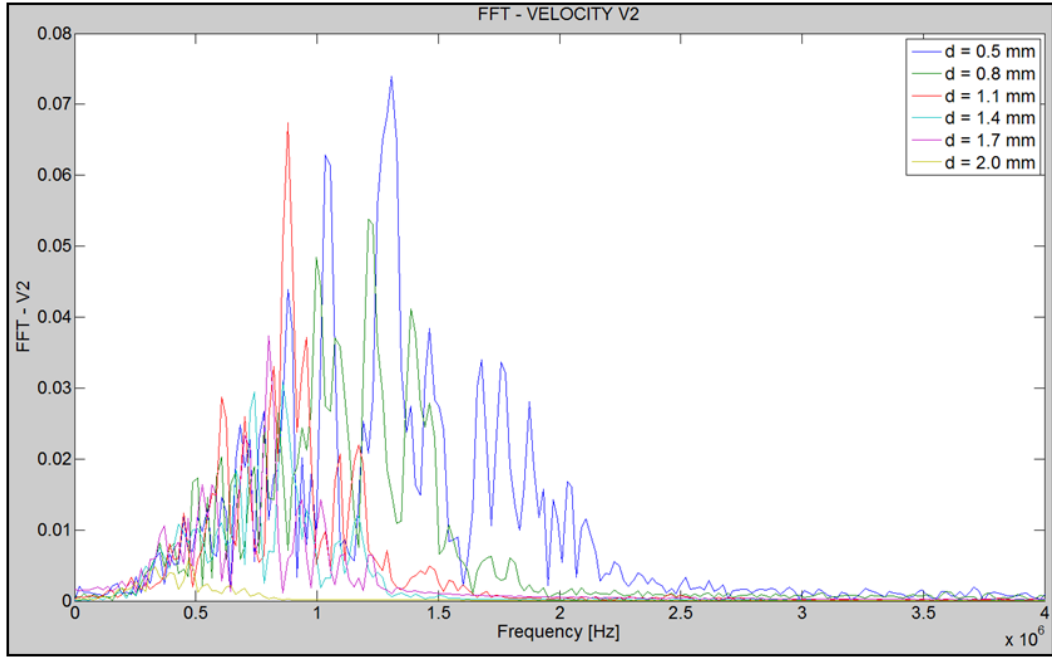
Figure 4.39. Fast Fourier Transform magnitude spectra recorded at the Probe Node for velocity v_y for the six different meshes considered in the convergence study.
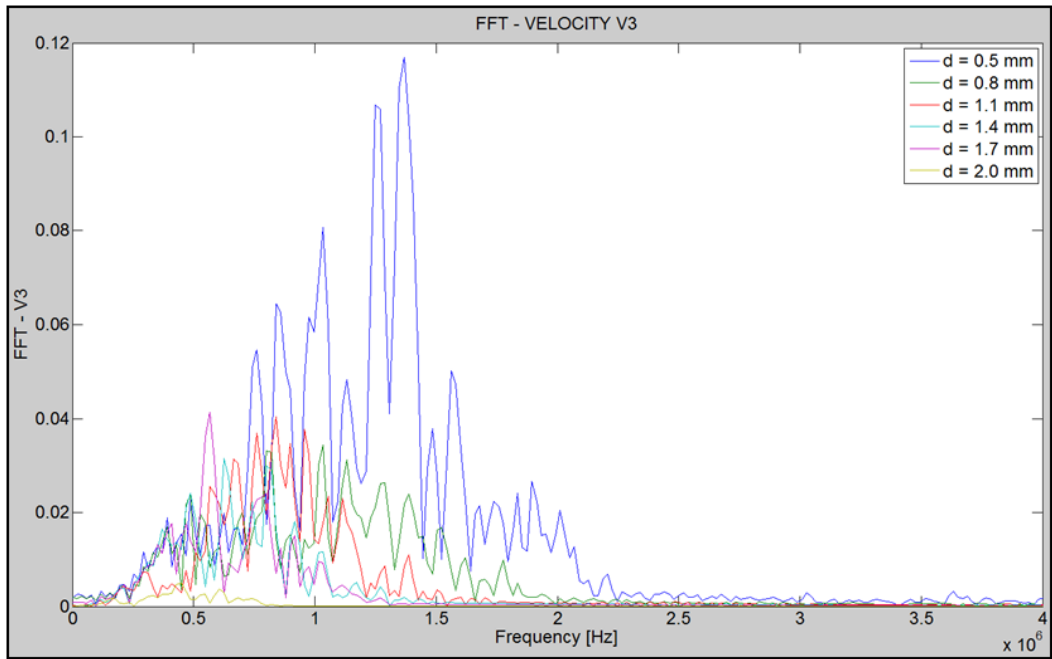
Figure 4.40. Fast Fourier Transform magnitude spectra recorded at the Probe Node for velocity v_z for the six different meshes considered in the convergence study.
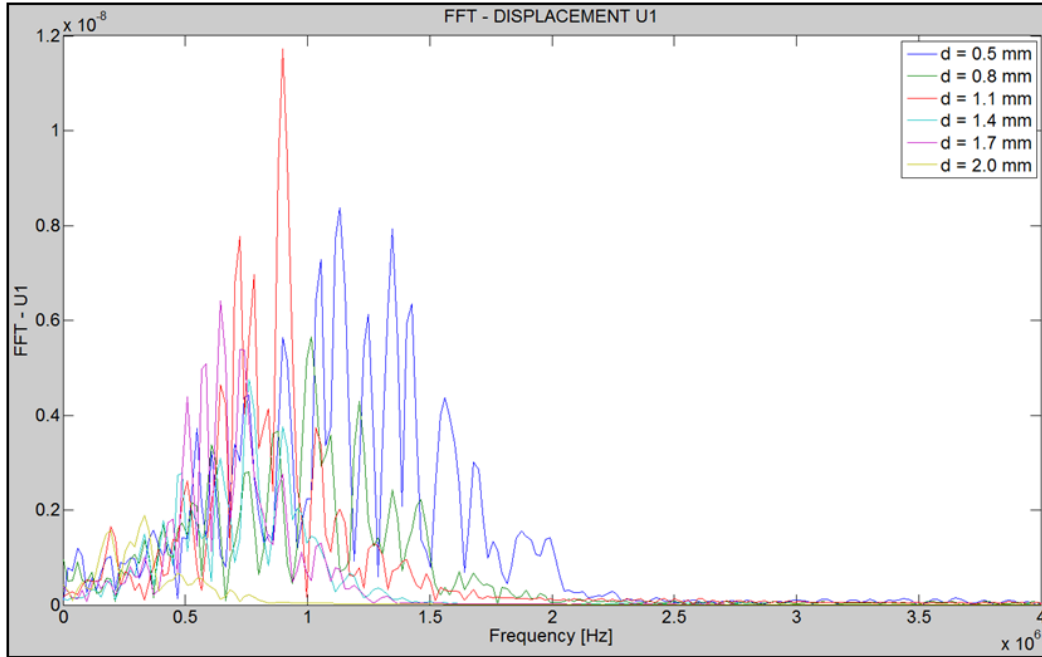
Figure 4.41. Fast Fourier Transform magnitude spectra recorded at the Probe Node for displacement u_x for the six different meshes considered in the convergence study.
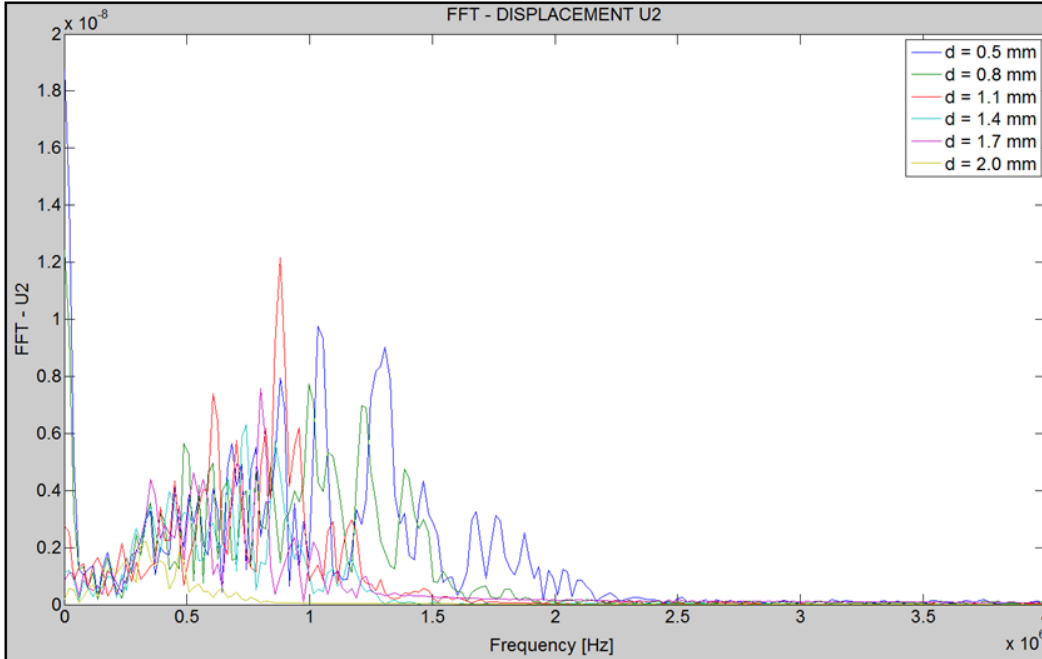
Figure 4.42. Fast Fourier Transform magnitude spectra recorded at the Probe Node for displacement u_y for the six different meshes considered in the convergence study.
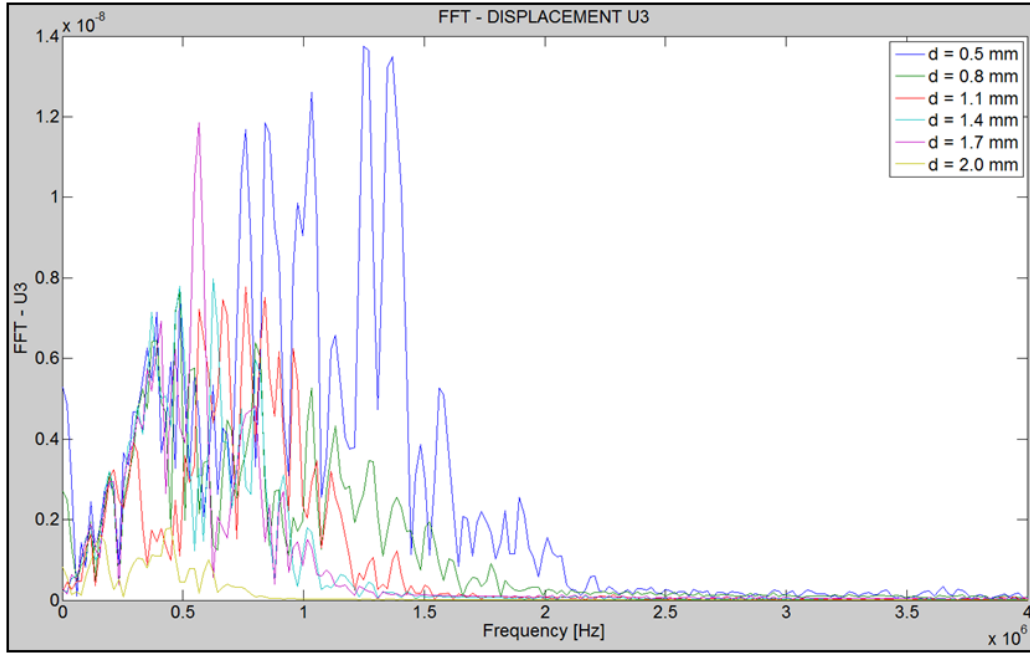
Figure 4.43. Fast Fourier Transform magnitude spectra recorded at the Probe Node for displacement u_z for the six different meshes considered in the convergence study.

For easier reading of the convergence results, a "Convergence Index" was also calculated. This index was computed as the integral of the FFT magnitude spectra between 1 MHz and 2.25 MHz at the Probe Node. The results as a function of mesh refinement are plotted in Figure 4.44 for each of the nine kinematic variables discussed above. These plots clearly show that the Convergence Index improves with increasing mesh refinement, with the $d = 0.5$ mm mesh providing the best convergence results for the high-frequency wave content.
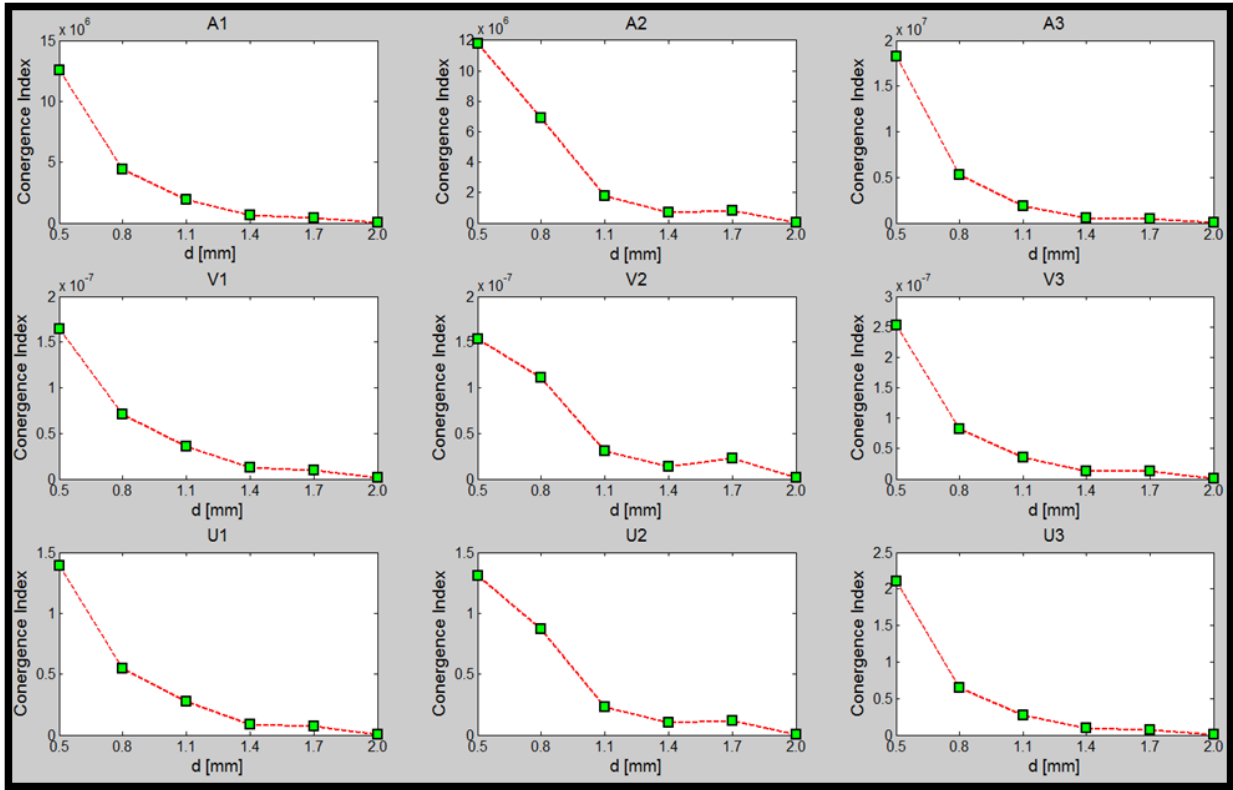
Figure 4.44. Convergence Index for accelerations a_x, a_y and a_z (first row), velocities v_x, v_y and v_z (second row), and displacements u_x, u_y and u_z (third row) recorded at the Probe Node for the six different meshes used in the convergence study.

5. Proposed Ultrasonic Tomographic Method for Rail Flaw Imaging

This chapter discusses the specific steps developed in this project for ultrasonic tomographic imaging of rail flaws.

5.1 Difference between Phased-Array Imaging and Ultrasonic Tomographic Imaging with Synthetic Aperture Focus

It is worth highlighting the differences between Phased Array Imaging and Tomographic-Synthetic Aperture Focus Imaging. A good review of this difference was given by Karaman et al. (1995). In conventional phased array imaging, all transducer elements transmit the ultrasonic waves, and focusing is achieved via wave reflections (Shoup and Hart 1988). This concept is shown in Figure 5.1(a). The improved contrast achieved in phased array imaging comes, however, at the expense of the many parallel transmit and receive circuits that are required. For example, medical imaging phased array 128 channel scanners require 128 independent transmit and receive circuits. Therefore, a phased array system with high channel count (i.e., high defect imaging resolution) can hardly meet the power or size requirements of a handheld system that is practical for field use on the rail tracks.

Alternatively, ultrasonic tomography with Synthetic Aperture Focusing (SAF) represents an evolution from phased array imaging, in that only a few transmitters can be used at once, as shown in Figure 5.1(b). The transmission beam is made as divergent as possible to span the inspection volume; as a result, the active channel count can be dramatically reduced. Ultrasonic tomography with SAF is at the forefront of recent developments in Sonar, Radar, and Medical Imaging. With the SAF approach, focusing is achieved with minimum complexity in both transmit and receive stages. Hence, a SAF-based imaging approach would be ideal for a handheld rail inspection system in the field.

(a)   (b)

Phased-Array (PA) Imaging

All elements transmit with time delays

Tomography with Synthetic Aperture Focus (SAF) Imaging

A few elements transmit with diverging beams
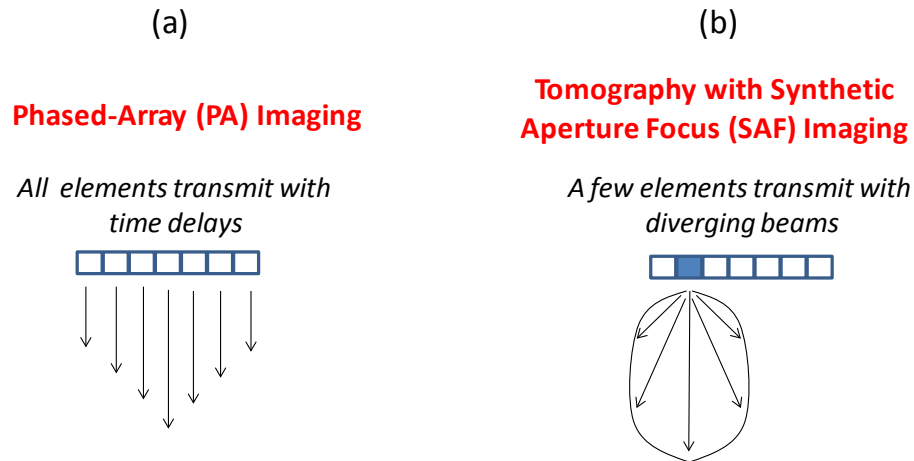
Figure 5.1. (a) Phased-Array Imaging. (b) Tomographic Imaging with Synthetic Aperture Focus.

The following sections describe the particular algorithms used in the SAF tomographic approach that has been developed for the 3-D imaging of rail flaws. The algorithms include the following:

1) Synthetic Aperture Focusing
2) Matched Filtering
3) Baseline Subtraction
4) Multimode Detection

5.2 Synthetic Aperture Focusing

The proposed approach uses SAF implemented with envelope detection and delay-and-sum algorithms. The general idea of the SAF applied in 3-D is schematized in Figure 5.2.
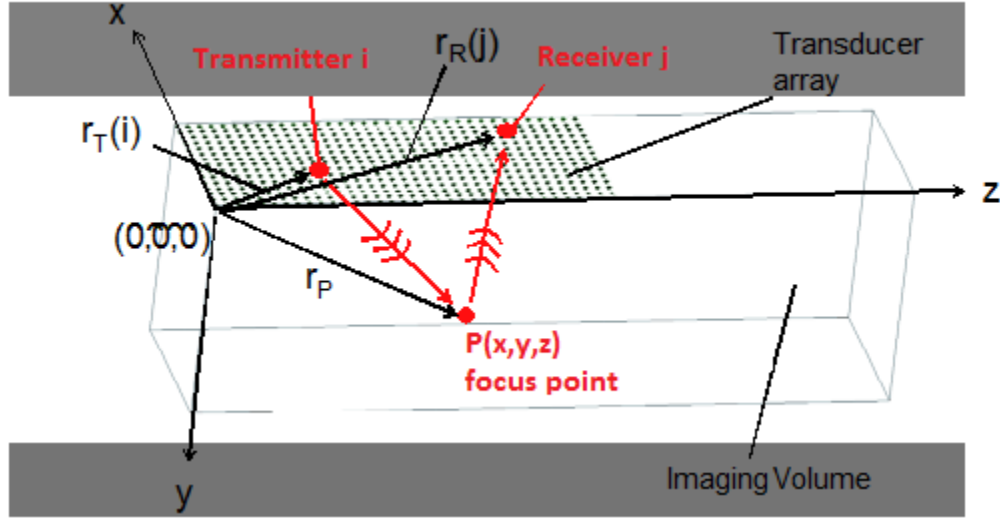
Figure 5.2. Principle of Synthetic Aperture Focusing (SAF) for Ultrasonic Tomography 3-D imaging.

The SAF method is most efficiently implemented using a delay-and-sum algorithm (Nikolov and Jensen 2000 and 2003, Jensen et al. 2006, Daher and Yen 2006). This is based on the time required for an ultrasonic wave to propagate from a transmitter i to a receiver j after reflection from a focus point P in the imaging volume. Referring to Figure 5.2, the delay-and-sum algorithm used in this study can be expressed by the following equation:

$$I(\mathbf{r_P}) = \sum_{j=1}^{N} \sum_{i=1}^{M} y\left[t_P(i,j),i,j\right] \tag{5.1}$$

In the above equation (5.1), $I(\mathbf{r_P})$ is the imaging intensity at focal point $P(x,y,z)$ of the volume (associated with 3-D position vector $\mathbf{r_P}$), N is the total number of receivers j, M is the total number of transmitters i, and the function $y\left[t_P(i,j),i,j\right]$ is the ultrasonic waveform generated by the i-th transmitter and detected by the j-th receiver. The ultrasonic waveform $y\left[t_P(i,j),i,j\right]$ is calculated at the time delay value $t_P(i,j)$, that is in turn calculated from the wave travel time from transmitter i, to the focal point P, to receiver j (Figure 5.2) as follows:

$$t_P(i,j) = \frac{\left|\mathbf{r_P} - \mathbf{r_T}(i)\right|}{v_{L,S}} + \frac{\left|\mathbf{r_P} - \mathbf{r_R}(j)\right|}{v_{L,S}} \tag{5.2}$$

60

In the above equation (5.2), $\mathbf{r}_P$ is the 3-D position vector of the focus point P, $\mathbf{r}_T(i)$ is the 3-D position vector of the i-th transmitter, $\mathbf{r}_R(j)$ is the 3-D position vector of the j-th receiver, and $v_{L,S}$ represents the longitudinal wave velocity or the shear wave velocity in the material. The fact that either the longitudinal wave velocity or the shear wave velocity can be used is referred to as "Multimode Detection" and is further discussed below.

In summary, Equation (5.1) and Equation (5.2) "scan" all focus points $P(x,y,z)$ of the 3-D imaging volume (known as "voxels" in radar and sonar imaging) and attribute to each voxel an "imaging" value $I(x,y,z)$ that corresponds to the ultrasonic intensity that is transmitted by all M transmitters, reflected by point P, and received by all N receivers. This is what is known as "total focusing" (i.e., focusing in both transmit and receive). More importantly, as discussed above, the ultrasonic tomographic approach minimizes the number of transmitters that need to be excited at once, thereby greatly reducing the complexity of the electronics.

Owing to the focusing process in both transmit and receive, the Signal-to-Noise Ratio (SNR) of the image expected from an ultrasonic tomographic system with M transmitters and N receivers can be written as (Lockwood et al. 1998):

$$SNR = \sqrt{N \times M} \tag{5.3}$$

Therefore, as expected, the SNR of the resulting image improves with increasing numbers of transmitters and receivers. In practice, the hardware complexity, cost, and scan time limit the number of transducers that can be used—with much more restrictive limits on the number of transmitters. That is why, in this study, a *sparse* array of transmitters was used (as few as five transmitters for the 3-D rail imaging) in combination with a finer array of receivers (140 or 525 receivers for the 3-D rail imaging). The same approach involving sparse transmitters and fine receivers has been considered in medical imaging devices based on the SAF technique (Lockwood et al. 1998).

The present study applies envelope detection (Frazier and O'Brien 1998) to the waveforms $y[t_P(i,j),i,j]$ before applying the delay-and-sum equations (5.1) and (5.2), as is customary in ultrasonic imaging. In the Matlab$^©$ program that has been written, envelope detection was

61

achieved by taking the absolute value of the waveforms' Hilbert Transform. For the purposes of analysis, the Hilbert Transform $\hat{y}(t)$ of a signal $y(t)$ is expressed with the following equation:

$$\hat{y}(t) = \frac{1}{\pi} \int_{-\infty}^{+\infty} \frac{y(t)}{t - \tau} d\tau \tag{5.4}$$

Figure 5.3 shows the application of envelope detection to one of the ultrasonic signals recorded in the rail by the 3-D imaging system discussed later in this report. It is clear that the Hilbert Transform effectively captures the signal strength (amplitude) which is then summed, with the appropriate delays, at each point of the imaging volume.
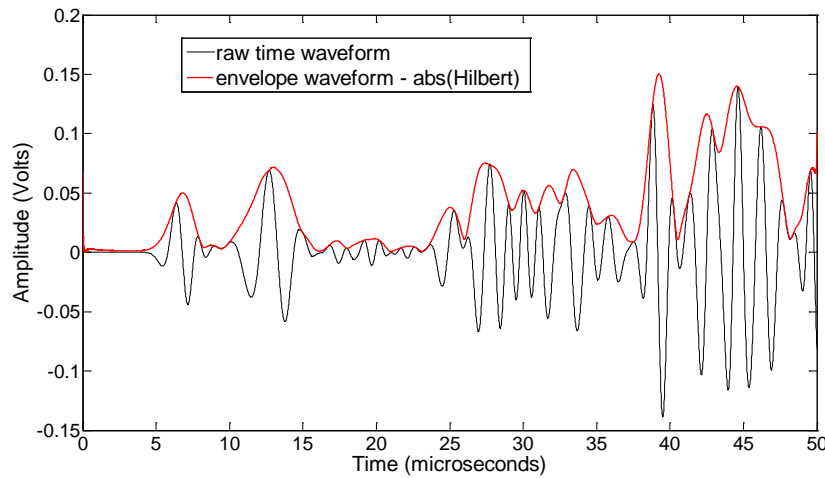
Figure 5.3. Example of envelope detection (Hilbert Transform) of an ultrasonic waveform recorded from the 3-D rail imaging FEA model.

5.3 Matched Filtering

One key step that was adopted in the present study involved the implementation of matched filtering in the general SAF approach. The matched filtering step is used in radar imaging (Maitre 2008) to compress and denoise the radar pulses, thereby dramatically enhancing the SNR and image resolution.

The matched filtering approach implemented for rail imaging performs a cross-correlation between each raw waveform detected by the ultrasonic receivers and the known excitation sent to the ultrasonic transmitters. For the purposes of analysis, the matched filtered signal is represented by the following equation:

$$z(t) = \int_{-\infty}^{+\infty} f^*(\tau)\, y(t+\tau)\, d\tau \tag{5.5}$$

where $f^*(\tau)$ is the complex conjugate of the (known) excitation signal sent to the transmitters and $y(t)$ is the waveform detected by the receivers.

Figure 5.4 shows an example of the application of matched filtering. The top waveform represents the excitation signal, which is a two-cycle toneburst at 2 MHz (this is the same excitation used for the 3-D rail flaw imaging model discussed earlier). The middle waveform represents a simulated detection with 10 dB white noise added. The bottom signal was obtained by match filtering the noisy signal with the excitation signal. As shown in the figure below, the arrival of the waveform is clearly visible in the filtered result. This filtering was one of the keys to success for the 3-D rail flaw imaging results shown later.
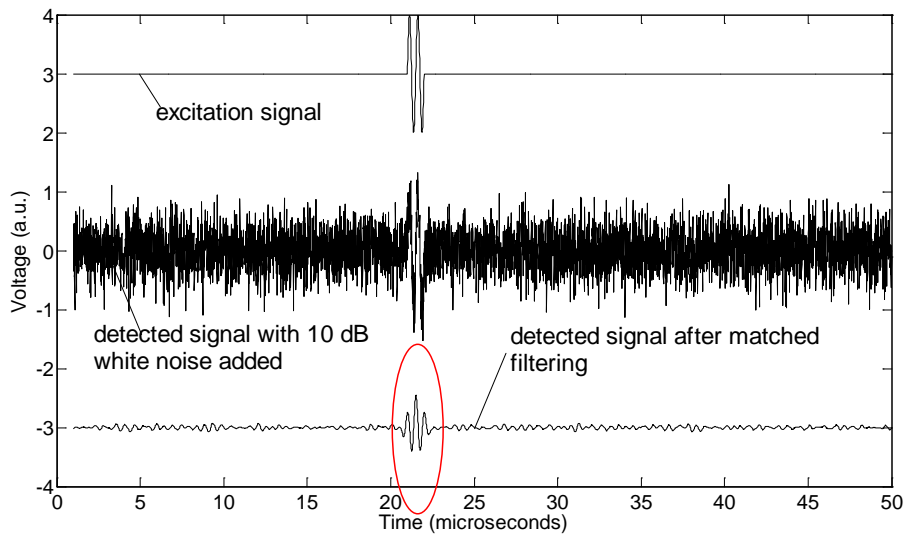
Figure 5.4. Example of Matched Filtering. Top waveform: excitation signal (two-cycle toneburst at 2 MHz). Middle waveform: detected signal with 10 dB white noise added ("noisy signal"). Bottom signal: "noisy signal" after matched filtering with excitation signal.

In radar imaging, the matched filtering is more often achieved using a chirped signal, rather than the narrowband signal used in Figure 5.4. The chirped signal provides an added pulse compression performance that can further increase the resolution of the tomographic image. The

use of chirped excitation could be considered in the future for the rail flaw imaging prototype, if signal noise becomes an issue.

5.4 Baseline Subtraction

Another key feature implemented in the 3-D rail flaw imaging approach is baseline subtraction. This step was derived by subtracting the ultrasonic results of a defect-free rail (baseline) from the results of the flawed rail. This step eliminates any wave contributions that have not resulted directly from the flaw (primarily railhead boundaries), and dramatically enhances the SNR of the defect image. In actual rail imaging in the field, this step simply requires taking a scan of a pristine region of the rail prior to scanning the flawed region. In theory, it should be sufficient to take only one baseline scan for each geometry of rail (136 lb, 139 lb, etc.) being inspected. When imaging defects in a worn rail, the baseline would be taken on the specific rail section to be inspected to account for the worn profile.

In the Matlab$^{©}$ program developed, baseline subtraction was implemented in two different modalities. In the first modality (envelope subtraction), the subtraction was performed on the enveloped signals. In the second modality (image subtraction), the subtraction was performed on the resulting images. Both approaches yielded successful results.
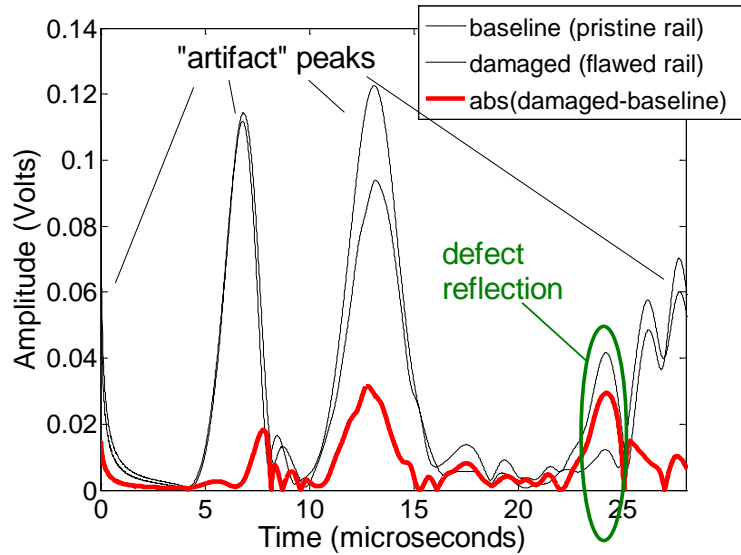
Figure 5.5. Example of baseline subtraction on the envelope signals. Notice how the defect reflection increases relative to the "artifact" peaks in the baseline-subtracted signal (red trace).

Figure 5.5 shows an example of envelope baseline subtraction on one of the signals from the 3-D rail flaw imaging simulation discussed in Section 4. This graph depicts an envelope signal from the damaged rail, the envelope signal from the pristine rail (baseline), and the baseline-compensated signal (red trace). As seen, the baseline subtraction increases the defect reflection (arriving at approximately 24 microseconds in this case), while decreasing the signal peaks, which are artifacts and not related to the flaw, on either side of the defect reflection. In comparison, the "artifact" peaks are larger than the defect reflection in the raw "damaged" signal before baseline subtraction (black continuous line).

5.5 Multimode Detection

Yet another step implemented in the imaging algorithm is the multimode detection. This unique possibility exists in rail flaw imaging because the rail steel allows for the two fundamental wave modes of propagation: longitudinal wave mode and shear wave mode. These two modes propagate at two different velocities (typical velocities for steel are longitudinal velocity $v_L = 5.3$ mm/microsec and shear velocity $v_S = 2.8$ mm/microsec). Under longitudinal mode excitation, the rail flaw reflects both the same longitudinal mode (same mode reflection) and the shear mode (mode conversion). The existence of the two different modes allows for the use of different time

delays in the delay-and-sum equations (5.1) and (5.2), thereby providing redundant focusing for enhanced SNR of the imaging result.

The existence of both the longitudinal wave mode (travelling faster) and the shear wave mode (travelling slower) in a flawed rail is shown in Figure 5.6. This figure depicts the propagating wave fronts (Von Mises stress) from the 2-D FEA study that is discussed in detail in Section 3.

It should be emphasized that the option to exploit both wave modes for imaging is unique to ultrasonic propagation in solid materials (i.e., materials with a non-negligible elastic shear stiffness); this option was selected for the present study of rail flaw detection because no shear wave mode exists in fluids or biological media (i.e., underwater sonar and medical imaging can only exploit the ultrasonic longitudinal mode) and no shear mode exists in electromagnetic RF waves (i.e., radar imaging can only exploit one RF wave mode).
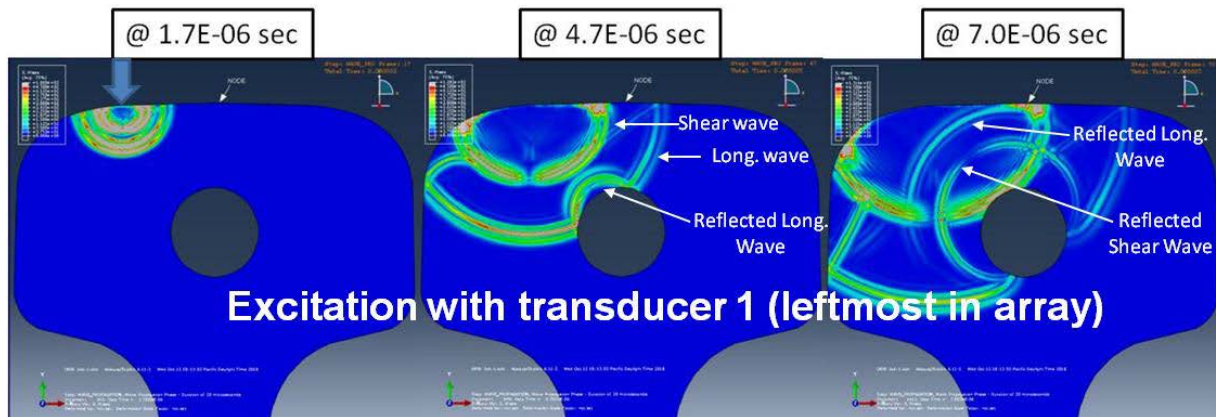
Figure 5.6. Multimode Detection: formation of both longitudinal wave mode (travelling faster) and shear wave mode (travelling slower) in rail flaw imaging (from the 2-D FEA model discussed in the next section).

6. 2-D Rail Flaw Imaging

This chapter presents the results of the ultrasonic tomographic imaging of the 5-percent RHA TD in the 136-pound RE rail from the 2-D simulations.

6.1 Finite Element Model for 2-D Rail Flaw Imaging

The FEA model for 2-D rail flaw imaging consisted of a 136-pound rail with a TD in the railhead extending for 5 percent of the rail RHA, as shown in Figure 6.1. ABAQUS Explicit was used for the model. The FE mesh was generated for a maximum ultrasonic frequency of 2.25 MHz and 10 elements per wavelength as required to properly represent the ultrasonic waves. The resulting FE parameters were as follows:

- Total number of nodes: 188,256
- Total number of elements: 187,112
- Element type: linear quadrilateral elements of type CPS4R

Figure 6.1. The FE mesh for the 2-D rail flaw imaging study along with the linear transducer array for tomographic imaging with Synthetic Aperture Focus.

For 2-D imaging (plane strain), a linear transducer array with N = 23 elements and 1.5 mm spacing was simulated in the model. The array was used for SAF in a reflection mode where each of the transducers acted as a transmitter of a 2.25 MHz wave and all the remaining

transducers acted as the receivers of the wave. The total number of transmitter-receiver combinations was therefore $N^2 = 529$ combinations. In addition to the flawed rail model, a pristine rail model was analyzed for baseline subtraction.

The transducer signals were analyzed in Matlab[©] to perform the tomographic imaging steps that were described in the previous section. Specifically, the following steps were conducted for the 2-D imaging:

- Synthetic Aperture Focus (see Section 5.2)
- Baseline Subtraction (see Section 5.4)
- Multimode Detection (see Section 5.5)

The matched filtering step was not implemented in the 2-D imaging, only in the 3-D imaging. In addition, noise robustness studies were performed in 2-D by adding artificial noise.

Figure 6.2 shows a detail of the mesh around the 5-percent RHA TD to demonstrate the high level of refinement used.
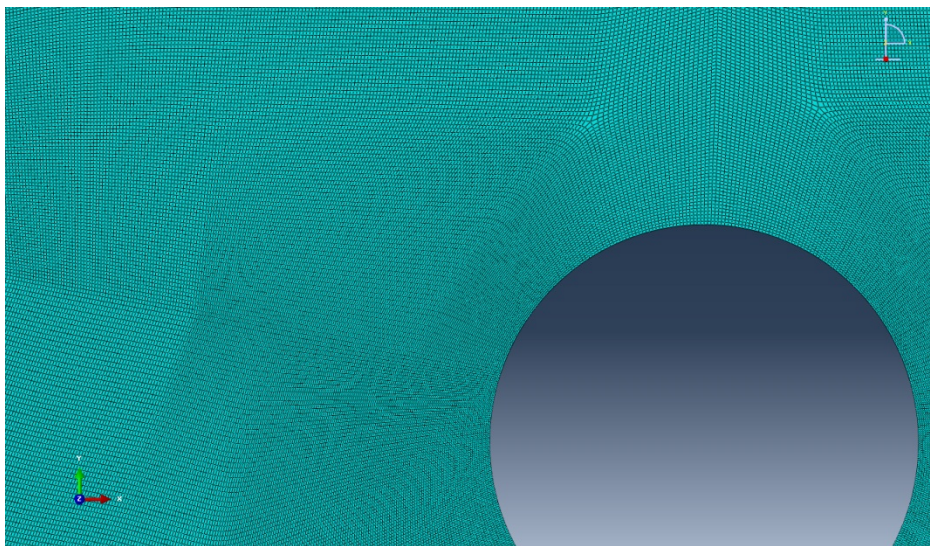
Figure 6.2. Detail of the FE mesh around the 5% RHA Transverse Defect.

Figure 6.3 shows an example of wave propagation generated in this model. The cases shown are those of wave generation with the leftmost transducer in the array (transducer 1) and wave generation with the central transducer in the array (transducer 12). The excitation signal in all cases was a one-cycle sine wave at 2.25 MHz frequency directed vertically. The figure shows, in

terms of Von Mises stress, that both longitudinal wave modes (travelling faster) and shear wave modes (travelling slower) are generated by the excitations, and both modes are generated at the reflections from the defect, which confirms the "same-mode reflection" and "mode-converted reflection" expected for this kind of wave-defect interaction.

The existence of both longitudinal mode and shear mode allowed us to exploit multimode detection for enhanced imaging performance. The following values of longitudinal wave velocity and shear wave velocity were used in the time delays used for the delay-and-sum algorithm (Equations 5.1 and 5.2):

Longitudinal Wave speed: $v_L = 5.3$ mm/microsec

Shear Wave speed: $v_S = 2.8$ mm/microsec

These velocity values were measured from the FEA animations.
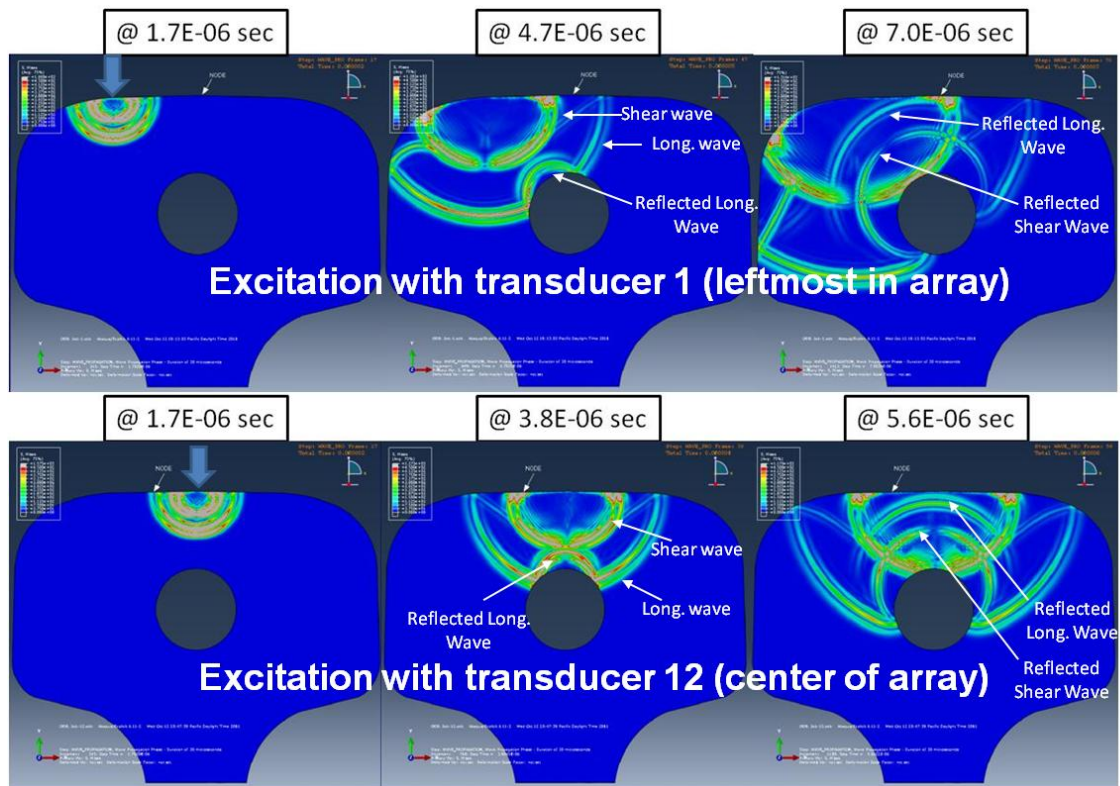
Figure 6.3. Von Mises stress contour plots for two different excitations showing the propagation of both longitudinal wave mode (travelling faster) and shear wave mode (travelling slower).

6.2 Imaging Results from the 2-D Model

Representative results of the 2-D defect imaging with the Matlab$^{©}$ ultrasonic tomographic algorithm are presented in this section. Figure 6.3 shows the result for two cases. The left-hand plot is the imaging result obtained using the longitudinal modes and the envelope baseline subtraction. The right-hand plot is the imaging result obtained using the longitudinal mode and the shear mode (Multimode Detection), as well as image baseline subtraction. In both images, the top of the 5 percent RHA defect is clearly visible in the correct position. A small "shadow" artifact is present in the longitudinal-shear image. The fact that only a portion of the defect contour was successfully imaged has to do with the limited width of the array considered. These results therefore serve as a successful proof-of-principle 2-D imaging.

Longitudinal Wave Transmission and Longitudinal Wave Reflection

Longitudinal Wave Transmission and Shear Wave Reflection
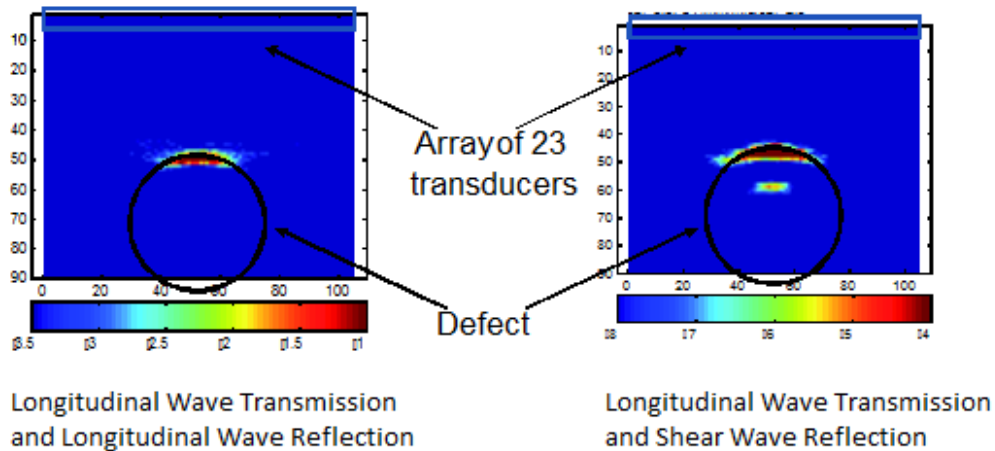
Figure 6.4. 2-D Imaging of 5% RHA Transverse Defect by Ultrasonic Tomography with Synthetic Aperture Focus using (a) the Longitudinal Wave mode (left-hand image) and (b) the Longitudinal Wave mode and the Shear Wave mode (right-hand image). Baseline Subtraction was also implemented in these images.

6.3 Noise Robustness Study

In an effort to test the robustness of the ultrasonic tomographic imaging method, noise was artificially added to the FEA waveforms prior to use of the SAF algorithm. Specifically, Gaussian white noise was added using the Matlab$^{©}$ function "awgn" at increasing power levels (relative to the original signals) from 10 dB to 35 dB in 5 dB increments.

70

Figures 6.5 through 6.7 show the imaging results corresponding to the same two cases shown earlier in Figure 6.4, but with the signals corrupted by the increasing levels of Gaussian noise. These figures show representative signals (after envelope detection) without noise (red traces) and with noise added (blue traces). The results shown in Figures 6.5 through 6.7 lead to the following conclusions:

- Noise levels up to 35 dB in power over the original signals do not degrade substantially the images created by the longitudinal and shear wave combination.
- Noise levels up to 25 dB in power over the original signals do not degrade substantially the images created by the longitudinal and shear wave combination. However, above the 25 dB noise level, longitudinal and shear wave combination images are substantially degraded.

Overall, the results suggest a strong robustness against noise, and particularly so when multimode detection is implemented in the tomographic imaging algorithm, in addition to baseline subtraction. Clearly, these results are also limited by the ultrasonic frequency used in excitation (2.25 MHz). The use of a higher frequency (which is challenging to model in FEA, but easy to implement experimentally in a prototype) would enhance the resolution of the defect images shown here.
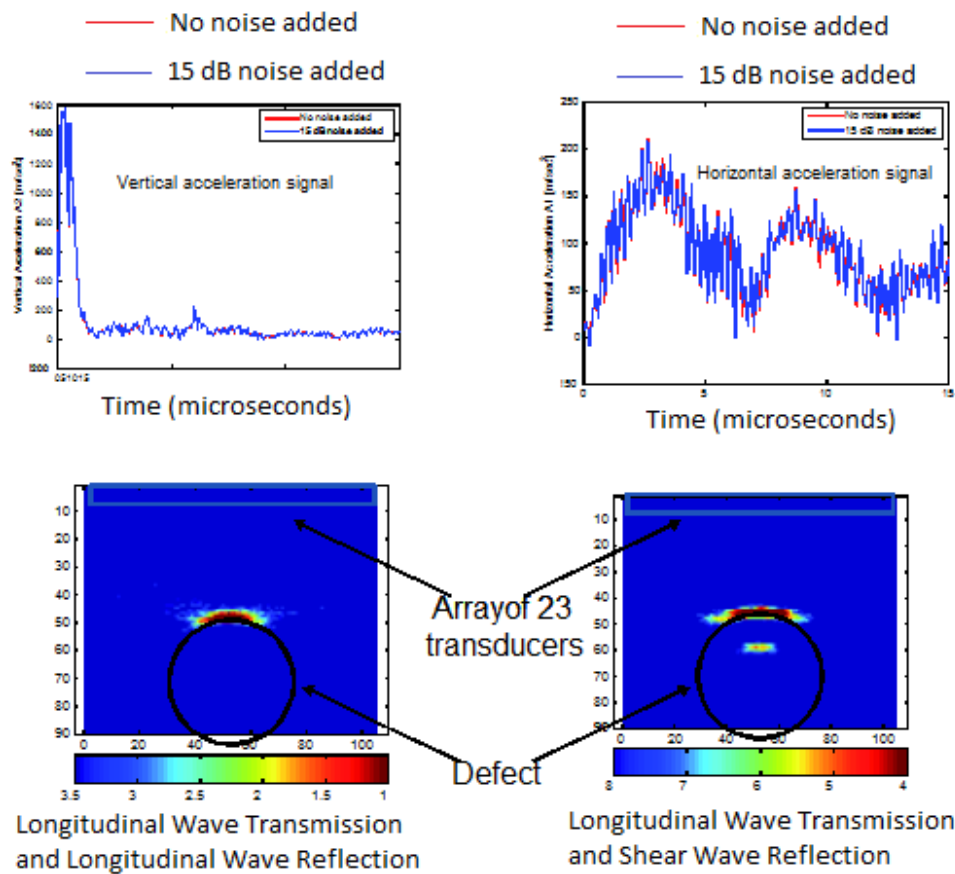
Figure 6.5. 2-D Imaging of 5% RHA Transverse Defect with 15 dB Gaussian White Noise added to the signals, and using (a) the Longitudinal Wave mode (left-hand image) and (b) the Longitudinal Wave mode and the Shear Wave mode (right-hand image). Baseline Subtraction was also implemented in these images.
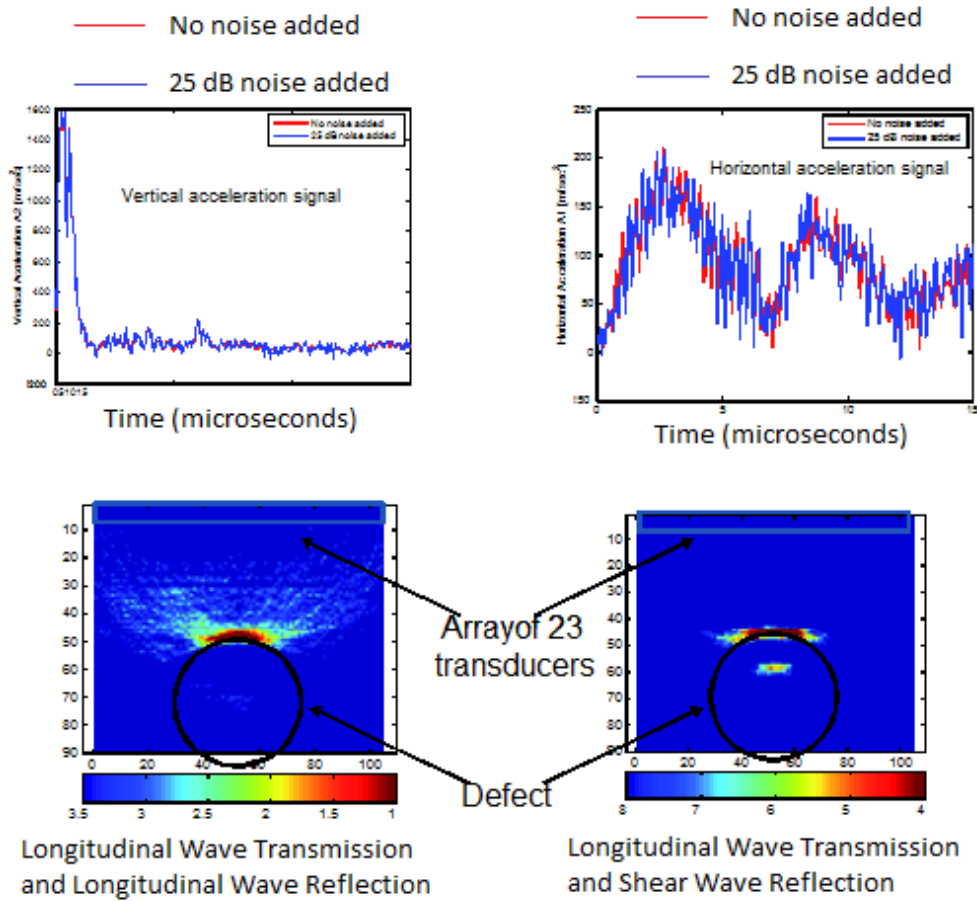
Figure 6.6. 2-D Imaging of 5% RHA Transverse Defect with 25 dB Gaussian White Noise added to the signals, and using (a) the Longitudinal Wave mode (left-hand image) and (b) the Longitudinal Wave mode and the Shear Wave mode (right-hand image). Baseline Subtraction was also implemented in these images.
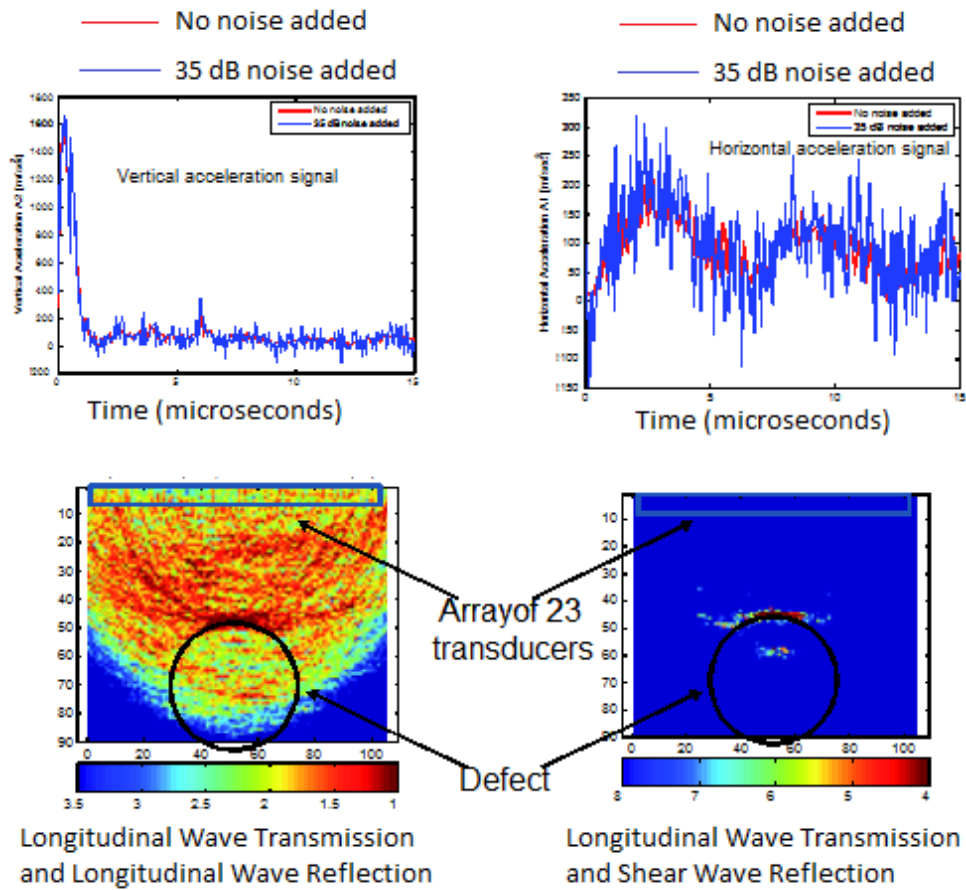
Figure 6.7. 2-D Imaging of 5% RHA Transverse Defect with 35 dB Gaussian White Noise added to the signals, and using (a) the Longitudinal Wave mode (left-hand image) and (b) the Longitudinal Wave mode and the Shear Wave mode (right-hand image). Baseline Subtraction was also implemented in these images.
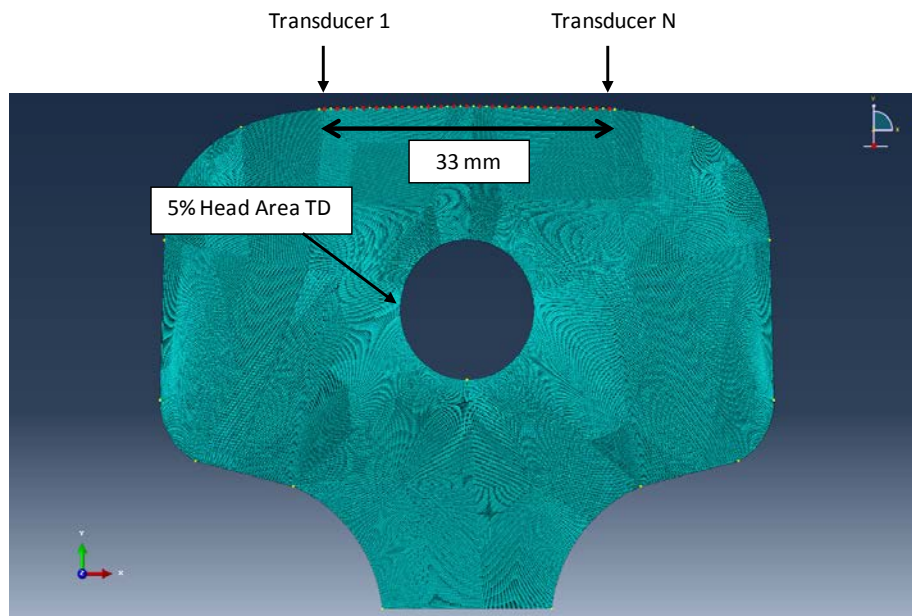
7. 3-D Rail Flaw Imaging

This chapter presents the results of the ultrasonic tomographic imaging of the 5-percent RHA TD in the 136-pound RE rail from the 3-D simulations.

7.1 Finite Element Model for 3-D Rail Flaw Imaging

The 3-D FEA ABAQUS model consisted of a 175.2-milimeter long section of a 136-pound RE rail sectioned at the web height as shown in Figure 7.1. The flaw modeled was a circular TD extending for 5 percent of the rail RHA as shown in the sectional view of Figure 7.2.
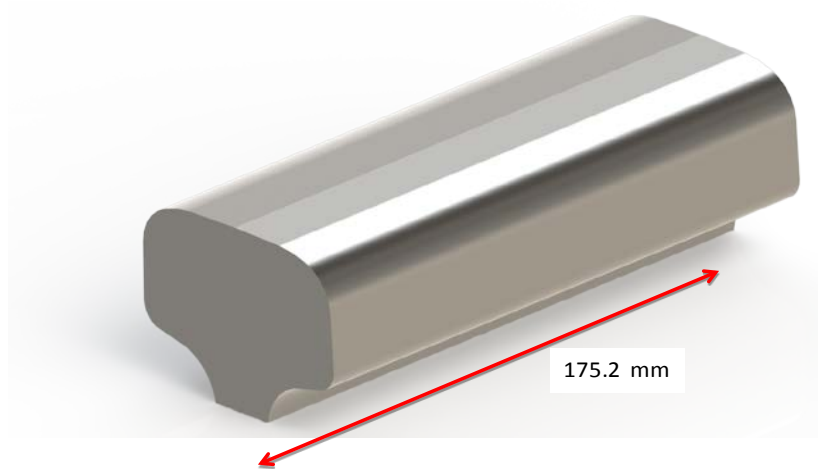
Figure 7.1. Rail section model for the 3-D FEA.
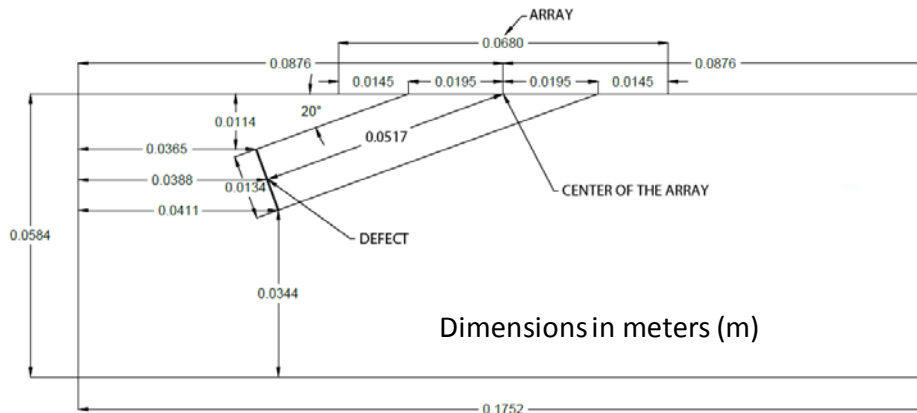
Figure 7.2. Geometrical dimensions for the 3-D FEA model.

The FE mesh used 8-node linear hexahedral elements with "reduced integration" (ABAQUS element HEXA C3D8R) and a characteristic size of 0.5 mm. Another important feature was the use of 8-node "infinite elements" (ABAQUS element HEXA CIN3D8) at the boundaries of the model to avoid spurious reflections of the ultrasonic waves that would not be existent in an actual inspection in the field. The resulting mesh is shown in Figures 7.3 and 7.4.

The resulting FE parameters were as follows:

- Total number of nodes: 3,948,855
- Total number of elements: 4,023,918
- Element type on model: linear hexahedral elements of type HEXA C3D8R
- Element type on boundaries: "infinite" elements of type HEXA CIN3D8
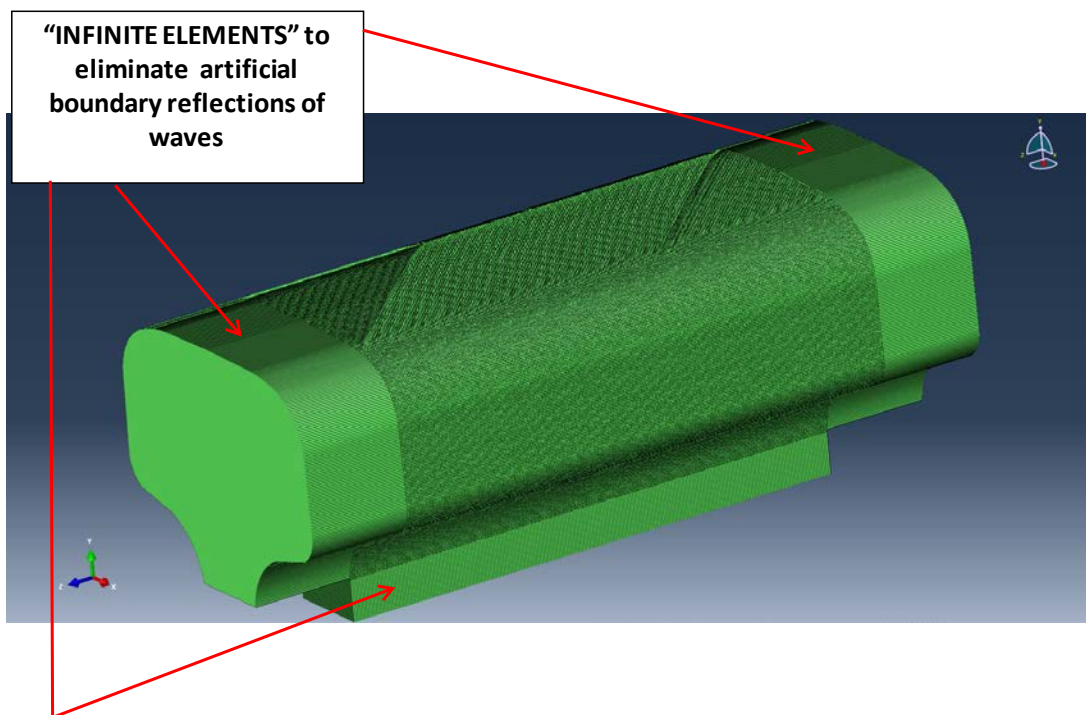
Figure 7.3. Mesh for the 3-D FEA with "infinite elements" at the model boundaries to eliminate artificial boundary reflections of the waves.

5% H.A. Transverse Defect
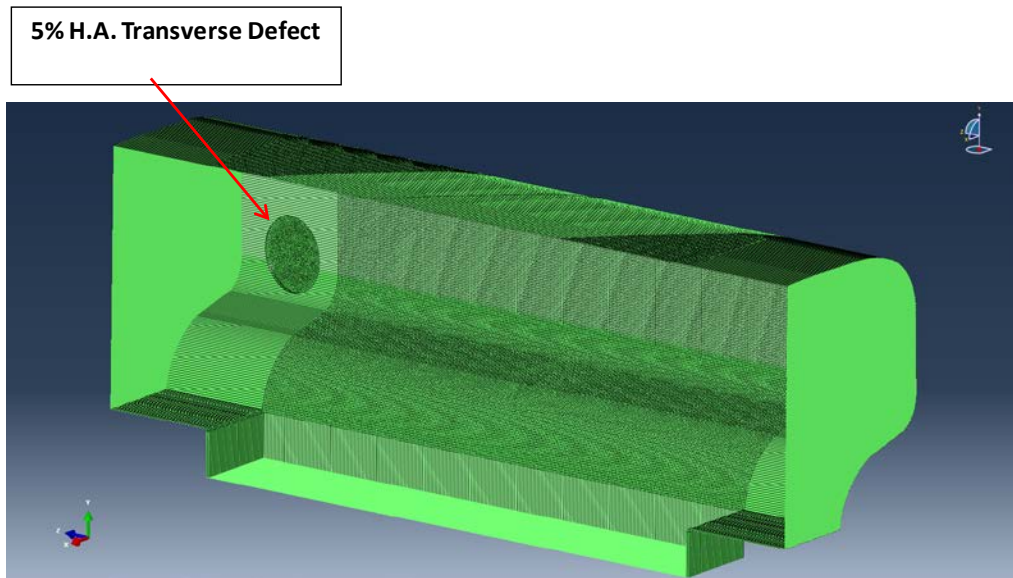
Figure 7.4. Mesh for the 3-D FEA: sectional view.

For 3-D imaging, a planar transducer array with a total of 525 elements and 2 mm spacing was simulated in the model. The array was used for SAF in a reflection mode. Different views of the transducer array simulated in the FEA model are provided in Figures 7.5 and 7.6.

To simplify the procedure, and also with a future prototype design in mind, it was decided that a scheme with *sparse* transmitters, i.e. only five transmitters ($M = 5$), would be used (Figure 7.7). As discussed earlier in the report, minimizing the number of transmitters is an effective way to decrease the complexity, cost, and scan time of an imaging system. For the reception, the following two cases were considered: all elements receiving (Full Array: $N = 525$), and only 140 elements receiving (Reduced Array: $N = 140$). The total transducer combinations used in the 3-D SAF algorithm was therefore:

- Full Array: $N \times M = 525 \times 5 = 2,625$
- Reduced Array: $N \times M = 140 \times 5 = 700$.

The excitation signal to the five transmitters was a force inclined at 70 degrees from the vertical and following a one-cycle toneburst at 2 MHz. The 70-degree orientation is consistent with the 70-degree wedge angle used in conventional ultrasonic hand verification of Transverse Head defects in the rail head.
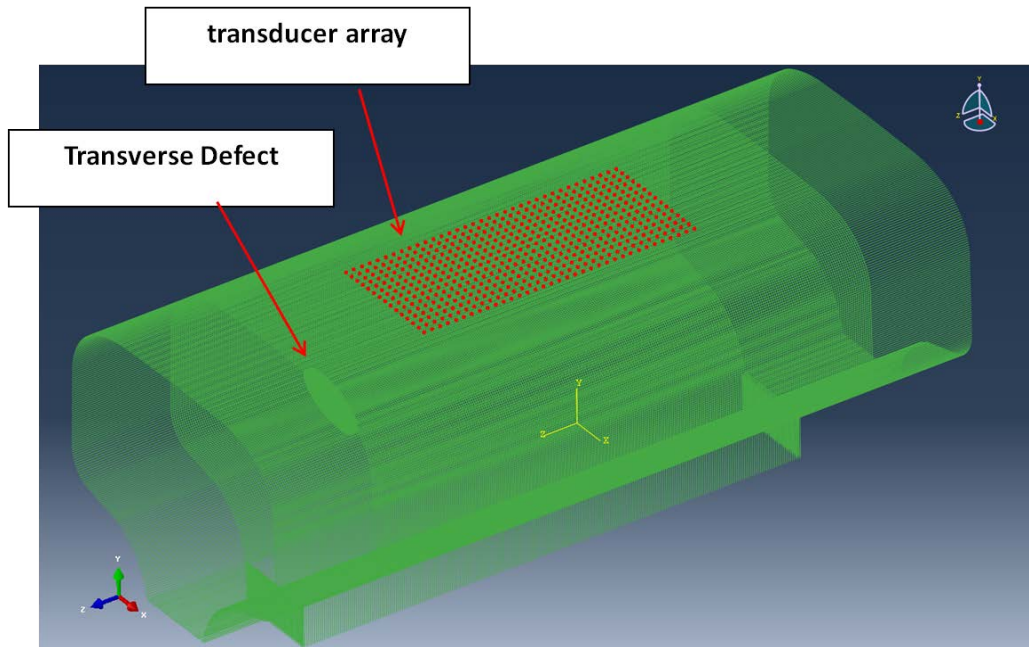
Figure 7.5. Full transducer array for the 3-D FEA.
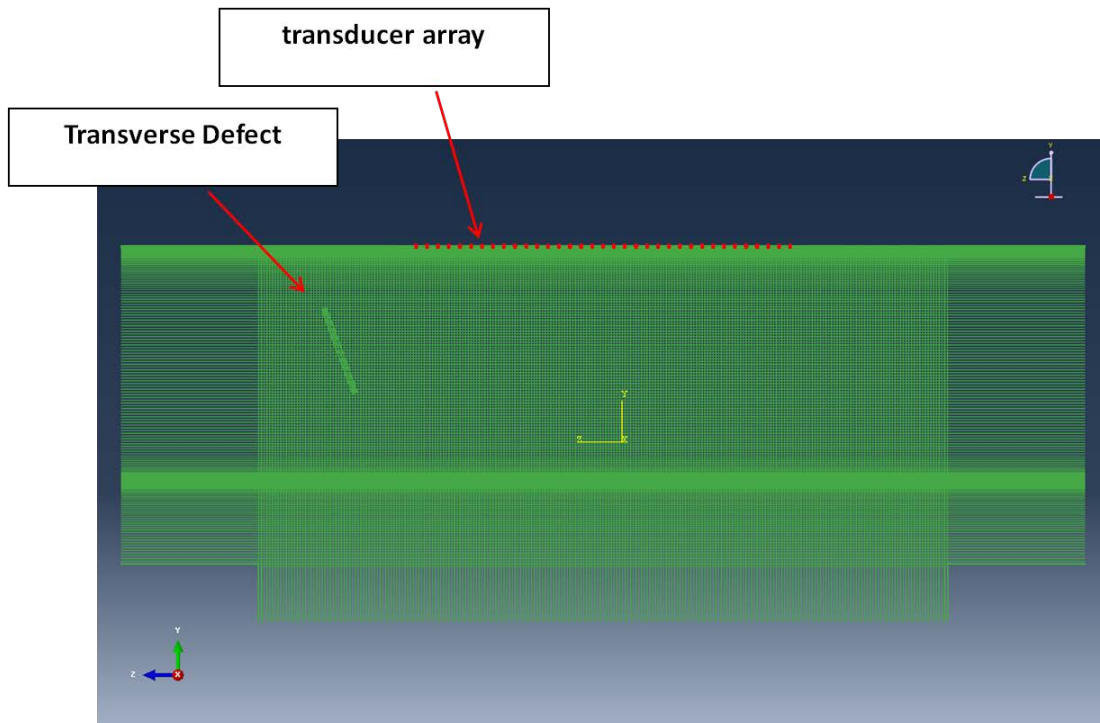
Figure 7.6. Full transducer array for the 3-D FEA: sectional view.
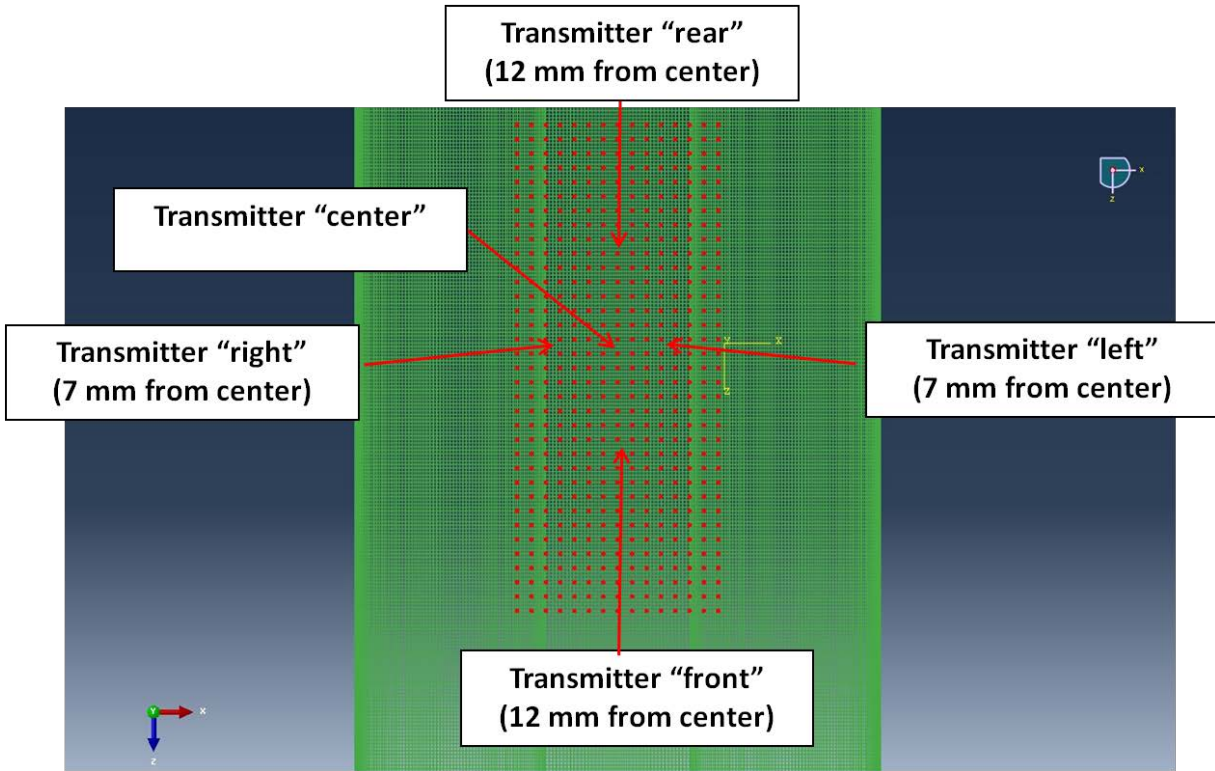
Figure 7.7. Position of the five "sparse" transmitters in the transducer array: top view.

For the 3-D imaging case, a pristine rail model was analyzed along with the flawed rail model for baseline subtraction. In addition, the matched filtering step was adopted by cross-correlating the received signals with the known excitation signal. In summary, the tomographic imaging Matlab[©] program for the 3-D case included all of the necessary imaging steps discussed earlier:

- Synthetic Aperture Focus (see Section 7.2)

- Matched Filtering (see Section 7.3)

- Baseline Subtraction (see Section 7.4)

- Multimode Detection (see Section 7.5)

As was the case with the 2-D FEA results, the existence of both longitudinal mode and shear mode in the 3-D case allowed multimode detection to be used for enhanced imaging performance. The following values of longitudinal wave velocity and shear wave velocity were used in the delay-and-sum algorithm of the 3-D analysis:

Longitudinal Wave speed: v_L = 5.9 mm/microsec

Shear Wave speed: v_S = 3.1 mm/microsec

These velocity values were measured from the 3-D FEA animations.

Screenshots of the wave propagation in the 3-D model, under excitation by the central transmitter, are shown in Figures 7.8 and 7.9 in terms of Von Mises stress.
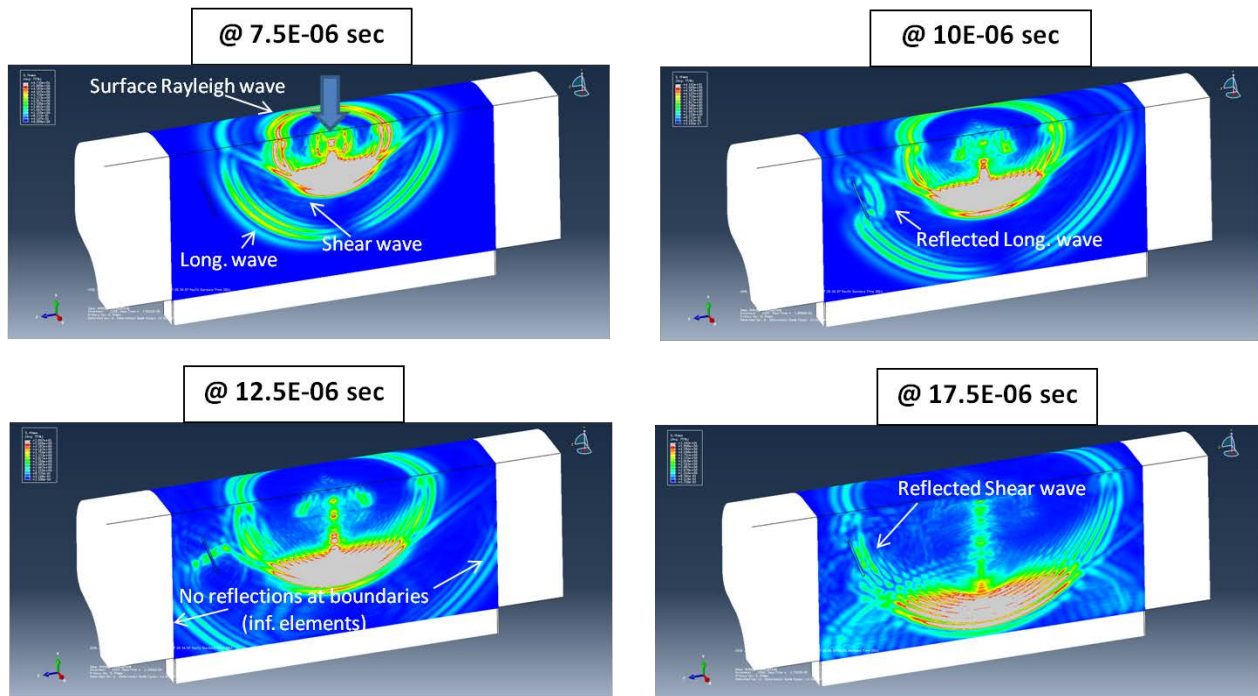
Figure 7.8. Von Mises stress contour plots for central excitation showing the propagation of both Longitudinal Wave mode (travelling faster) and Shear Wave mode (travelling slower), as well as absence of reflections at boundaries owing to "infinite" elements (longitudinal sectional view).
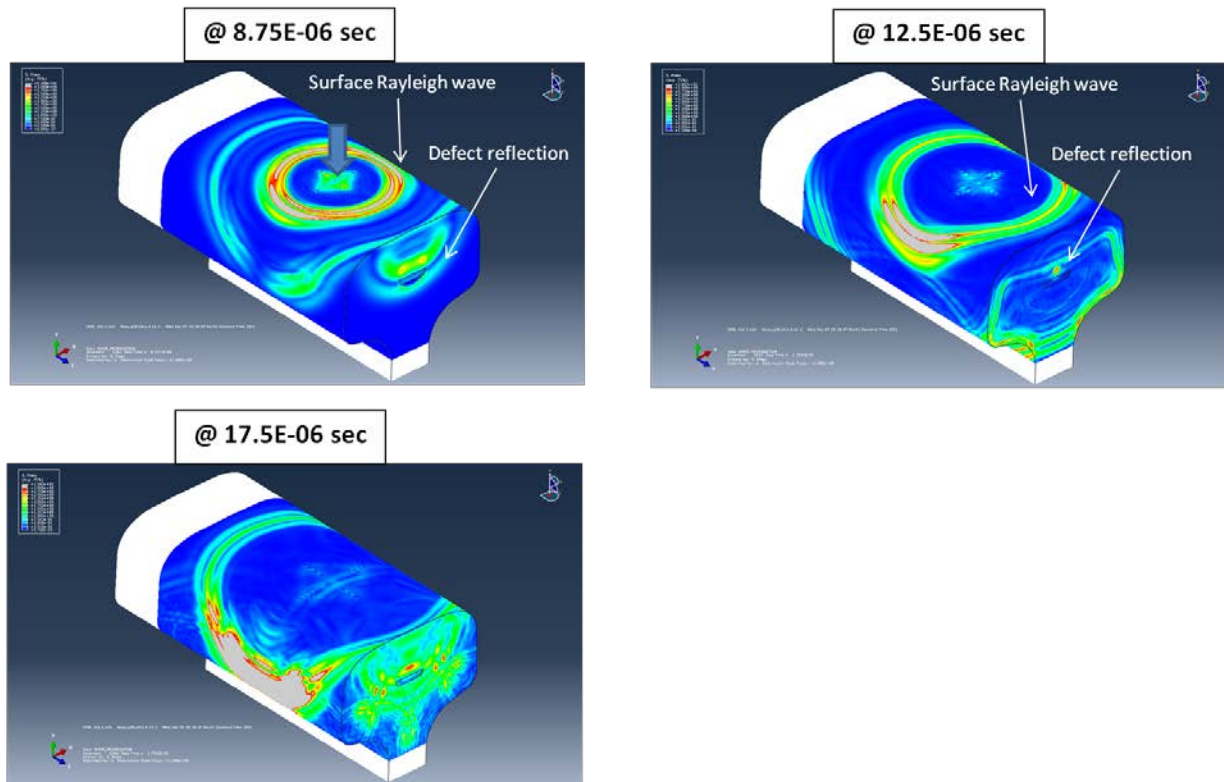
Figure 7.9. Von Mises stress contour plots for central excitation (transverse sectional view at defect position).

7.2 Imaging Results from the 3-D Model

7.2.1 Results from the Full Array (5 transmitters, 525 receivers)

Representative 3-D imaging results from the ultrasonic tomographic algorithm with the full receiver array are shown in this section.

Figures 7.10 through 7.16 show different views of the imaging result obtained using the longitudinal mode and the shear mode (multimode detection: L-wave velocity for transmitter-to-defect path and S-wave velocity for defect-to-receiver path) using matched filtering and envelope baseline subtraction. The defect indication is clearly shown with excellent contrast, with no extraneous artifacts, image noise, or uncorrelated speckle noise. The defect imaged with this L-mode and S-mode combination (L-mode/S-mode) appears in a position that is slightly underestimated horizontally (direction z in the figures), and slightly overestimated vertically (direction y in the figures). A more precise location will likely require a change in the value of the shear wave velocity adopted for the SAF algorithm. The overall shape of the defect and,

more importantly, the *size* of the defect (which is the most important parameter for decisionmaking for an in-service rail inspection) are estimated very accurately. In fact, with an actual defect size of 141 mm^2 (or 5 percent rail RHA), the L-wave and S-wave tomographic imaging yields a defect size of 150 mm^2 (or 5.3 percent rail RHA). In summary:

Full array (5 transmitters, 525 receivers)

- Actual defect size: 5 percent rail RHA
- Defect size calculated from L-wave/S-wave Tomographic Imaging: 5.3 percent rail RHA
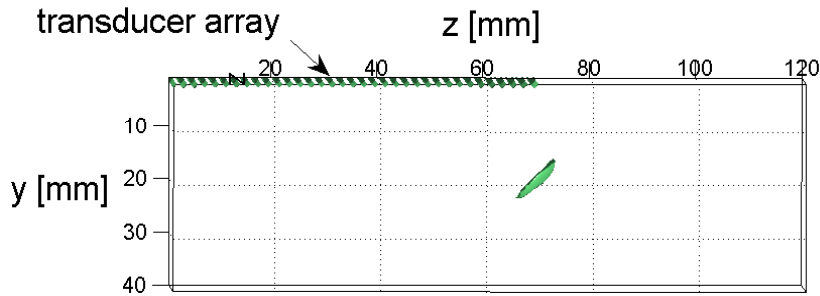
Figure 7.10. 3-D Imaging of 5% RHA Transverse Defect using the Longitudinal Wave mode and the Shear Wave mode with Envelope Baseline Subtraction (Full Array: 5 transmitters, 525 receivers).
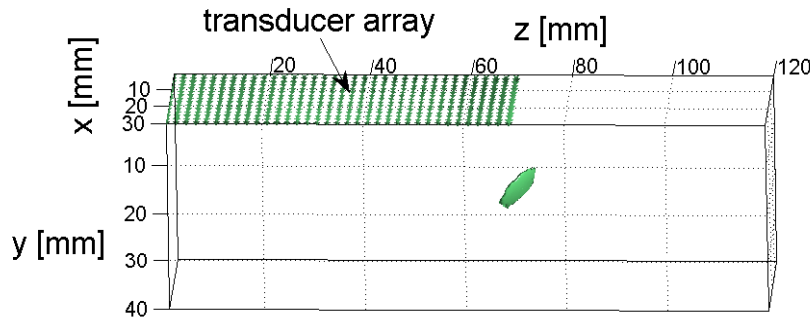
Figure 7.11. 3-D Imaging of 5% RHA Transverse Defect using the Longitudinal Wave mode and the Shear Wave mode with Envelope Baseline Subtraction (Full Array: 5 transmitters, 525 receivers).

Longitudinal-Shear (Damaged - Pristine Signal Envelope Difference)
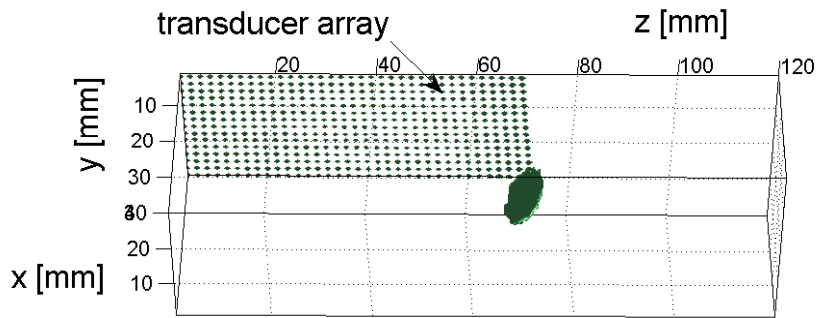
Figure 7.12. 3-D Imaging of 5% RHA Transverse Defect using the Longitudinal Wave mode and the Shear Wave mode with Envelope Baseline Subtraction (Full Array: 5 transmitters, 525 receivers).

Longitudinal-Shear (Damaged - Pristine Signal Envelope Difference)
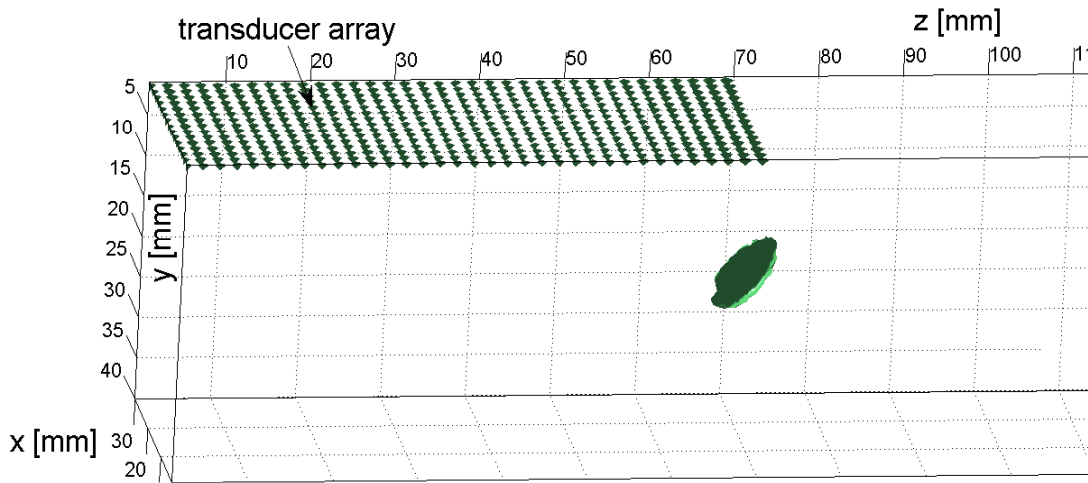
Figure 7.13. 3-D Imaging of 5% RHA Transverse Defect using the Longitudinal Wave mode and the Shear Wave mode with Envelope Baseline Subtraction (Full Array: 5 transmitters, 525 receivers).

83

Longitudinal-Shear (Damaged - Pristine Signal Envelope Difference)
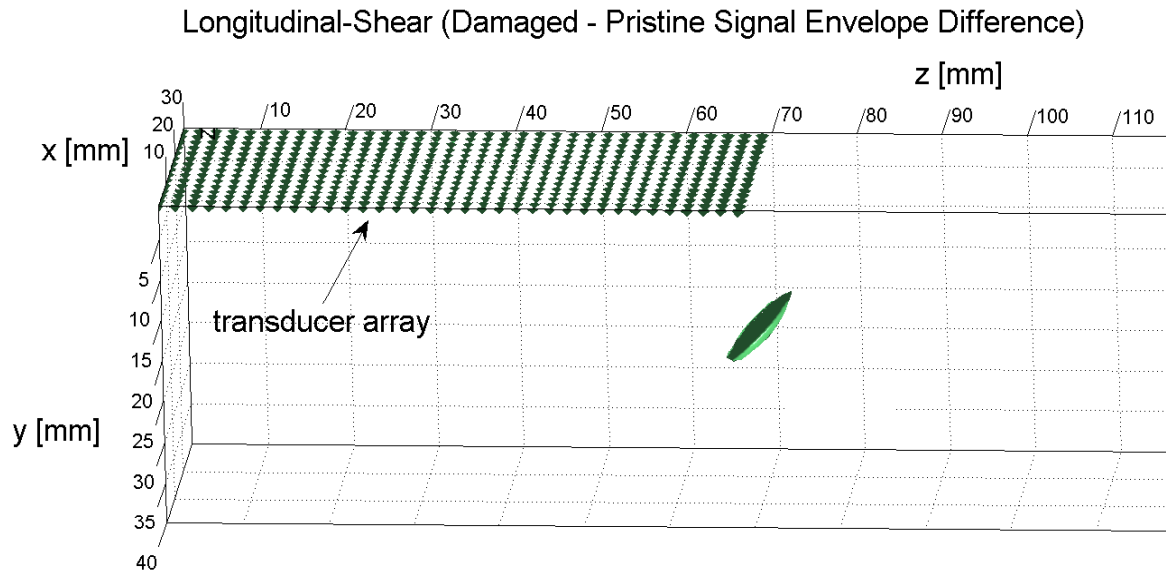
Figure 7.14. 3-D Imaging of 5% RHA Transverse Defect using the Longitudinal Wave mode and the Shear Wave mode with Envelope Baseline Subtraction (Full Array: 5 transmitters, 525 receivers).

Longitudinal-Shear (Damaged-Pristine Signal Envelope Difference)

Figure 7.15. 3-D Imaging of 5% RHA Transverse Defect using the Longitudinal Wave mode and the Shear Wave mode with Envelope Baseline Subtraction (Full Array: 5 transmitters, 525 receivers).

84

Longitudinal-Shear (Damaged - Pristine Signal Envelope Difference)

Figure 7.16. 3-D Imaging of 5% RHA Transverse Defect using the Longitudinal Wave mode and the Shear Wave mode with Envelope Baseline Subtraction (Full Array: 5 transmitters, 525 receivers).

Figures 7.17 through 7.20 show the imaging result obtained using the longitudinal mode only (L-wave velocity for transmitter-to-defect path and for defect-to-receiver path) using matched filtering and image baseline subtraction. Again, the defect indication is clearly shown with excellent contrast, with no extraneous artifacts, image noise, or uncorrelated speckle noise. The defect imaged with the L-mode alone appears in a position that is very accurate in both horizontal direction (direction z in the figures) and vertical direction (direction y in the figures). The circular contour of the defect image in this mode is more irregular, with contour lobes that are not present in the L-wave/S-wave imaging mode discussed previously. The origin of these contour lobes will be investigated in the following phase. More importantly, the *size* of the defect (to reemphasize the most important parameter for decisionmaking from an in-service rail inspection perspective) is imaged, again, very accurately. With an actual defect size of 141 mm^2 (or 5 percent rail RHA), the L-wave tomographic imaging yields a defect size of 154 mm^2 (or 5.4 percent rail RHA). In summary:

Full array (5 transmitters, 525 receivers)

- Actual defect size: 5 percent rail RHA

- Defect size calculated from L-wave tomographic imaging: 5.4% rail RHA

Longitudinal - Longitudinal (Damaged - Pristine Image Difference)

Figure 7.17. 3-D Imaging of 5% RHA Transverse Defect using the Longitudinal Wave mode along with Image Baseline Subtraction (Full Array: 5 transmitters, 525 receivers).

Longitudinal-Longitudinal (Damaged - Pristine Image Difference)
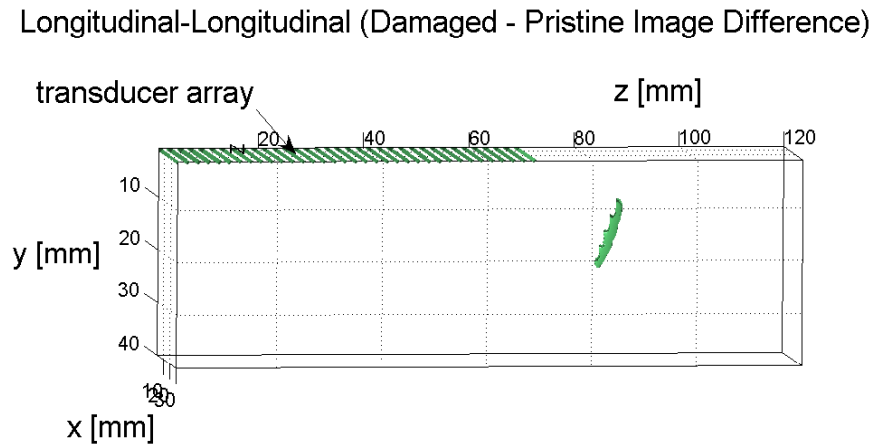
Figure 7.18. 3-D Imaging of 5% RHA Transverse Defect using the Longitudinal Wave mode along with Image Baseline Subtraction (Full Array: 5 transmitters, 525 receivers).

Longitudinal - Longitudinal (Damaged - Pristine Image Difference)
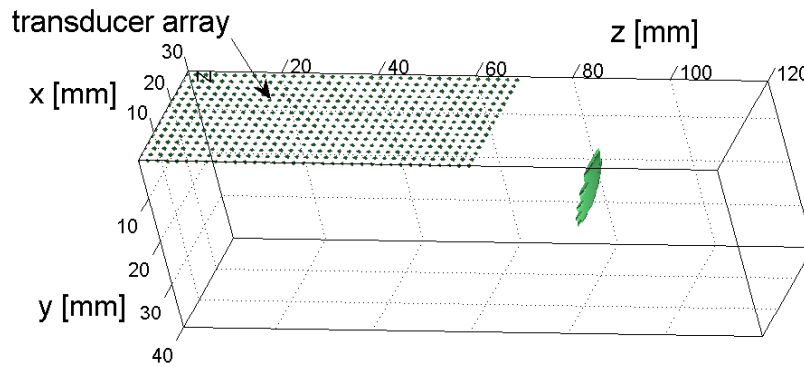
Figure 7.19. 3-D Imaging of 5% RHA Transverse Defect using the Longitudinal Wave mode along with Image Baseline Subtraction (Full Array: 5 transmitters, 525 receivers).

Longitudinal-Longitudinal (Damaged - Pristine Image Difference)
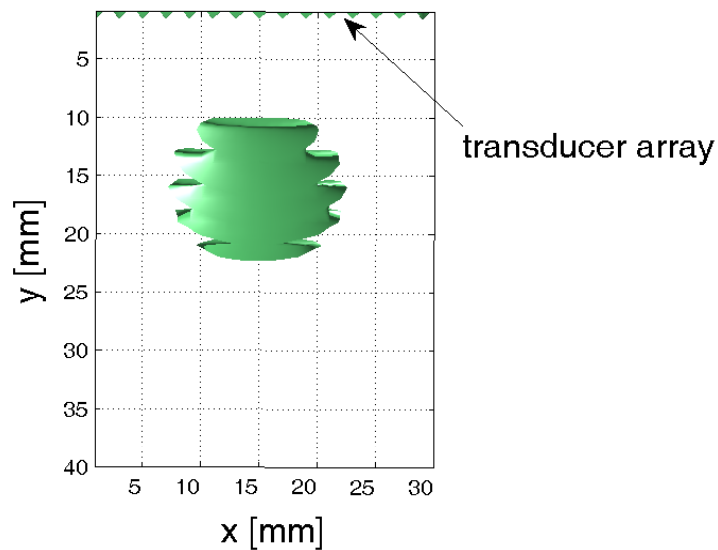
Figure 7.20. 3-D Imaging of 5% RHA Transverse Defect using the Longitudinal Wave mode along with Image Baseline Subtraction (Full Array: 5 transmitters, 525 receivers).

7.2.2 Results from the Reduced Array (5 transmitters, 140 receivers)

Representative results obtained by the reduced receiver array are shown in this section. Figures 7.21 through 7.23 show different views of the 3-D imaging by the longitudinal mode and the shear mode (Multimode Detection: L-wave velocity for transmitter-to-defect path and S-wave velocity for defect-to-receiver path) using matched filtering and envelope baseline subtraction. The results are very similar to those obtained with the full array. This finding is encouraging because it means that it is possible to substantially reduce the number of receivers (from 525 to 140), thereby reducing the electronic complexity and scan time of a future field prototype without substantially degrading the quality of the imaging results.

With an actual defect size of 141 mm^2 (or 5 percent rail RHA), the L-wave/S-wave tomographic imaging with reduced array yields a defect size of 148 mm^2 (or 5.25 percent rail RHA).

In summary:

Reduced array (5 transmitters, 140 receivers)

- Actual defect size: 5 percent rail RHA
- Defect size calculated from L-wave/S-wave tomographic imaging: 5.25 percent rail RHA
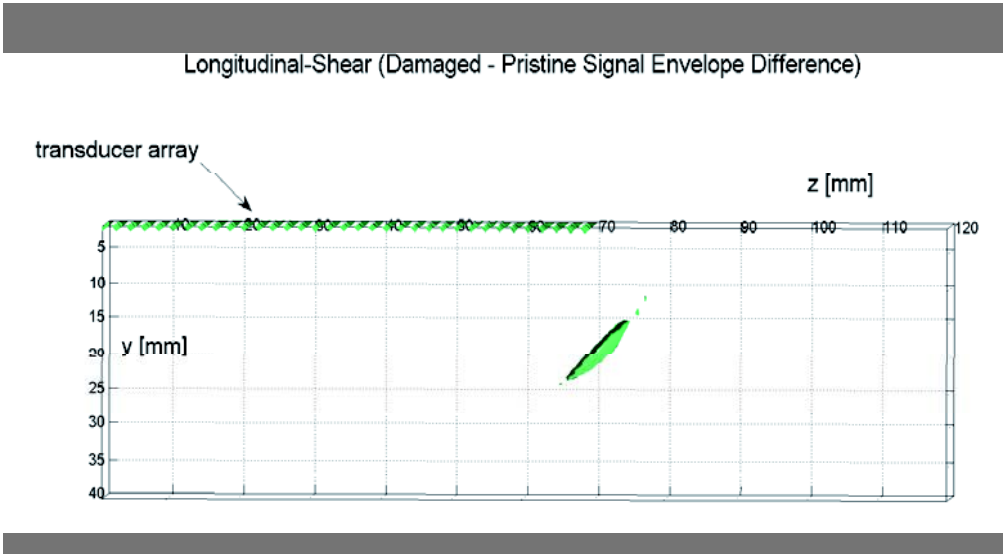
Figure 7.21. 3-D Imaging of 5% RHA Transverse Defect using the Longitudinal Wave mode and the Shear Wave mode with Envelope Baseline Subtraction (Reduced Array: 5 transmitters, 140 receivers).
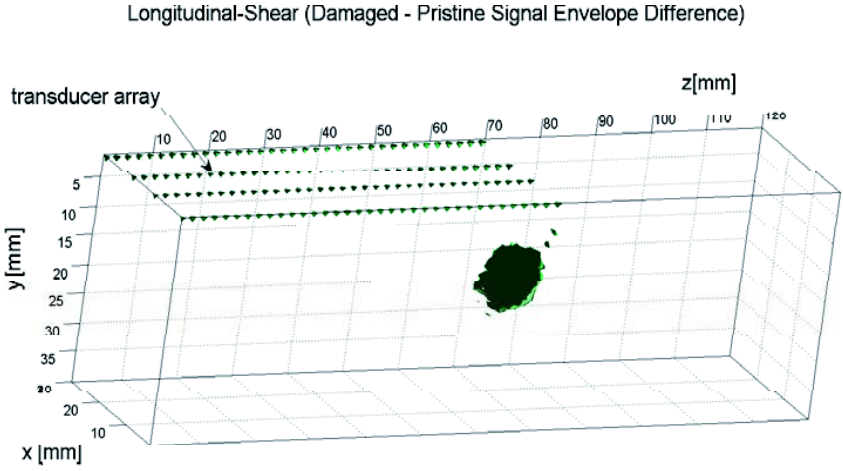
Figure 7.22. 3-D Imaging of 5% RHA Transverse Defect using the Longitudinal Wave mode and the Shear Wave mode with Envelope Baseline Subtraction (Reduced Array: 5 transmitters, 140 receivers).
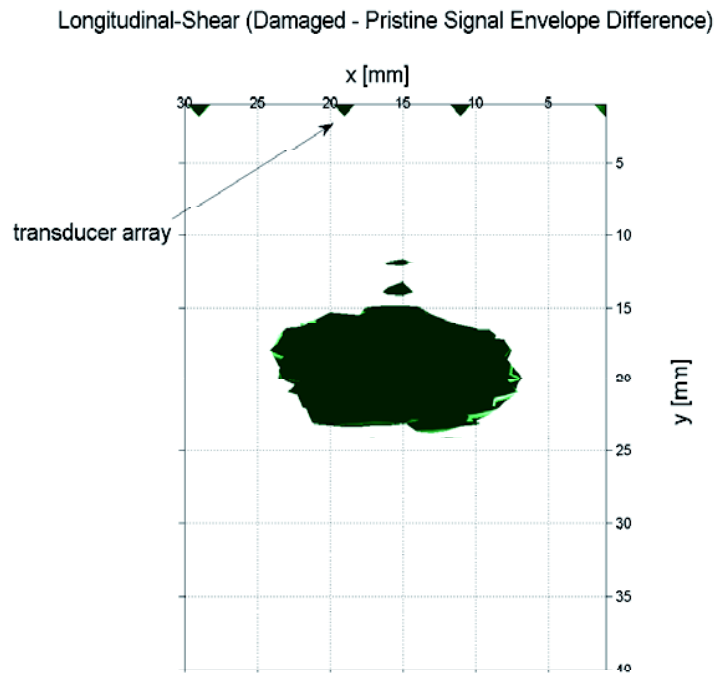
Figure 7.23. 3-D Imaging of 5% RHA Transverse Defect using the Longitudinal Wave mode and the Shear Wave mode with Envelope Baseline Subtraction (Reduced Array: 5 transmitters, 140 receivers).
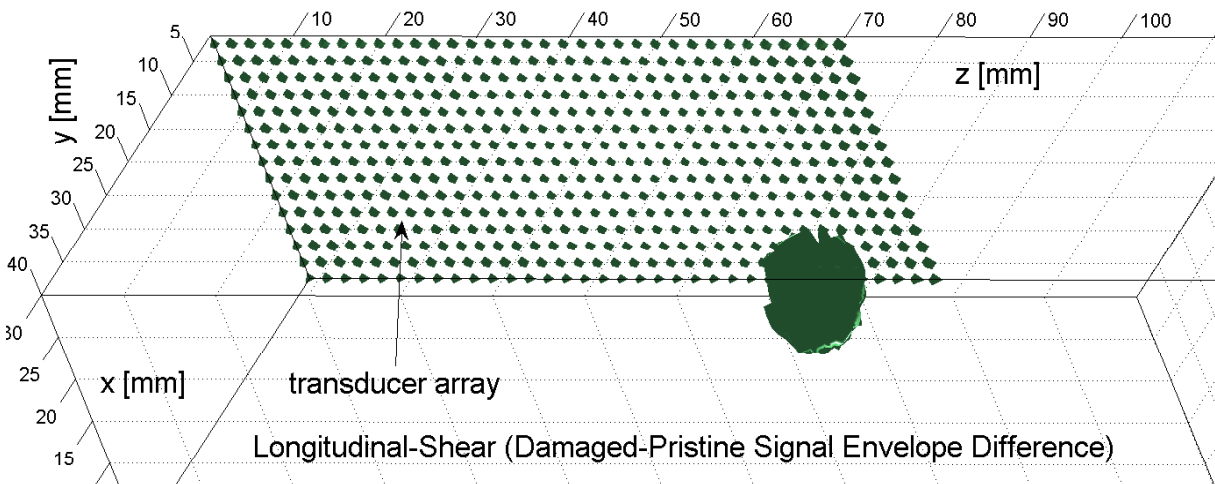
Figures 7.24 through 7.26 show the imaging result obtained by the reduced array using the longitudinal mode only (L-wave velocity for transmitter-to-defect path and for defect-to-receiver path), along with matched filtering and image baseline subtraction. Again, the results are very similar to those obtained with the full array, confirming the possibility of greatly reducing the computational complexity and scan time of a future field prototype.

With an actual defect size of 141 mm^2 (or 5 percent rail RHA), the L-wave tomographic imaging with the reduced array yields essentially the same defect size of 154 mm^2 (or 5.4 percent rail RHA) as the full array.

In summary:

Reduced array (5 transmitters, 140 receivers)

- Actual defect size: 5 percent rail RHA
- Defect size calculated from L-wave tomographic imaging: 5.4 percent rail RHA

Longitudinal-Longitudinal (Damaged - Pristine Image Difference)
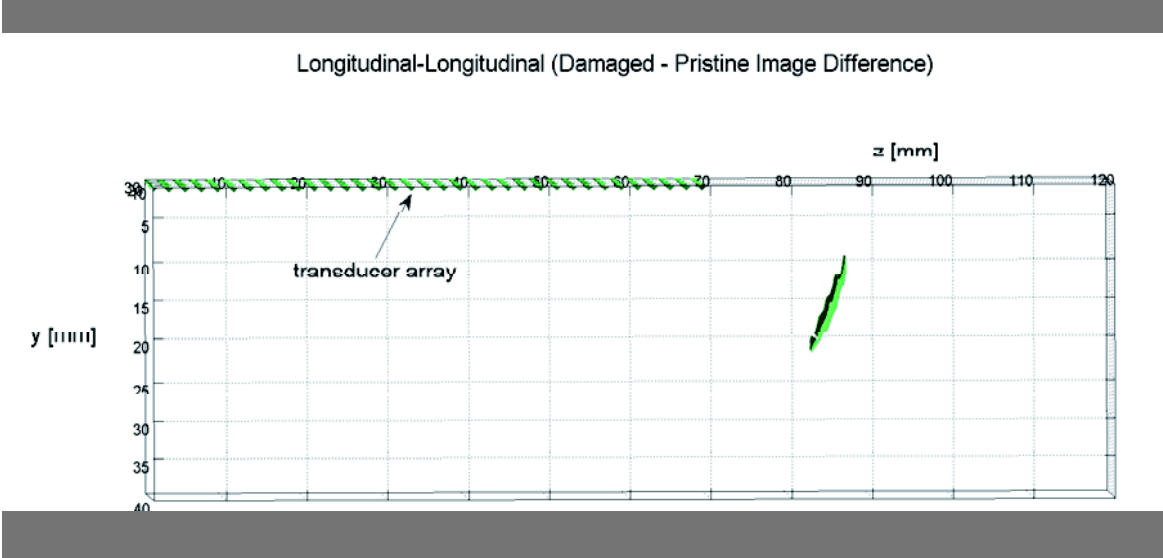
Figure 7.24. 3-D Imaging of 5 percent RHA Transverse Defect using the Longitudinal Wave mode along with Image Baseline Subtraction (Reduced Array: 5 transmitters, 140 receivers).
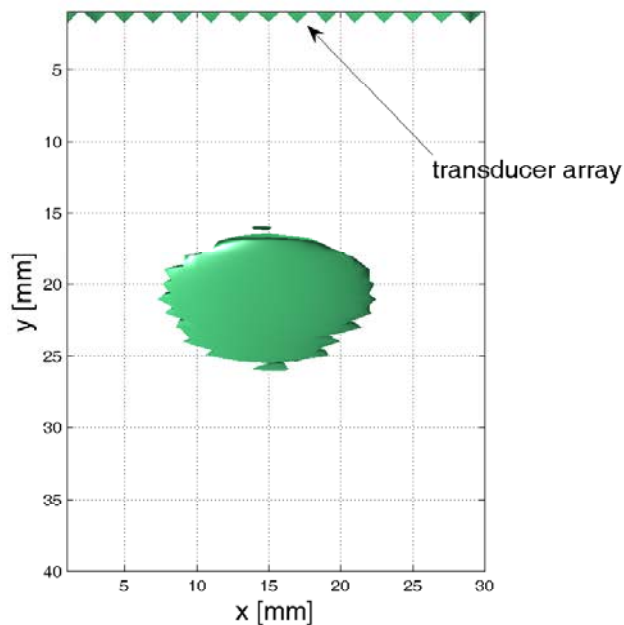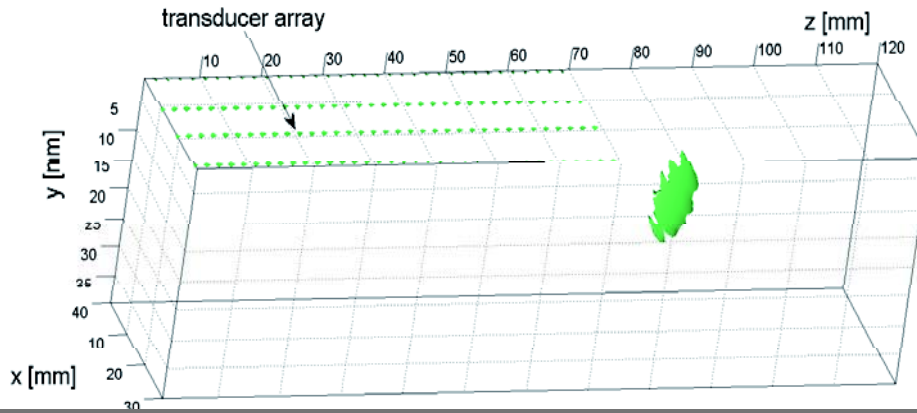
Figure 7.25. 3-D Imaging of 5% RHA Transverse Defect using the Longitudinal Wave mode along with Image Baseline Subtraction (Reduced Array: 5 transmitters, 140 receivers).
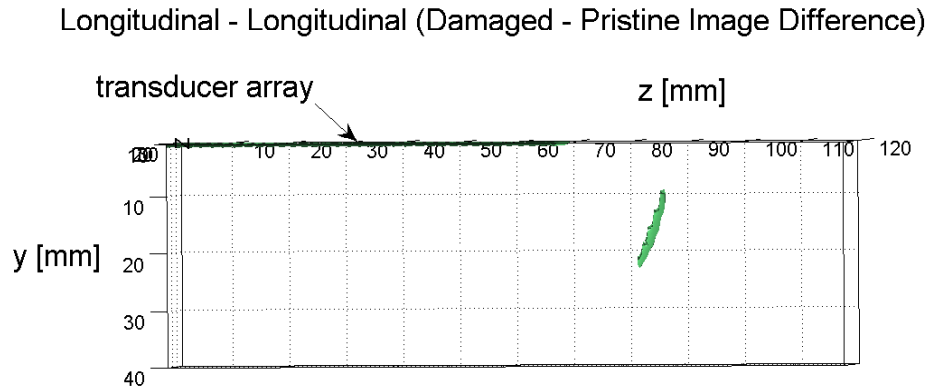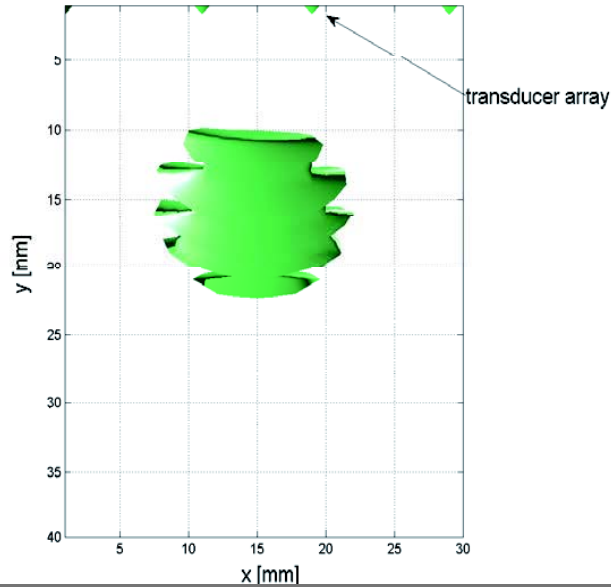

Figure 7.26. 3-D Imaging of 5% RHA Transverse Defect using the Longitudinal Wave mode along with Image Baseline Subtraction (Reduced Array: 5 transmitters, 140 receivers).

8. 3-D Rail Flaw Imaging: Case of Worn Rail

This chapter presents 3-D flaw imaging results from the proposed tomographic analysis applied to a worn rail profile (BNSF – worn rail geometry, tangent track).

8.1 Worn Rail Model

The effect of rail head wear on the performance of the tomographic imaging technique was examined. A profile of a worn tangent track was obtained from the BNSF Railway. The 3-D FE model was then constructed on the worn profile. Figure 8.1 shows the worn profile, along with the 3-D geometrical model developed for the FE analysis.
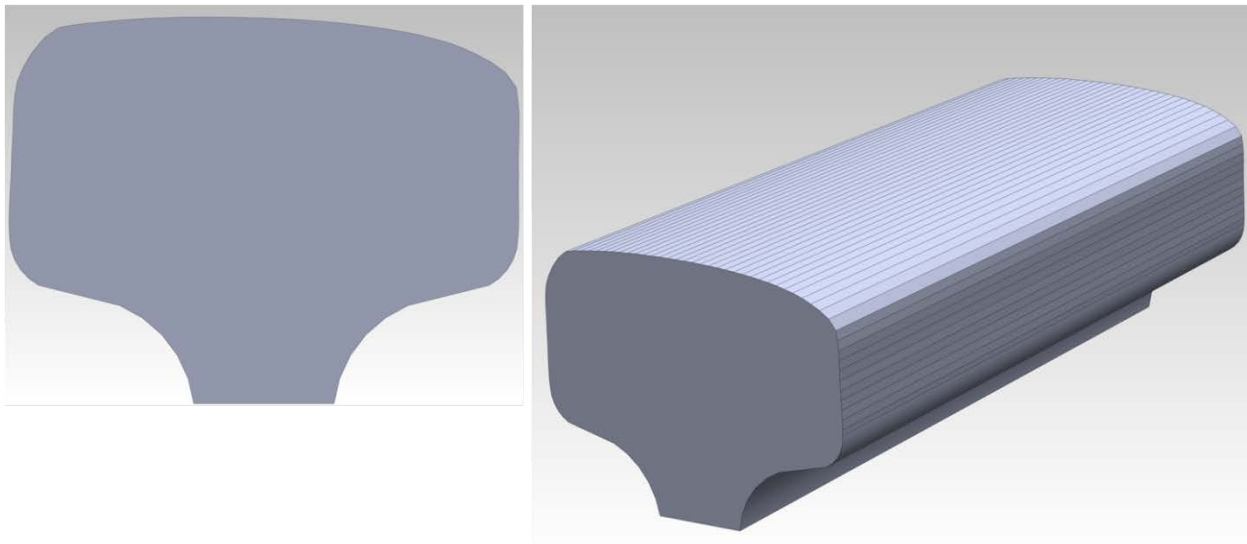
Figure 8.1. Worn BNSF rail profile (136-pound RE tangent track), and 3-D model constructed for the 3-D Finite Element Analysis and Tomographic Imaging.

The same 5-percent RHA TD considered for the new rail in the previous section was modeled for the worn rail case (Figure 8.2). Also, the same planar transducer array (up to 525 transducers) modeled for the new rail in section 7 was considered for the worn rail case (Figure 8.2). The array was considered "flat," hence the positions of each transducer considered in the SAF algorithm were on an ideal plane. As for the new rail study, "sparse" transmitters (5) were considered for the excitation.
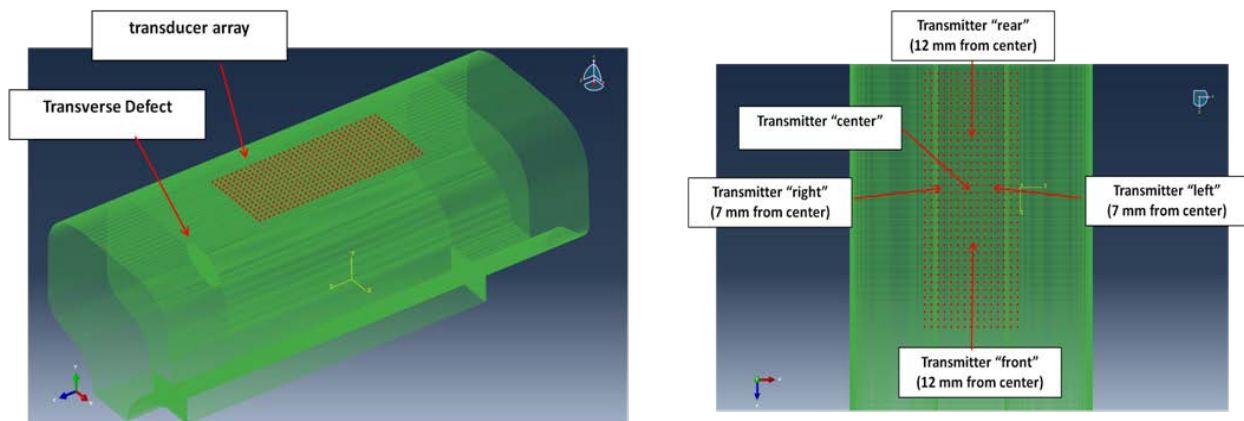
Figure 8.2. Transducer array modeled for the 3-D tomographic imaging of the worn rail.

8.2   Imaging Results from the 3-D Model of the Worn Rail

The imaging procedure followed the same steps taken for the imaging of the new rail discussed in section 7. Only the longitudinal shear mode combination was considered for the worn rail because it was proven more robust against noise by the 2-D imaging results (see section 8). In terms of transducer configurations, the following two configurations were modeled:

- "Sparse" transmitter array (5) with "full" receiver array (525), and
- "Sparse" transmitter array (5) with "reduced" receiver array (140).

The 3-D imaging results for the "full" receiver array on the worn rail are shown in Figure 8.3 (right) and compared with the equivalent results previously obtained for the new rail (left). It can be seen in the illustration that the degree of wear does not degrade the performance of the flaw images in any appreciable way.

94
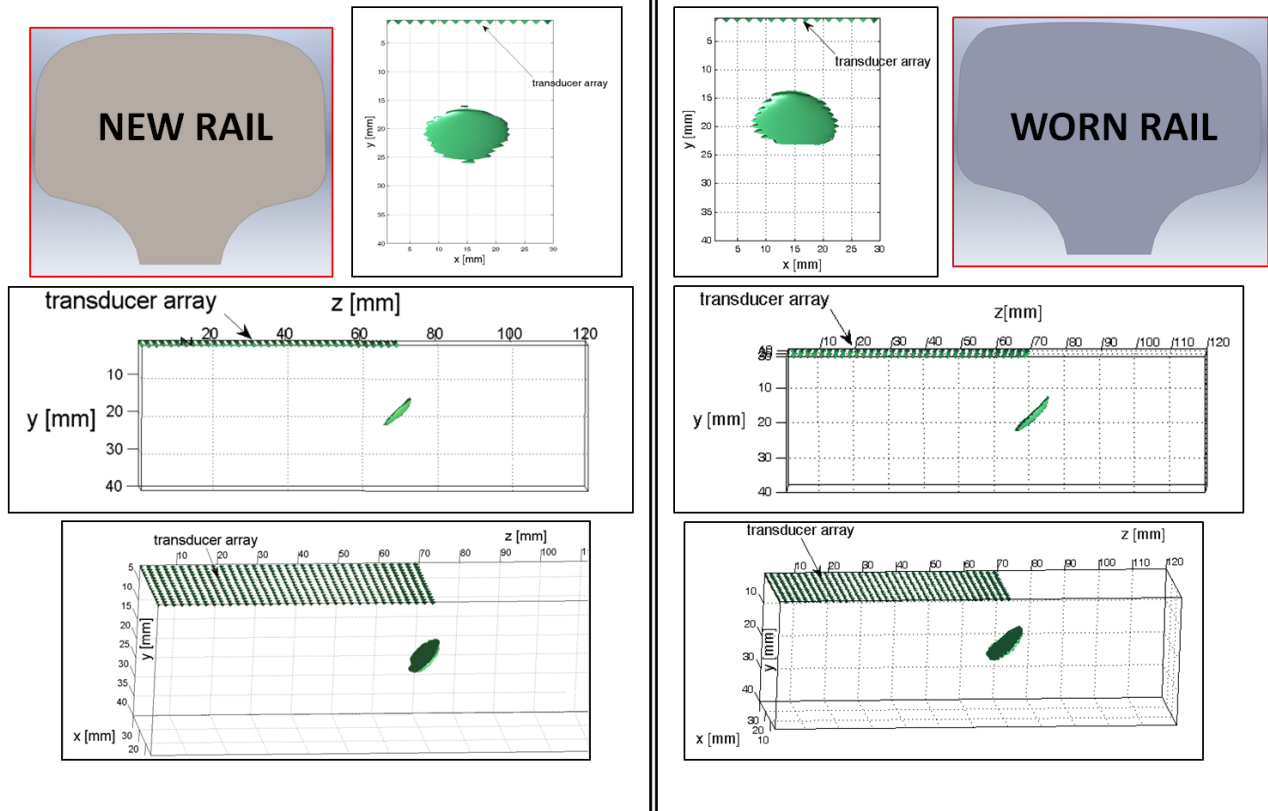
Figure 8.3. New rail versus worn rail: 3-D imaging of 5% RHA Transverse Defect using the Longitudinal Wave mode and the Shear Wave mode with Envelope Baseline Subtraction (Full Array: 5 transmitters, 525 receivers).

The 3-D imaging results for the "reduced" receiver array on the worn rail are shown in Figure 8.4 (right) and compared with the equivalent results obtained for the new rail (left). It can be seen in the illustration that the reduced number of receivers does affect the performance of the imaging method on the worn rail; however, the image degradation is not too severe. More importantly, the positions of the 140 reduced receivers were chosen quite randomly, and different positions would likely yield different results. Finally, in the case of severe rail wear, it is always possible to correct for any changes in the railhead profile by inputting the exact positions of the transducers in the SAF algorithm. Using the exact transducer positions will theoretically eliminate any effect of rail wear on the performance of the imaging technique.

95
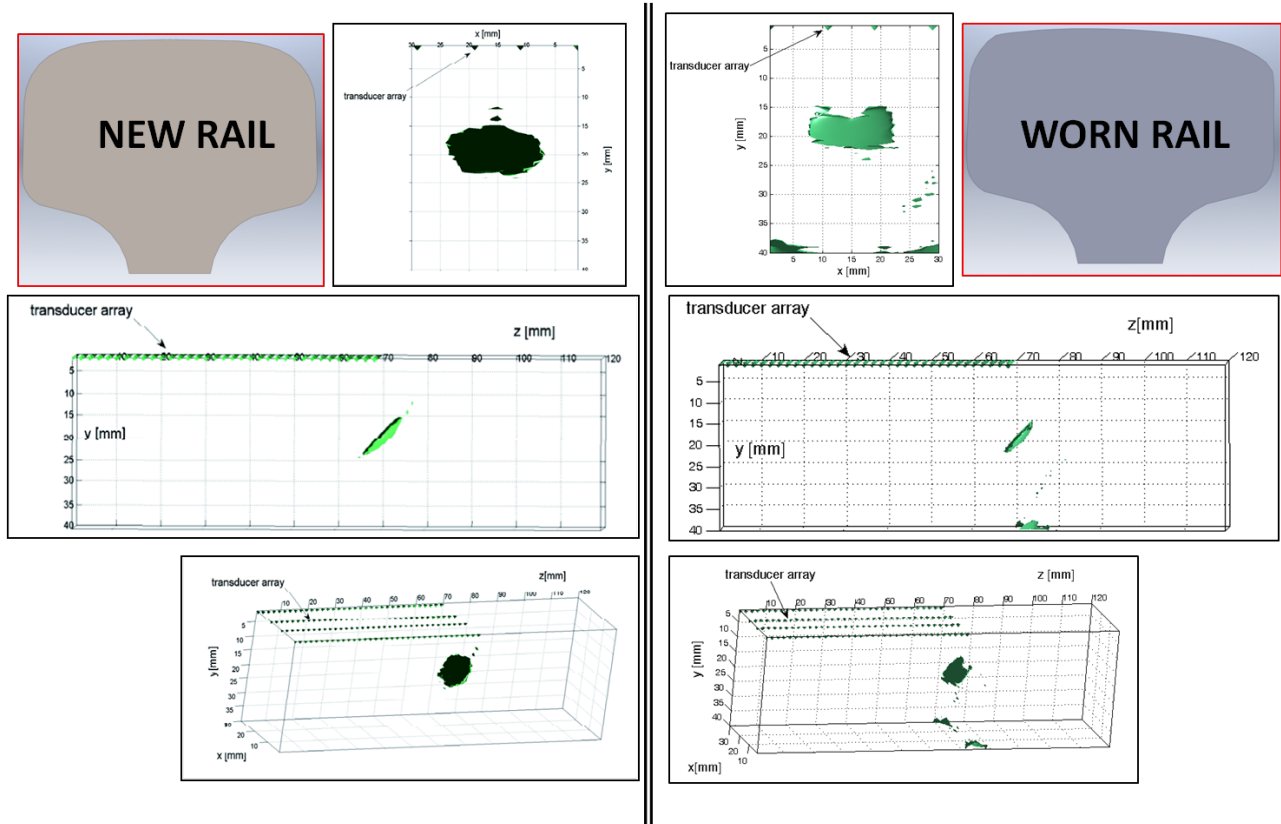
Figure 8.4. New rail versus worn rail: 3-D imaging of 5% RHA Transverse Defect using the Longitudinal Wave mode and the Shear Wave mode with Envelope Baseline Subtraction (Reduced Array: 5 transmitters, 140 receivers).

9. Conclusions

This report has shown the successful 3-D imaging using ultrasonic tomography of a 5-percent RHA TD in the rail head. The work has been purely numerical, involving FEA to simulate the behavior of the tomographic ultrasonic array on a flawed rail, followed by a tomographic algorithm for the 3-D imaging of the rail's interior.

The report begins with a review of ultrasonic testing in the railroad industry, followed by a review of tomographic imaging in several fields, including the medical field and the civil engineering field. The report then describes the FEA model developed to simulate the tomographic imaging procedure using transducer arrays.

Imaging of the 5-percent RHA TD in the railhead was conducted first in 2-D and then in 3-D. The 3-D FEA used the rather sophisticated features of "infinite elements" (to eliminate the artificial wave reflections at the model boundaries—which would be nonexistent in an actual experimental testing), as well as "numerical damping" to introduce a realistic level of wave damping as applicable to the imperfect surface of a rail.

The ultrasonic tomographic method developed in this project combines several algorithmic steps that are at the forefront of medical, sonar, and radar imaging, and adapts these steps to rail flaw imaging. In particular, the following steps were implemented: (1) SAF with Sparse Transmitters, (2) Matched Filtering, (3) Baseline Subtraction, and (4) Multimode Detection. A Matlab$^©$ program was written and tested to combine all of these steps so that the imaging result in 3-D is obtained in one single analysis. The Matlab$^©$ interface also allows the researchers to rotate the view of the inspected volume at will, a feature that would likely be useful in a possible future field-deployable system.

The imaging process envisages a planar array of ultrasonic transducers located at the top of the railhead and operating in a reflection scheme. Since the array is stationary, no transducer movement is required for full 3-D visualization of the railhead. The full array considered in this report uses 525 elements (overall size of 28 mm×68 mm) with only 5 elements acting as transmitters. For the reception, two cases were considered: a full array (all 525 elements receive) and a reduced array (only 140 elements receive).

The best tomographic 3-D imaging results of the 5-percent RHA TD were obtained using either a combination of the L-wave mode and the S-wave mode, or the L-wave mode alone. In both modalities, the defect size was estimated very accurately. Table 1 summarizes the flaw sizing results extracted from Figures 9.10 through 9.26. Another encouraging conclusion was that the full array (all 525 receivers) and the reduced array (only 140 receivers) yielded very similar images and flaw sizing estimates. This indicates the possibility of greatly reducing the electronic complexity and the scan time required by a future field-deployable prototype.

Table 9.1. Rail flaw sizing results from the 3-D Tomographic Imaging models.

	Full Array (5 transmitters, 525 receivers)		Reduced Array (5 transmitters, 140 receivers)	
	L-wave mode + S-wave mode	L-wave mode alone	L-wave mode + S-wave mode	L-wave mode alone
Imaged Transverse Flaw Size	**5.3% Head Area**	**5.4% Head Area**	**5.25% Head Area**	**5.4% Head Area**
Actual Transverse Flaw Size	**5% Head Area**			

Although defect sizing was very accurate, in some cases errors were found in the estimation of the precise defect location and defect contour shape. Specifically, the L-wave/S-wave modality presented slight inaccuracies in defect location while retaining excellent defect contour shape representation. The L-wave alone modality, on the other hand, presented artificial contour "lobes" while retaining excellent defect location.

The final analyses of this project were conducted on a model of a worn rail whose geometry was provided by BNSF (136-pound RE tangent track). The tomographic array was considered to be in the ideal "flat" position to test the effect of the worn profile on the image reconstruction. The results showed that when using the full array (5 transmitters, 525 receivers), rail wear had virtually no effect on the performance of tomographic imaging of the 5-percent RHA TD. When

the array was reduced to 140 receivers, some degradation of the flaw image was noted, although the degradation was not too severe. Clearly, the results depend on the exact level of wear considered. In addition, it is worth noting that for severely worn profiles it is always possible to input the actual positions of the array transducers in the tomographic imaging algorithm. Accounting for the actual transducer positions will theoretically eliminate the effect of any worn profile on the resulting SAF image.

It is also important to emphasize that the ultrasonic frequency of 2 MHz used in the 3-D imaging was limited by the FEA computational requirements. With any ultrasonic testing, higher frequencies generally yield increased defect resolution. Therefore, an actual tomographic imaging system for the field would likely use frequencies higher than what was simulated in these models.

The models developed within this project have shown excellent potential for using ultrasonic tomographic techniques to produce 3-D images of internal rail flaws. Based on these results, it seems possible to develop an ultrasonic tomographic system for rail flaw characterization in the field.

10.   References

Anderson, A. and Kak, A. (1982). "Digital ray tracing in two-dimensional refractive index field," *Journal of Acoustical Society of America*, 72, pp. 1593–1606.

Anon, F. (1990). "Rail-flaw detection. A science that works," *Railway Track and Structures*, 86, pp. 30–32.

ASNT. (2007). *Nondestructive Testing Handbook, Volume 7 Ultrasonic Testing*, 3rd edition. American Society for Nondestructive Testing.

Berndt H., Schniewind, A.P. and Johnson, G.C. (1999). "High resolution ultrasonic imaging of wood," *Wood Science and Technology*, 33, pp. 185–98.

Bian, H. and Rose, J.L. (2005). "Sparse array ultrasonic guided wave tomography," *Materials Evaluation*, 10, pp. 1035–1038.

Bishko, A., Samokrutov, A. and Shevaldykin, V. (2008). "Ultrasonic echo-pulse tomography of concrete using shear waves low-frequency phased antenna arrays," *Proceedings 17th World Conference on Nondestructive Testing*, October 25–28, 2008, Shanghai, China.

Bray, D.E. (1991). "Ultrasonic testing applications in the transportation industries-part 1." *ASNT Nondestructive Testing Handbook-Ultrasonic Testing, 2nd Ed*. Vol. 7. Columbus, OH: The American Society for Nondestructive Testing, pp. 609–634.

Bucur, V. (2003). "Techniques for high resolution imaging of wood structure: a review," *Measurement Science and Technology*, pp. R91–R98.

Chan, F.W. and Tsang, F.W. (2006). "Quality assurance of concrete foundation elements using an ultrasonic evaluation technique," *Insight - NDT and Condition Monitoring*, *Journal of the British Institute of NDT*, 48, pp. 360–367.

Chernauskas, L.R. and Paikowsky, S.G. (2000). "Defect detection and examination of large drilled shafts using a new cross-hole sonic logging system," *Performance Verification of Constructed Geotechnical Facilities*, Amherst: GeoInstitute/ASCE Specialty Conference, April 9–12, 2000.

Clark, R. and S. Singh. (2003). "The inspection of thermite welds in railroad rail – a perennial problem," *Insight - NDT and Condition Monitoring*, *Journal of the British Institute of NDT*, 45, pp. 387–393.

CTL Group. (2011). Ultrasonic Shear Wave Tomography or "MIRA," http://www.ctlgroup.com/OurExpertise/ConsultingServices/Detail/43

Daher, N.M. and Yen, J.T. (2006). "2-D Array for 3-D ultrasound imaging using synthetic aperture techniques," *IEEE Transactions on Ultrasonics, Ferroelectrics and Frequency Control*, 53, pp. 912–924.

Daigle, M., Fratta, D. and Wang, L.B. (2005). "Ultrasonic and X-ray tomographic imaging of highly contrasting inclusions in concrete specimens," *Proceedings of GeoFrontier Conference*, Austin, TX.

Denis, F., Basset, O. and Gimenez, G. (1995). "Ultrasonic transmission tomography in refracting media: reduction of refraction artifacts by curved-ray techniques," *IEEE Transactions on Medical Imaging*, 14, pp. 173–188.

Devaney, A. (1982). "A filtered back-propagation algorithm for diffraction tomography," *Ultrasonic Imaging*, 4, pp. 336–350.

Devaney, A. (1984). "Geophysical diffraction tomography," *IEEE Transactions on Geological Science*, Special Issue on Remote Sensing, GE-22, pp. 3–13.

Duric, N., Littrup, L., Poulo, P, Babkin, A., Pevzner, R., Holsapple, E., Rama, O. and Glide, C. (2007). "Detection of breast cancer with ultrasound tomography: first results with the Computed Ultrasound Risk Evaluation (CURE) prototype," *Medical Physics*, 34, pp. 773–785.

Federal Railroad Administration. (2011). *Safety Statistics Data*. Washington, DC: Federal Railroad Administration, Office of Safety Analysis (http://safetydata.fra.dot.gov/officeofsafety).

Fink, M., Montaldo, G. and Tanter, M. (2003). "Time-reversal acoustics in biomedical engineering," *Annual Review of Biomedical Engineering*, 5, pp. 465–497.

Fink, M. and Tanter, M. (2010). "Multiwave imaging and super resolution," *Physics Today*, pp. 28–33, February 2010.

Frazier, C. and O'Brian, W.D. (1998). "Synthetic aperture techniques with a virtual source element," *IEEE Transactions on Ultrasonics, Ferroelectrics and Frequency Control*, 45, pp. 196–207.

Garcia, G. and Zhang, J. (2006). "Application of ultrasonic phased arrays for rail flaw inspection," *Report DOT/FRA/ORD-06*, July 2006.

Grady, M., Spera, Z. and Truong, L. (2009). "Case study of cross-hole sonic logging: a non-destructive testing method for determining the integrity of drilled shafts," Technical Report, http://tyu.eng.uml.edu/14.511_2012/doc/Final_T3_GradySperaTruong.pdf

Grewal, D.S. (1996). "Improved ultrasonic testing of railroad rail for transverse discontinuities in the rail head using higher order Rayleigh (M_{21}) waves," *Materials Evaluation*, 54, pp. 983–986.

Hansen, W. and Hintze, H. (2002). "Ultrasonic testing of railway axles with phased array technique*," Proceedings of 8th European Conference on Nondestructive Testing*, Barcelona, June 2002.

Haramy, K. and Mekic-Stall, N. (2000a). "Cross-hole sonic logging and tomographic imaging surveys to evaluate the integrity of deep foundations - case studies." Federal Highway Administration (FHWA).

Haramy, K. and Mekic-Stall, N. (2000b). "Evaluation of drilled shafts at Piney Creek Bridge using Crosshole Sonic Logging data and 3-D tomographic imaging method," *Proceedings of Highway Geopgysics – NDE Conference*, St. Louis, MO, December 4–7, 2006.

Ho, K.S., Billson, D.R. and Hutchins, D.A. (2007). "Ultrasonic Lamb wave tomography using scanned EMATs and wavelet processing," *Nondestructive Testing and Evaluation*, 22, pp.19–34.

Jensen, J.A., Ivanov, S.N., Gammelmark, K.L., and Pedersen, M.H. (2006). "Synthetic aperture ultrasound imaging," *Ultrasonics*, 44, pp. e5–e15.

Johnson, S., Greenlaf, J., Tanaka, M., Rajagopalan, B. and Bahn, R. (1978). "Quantitative synthetic aperture reflection imaging with correction for refraction and attenuation. Application of seismic techniques in medicine," *Proceedings of San Diego Biomedical Symposium*, San Diego, CA, 1978.

Kak, A, and Slaney, M. (2001). *Principles of Computerized Tomographic Imaging*. Society for Industrial and Applied Mathematics (SIAM).

Karaman, M., Li, P-C., and O'Donnell, M. (1995). "Synthetic aperture imaging for small scale systems," *IEEE Transactions on Ultrasonics, Ferroelectrics and Frequency Control*, 42, pp. 429–442.

Lanza di Scalea, F. (2007). "Ultrasonic testing applications in the railroad industry," Chapter 15: *Special Applications of Ultrasonic Testing*, in *Non-destructive Testing Handbook*, 3rd edition, P.O. Moore, ed., American Society for Nondestructive Testing.

Leonard, K.R., Malyarenko, E.V. and Hinders, M.K. (2002). "Ultrasonic Lamb wave tomography,'' *Inverse Problems*, 18, pp. 1795–1808.

Leonard, K.R. and Hinders, M.K. (2003). "Guided wave helical ultrasonic tomography of pipes," *Journal of the Acoustical Society of America*, 114, pp. 767–774.

Leonard, K.R. and Hinders, M.K. (2005). "Multi-mode Lamb wave tomography with arrival time sorting," *Journal of the Acoustical Society of America*, 117, pp. 2028–2038.

Lewitt, R.M. (1983). "Reconstruction algorithms: transform methods," *Proceedings IEEE*, 71, pp. 390–408.

Likins, G., Piscsalko, G., Rausche, F. and Hussein, M. (2004a). "Monitoring quality assurance for deep foundations," *Proceedings of Conference on Current Practices and Future Trends in Deep Foundations (GSP 125)*, pp. 222–238.

Likins, G., Webster, S. and Saavedra, M. (2004b). "Evaluation of defects and tomography for CSL," http://www.pile.com/reference/stresswave2004/SW2004-046-Eval_of_Defects_and_Tomography_for_CSL.pdf

Lockwood, G.R., Talman, J.R., and Brunke, S.S. (1998). "Real-time 3-D ultrasound imaging using sparse synthetic aperture beamforming," *IEEE Transactions on Ultrasonics, Ferroelectrics and Frequency Control*, 45, pp. 980–988.

Maitre, H. (2008). *Processing of Synthetic Aperture Radar Images*. Wiley and Sons, United Kingdom.

Malyarenko, E.V. and Hinders, M. K. (2000). ''Fan beam and double crosshole Lamb wave tomography for mapping flaws in aging aircraft structures,'' *Journal of the Acoustical Society of America*, 108, pp. 1631–1639.

Malyarenko, E.V. and Hinders, M. K. (2001). ''Ultrasonic Lamb wave diffraction tomography,'' *Ultrasonics*, 39, pp. 269–281.

Martinez, O., Parrilla, M., Izquierdo, M.A.G. and Ullate, L.G. (1999). "Application of digital signal processing techniques to synthetic aperture focusing technique images," *Sensors and Actuators*, 76, pp. 448–156.

Martinis, R. (2002). "Nondestructive techniques for decay diagnosis on standing trees (Analisi di tecniche non destruttive per la diagnosi di carie su alberi in piedi)," *M.S. Thesis*, University of Florence, Italy.

McKeon, J.C.P. and Hinders, M.K. (1999a). ''Lamb wave contact scanning tomography,'' *Review of Progress in QNDE*, D.O. Thompson and D.E. Chimenti, eds., Plenum Press, New York, 18, p. 951–960.

McKeon, J.C.P. and Hinders, M.K. (1999b). ''Parallel projection and crosshole Lamb wave contact scanning tomography,'' *Journal of the Acoustical Society of America*, 106, pp. 2568–2577.

Mekic-Stall, S. and Grimm, P. (2002). "2D & 3D crosshole sonic logging tomography (CSLT) versus crosshole sonic logging (CSL) for drilled shafts," *Proceedings of 2nd Annual Conference on Applied Geophysics and NDT Technologies and Methods to Transport Facilities and Infrastructure*, FHWA-02-001(CD-ROM), Paper #32.

Nahamoo, D., Pan, S. and Kak, A. (1984). "Synthetic aperture diffraction tomography and its interpolation-free computer implementation," *IEEE Transactions Sonics and Ultrasonics*, SU-31, pp. 218–229.

Neuenschwander, J., Niemz, P. and Kucera, L.J. (1997). "Studies for visualizing wood defects using ultrasonic in reflection and transmission mode," *Holz Roh-Werkst*, 55, pp. 339–340.

Nikolov, S. and Jensen, J.A. (2000). "3-D Synthetic aperture imaging using a virtual source element in the elevation plane," *Proceedings 2000 IEEE Ultrasonics Symposium*, 1743–1747.

Nikolov, S. and Jensen, J.A. (2003). "Investigation of the feasibility of 3-D synthetic aperture imaging," *IEEE Ultrasonics Symposium*, 1903–1906.

Oralkan, O., Ergun, A., Johnson, J., Karaman, M. and Khuri-Yakub, B. (2002). "Capacitive micromachined ultrasonic transducers: next-generation arrays for acoustic imaging?" *IEEE Transactions on Ultrasonics, Ferroelectrics and Frequency Control*, 49, pp. 1596–1610.

Paikowsky, S.G., Chernauskas, L.R., Hart, L.J., Ealy, C.D. and DiMillio, A.F. (2000). "Evaluation of a new Cross-hole Sonic Logging system for integrity examination of drilled shafts," *Proceedings 6th International Conference Application of Stress-Wave Theory to Piles*, Niyama & Beim, eds., Rotterdam, pp.223–230.

Pan, S. and Kak, A. (1983). "A computational study of reconstruction algorithms for diffraction tomography: interpolation vs. filtered-backpropagation," *IEEE Transactions on Acoustical Speech Signal Processing*, ASSP-31, pp. 1261–1275.

Prada, J., Fratta, D. and Santamarina, J. C. (2000). "Tomographic detection of low-velocity anomalies with limited data sets," *ASTM Geotechnical Testing Journal*, 23, pp. 472–486.

Rathore, S., Kishore, N., Munshi, P. and Singhal, S. (2000). "Ultrasonic tomography of closely spaced defects," *Proceedings of the 15th World Congress in Nondestructive Testing*, Rome.

Rizzo, P. (2010). "Water and wastewater pipe health monitoring: a review," *Advances in Civil Engineering*, Article ID 818597, doi:10.1155/2010/818597.

Sandrin, L., Tanter, M., Catheline, S. and Fink, M. (2002). "Shear modulus imaging with 2-D transient elastography," *IEEE Transactions on Ultrasonics, Ferroelectrics and Frequency Control*, 49, pp. 426–435.

Shoup, T.A. and Hart, J. (1988), "Ultrasonic imaging systems," *Proceedings 1988 IEEE Ultrasonics Symposium*, 863–871.

Simonetti, F. and Huang, L. (2008). "From beamforming to diffraction tomography," *Journal of Applied Physics*, 103, pp. 1101–1107.

Sperry Rail Service. (1989). *Rail Defect Manual*. Danbury, Connecticut.

Tscharntke, D., Heckel, T., Boehm, R., Erhard, A., Krull, R., Lutzner, J. and Hintze, H. (2003). "Development of ultrasonic railway inspection systems using phased array methods," *Railway Engineering International Conference*, London, April 30–May 1, 2003.

Utrata, D. (2002), "Exploring enhanced rail flaw detection using ultrasonic phased arrays inspection," *Review of Progress in Quantitative Nondestructive Evaluation*, Vol. 21, Thompson and Chimenti, eds.

Wells, P. (1977). *Biomedical Ultrasonics*. London, Academic Press.

Wilcox, P., Evans, M., Pavlakovic, B., Alleyne, D., Vine, K., Cawley, P. and Lowe, M. (2003). "Guided wave testing of rail," *Insight - NDT and Condition Monitoring*, *Journal of the British Institute of NDT*, 45, pp. 413–420.

Wooh, S-C. and Wang, J. (2002). "Nondestructive characterization of defect using a novel hybrid ultrasonic array sensor," *NDT&E International*, 35, pp. 155–163.

Abbreviations and Acronyms

BNSF	Burlington Northern Santa Fe Railway
FE	Finite Element
FEA	Finite Element Analysis
RHA	Rail Head Area
TD	Transverse Defect
L-wave	Longitudinal Wave
RCF	Rolling Contact Fatigue
RHA	Rail Head Area
SAF	Synthetic Aperture Focus
SAFT	Synthetic Aperture Focus Technique
S-wave	Shear Wave